SAKARYA ÜNİVERSİTESİ
FEN BİLİMLERİ ENSTİTÜSÜ DERGİSİ

Sakarya University Journal of Science
SAUJS

ISSN 1301-4048 e-ISSN 2147-835X Period Bimonthly Founded 1997 Publisher Sakarya University
http://www.saujs.sakarya.edu.tr/

Title: Facile Synthesis And Characterization Of gCN, gCN-Zn And gCN-Fe Binary Nanocomposite And Its Application As Photocatalyst For Methylene Blue Degradation

Authors: Mustafa KAVGACI, Hasan ESKALEN

Recieved: 2022-10-28 00:00:00

Accepted: 2023-02-23 00:00:00

Article Type: Research Article

Volume: 27
Issue: 3
Month: June
Year: 2023
Pages: 530-541

How to cite
Mustafa KAVGACI, Hasan ESKALEN; (2023), Facile Synthesis And Characterization Of gCN, gCN-Zn And gCN-Fe Binary Nanocomposite And Its Application As Photocatalyst For Methylene Blue Degradation. Sakarya University Journal of Science, 27(3), 530-541, DOI: 10.16984/saufenbilder.1195934
Access link
https://dergipark.org.tr/en/pub/saufenbilder/issue/78131/1195934

Sakarya University Journal of Science 27(3), 530-541, 2023

Facile Synthesis and Characterization of gCN, gCN-Zn and gCN-Fe Binary Nanocomposite and Its Application as Photocatalyst for Methylene Blue Degradation

Mustafa KAVGACI [*1,3], Hasan ESKALEN [2,3]

Abstract

The combustion method to obtain for pure graphitic carbon nitride (gCN) and two binary nanocomposites, gCN-Zn - gCN-Fe have been used in the present study. The structural, morphological, thermal and optical characterizations of the syhtesized samples were characterized with X-ray diffraction, scanning electron microscopy, thermogravimetric analysis (TGA) and UV-Vis spectroscopy. The intensity of characteristic gCN peak at (002) crystalline plane decrease with formation of binary nanocomposites was observed. The EDX spectra supports presents of Zn and Fe element in binary nanocomposites. The bandgap of pristine gCN is calculated as 2.75 eV and it decreases to 2.58 eV and 2.50 eV for Zn and Fe addition. The degradation capacity of pristine gCN and synthesized binary nanocomposites showed an enhanced photodegradation performance for binary composite relative to pristine gCN was observed. The maximum degradation performance was observed at gCN-Zn binary composite. The obtained composites with this simple synthesis method and cost effective raw materials used for the photodegradation of methylene blue dye detail.

Keywords: Degradation, Zn, Fe, methylene blue (MB), graphitic carbon nitride (gCN)

1. INTRODUCTION

Environmental pollution is one of the significant problems for humans and other living organisms. Unfortunately, pollution increases in parallel to industrialization, which might result in pollution of water sources and unhealthy drinking water. To overcome this problem, some scientists focused on water treatment, especially pollution originating from dyestuff. Since the wastewater from dye can contaminate not only freshwater sources but also sands, that may magnify the risk [1–5]. Some of the organics dyes are toxic, carcinogenic, and have mutagenic potential [6]. Considering the current situation of dyes, especially their types (more than 100,000 varied structured) and different application areas (textile, medicine, pharmaceutic, cosmetics, food,

* Corresponding author:mkavgaci@gmail.com (M. KAVGACI)
[1] Elbistan Vocational School of Health Services, Department of Opticianry, Kahramanmaraş Istiklal University, Kahramanmaraş, Turkey.
[2] Vocational School of Health Services, Department of Opticianry, Kahramanmaraş Sutcu Imam University, Kahramanmaras, Turkey.
[3] Department of Material Science and Engineering, Graduate School of Natural and Applied Sciences, Kahramanmaraş Sutcu Imam University, Kahramanmaras, Turkey.
E-Mail: heskalen@gmail.com
ORCID: https://orcid.org/0000-0001-8747-0635, https://orcid.org/0000-0002-4523-6573

printing), the importance of treatment of wastewater originating from dyes may become more evident [7–9]. Different methods have been utilized to degrade wastewater, including physiochemical and biological approaches; photodegradation has massive potential for dealing with wastewater since its a clean and cost-effective method [10–12].

Graphitic carbon nitride (gCN) is defined as nitrogen substituted graphane with anisotropic 2D geometry, and aromatic conjugate structure [13]. gCN has been considered as a promotion material due to its original preparation methods, high stability, band gap and low cost [14–16]. Moreover, the earth abundant nature, suitable electronic band position, nontoxic characteristic, outstanding physicochemical stability and admirable optical properties has considered as novel specifications of the gCN [17, 18]. Triurea, melamine, cyanamide, urea, ammonium thiocyanate and dicyandiamide are some examples of gCN precursors that are inexpensive and high nitrogen content generally used in synthesis of gCN [17]. Fast charge carrier recombination, small particle size and poor absorption coefficient of the gCN negatively affect the photoactivity of pure gCN [19–21]. Different methods have been utilized to overcome this shortcoming like fabricating nano/mesoporous structures, coupling with other semiconductors, noble metal deposition and impurity doping [22–24]. Among them doping different elements like metal, metal oxide and nonmetals to the bulk structure results in a decrease in band gap and lead to enhancement of absorption of visible light [25]. Flower like copper/zinc bedecked gCN composite (gCN-CuO/ZnO) was fabricated and methylene blue dye (MB) degradation was investigated. The enhancement of the photocatalytic activity of gCN-CuO/ZnO relative to pure gCN has been observed [26]. H_2 release of P doped gCN - TiO_2 catalyst was used for hydrogen (H_2) release from the sodium borohydride ($NaBH_4$) methanolysis [27]. The photocatalytic degradation of Rhodamine B dye of gCN/nano zero valent iron doped bismuth ferrite nanoparticle composite demonstrated the degradation performance better than previously reported $BiFeO_3$ composite [28]. The photocatalytic performance of silver iodide- gCN nanocomposite was exhibited better behavior than pristine silver iodide and gCN over rhodamine B and methyl orange dye was reported [29]. Enhanced photocatalytic behavior observed with the addition of reduced graphene oxide and gCN to zinc oxide over methylene blue dye was investigated [30].

The present work has employed the combustion method to obtain two binary nanocomposites, gCN-Zn and gCN-Fe. The structural, morphological, thermal and optical characterizations were performed in detailly. The degradation capacity of pristine gCN and synthesized binary nanocomposites showed an enhanced photodegradation performance for binary composite relative to pristine gCN was observed. The obtained composites with this simple synthesis method and cost effective raw materials used for the photodegradation of methylene blue dye detail.

2. MATERIALS AND METHOD

2. 1. Materials

Ultra pure water was used in the studies. Ultra pure water was obtained from Kahramanmaras Sutcu Imam University University-Industry-Public Cooperation Development Application and Research Center (USKIM). All chemicals were used in tests and syntheses without purification. Thiourea (98%) was purchased from Merck, zinc nitrate (98%) was from Acros Organics, and iron nitrate (99%) was from Sigma Aldrich.

2. 2. Synthesis of gCN, gCN-Fe and gCN-Zn

gCN was produced using a the combustion method. Thiourea (10 g) in a ceramic crucible was heated to 550 °C at a heating rate of 10 °C/min in an muffle furnace. It was then calcined at 550 °C for 5 hours. gCN-Fe and gCN-Zn were synthesized under the same conditions. Briefly, 10 g of thiorue was dissolved in 50 mL of ultra water. Iron nitrate and zinc nitrate were then added to this solution in a weight ratio of 0.25:10. It was mixed on a magnetic stirrer for 1 hour. It was then dried at 90 °C for 48 hours. The obtained powder sample was heated to 550 °C at a heating rate of 5 °C/min and calcined at the same temperature for 5 hours. The synthesized samples were ground in a mortar for experiments. The graphitic carbon nitride gCN synthesized in a weight ratio of 0.25:10 was named as iron-doped graphitic carbon nitride gCN-Fe and zinc-doped graphitic carbon nitride gCN-Zn. Figure 1 shows a graphical representation of the gCN samples synthesis.

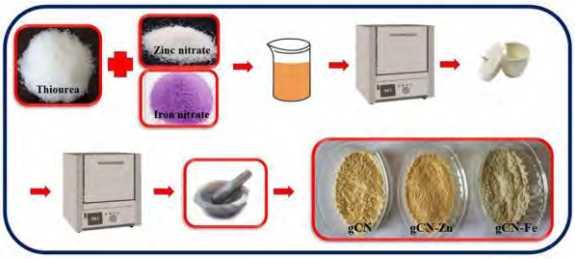

Figure 1 Scheme showing synthesis of gCN, gCN-Fe and gCN-Zn samples

2.3.Characterization

The X-ray diffraction (XRD) pattern of the gCN samples was obtained using a Philips brand X'Pert PRO model XRD instrument with Cu Ka radiation (λ=0.154056 nm, 40 kV and 30 mA). Scanning Electron Microscope (SEM) images and EDX measurements were taken with the FEI brand Quanta 650 Field Emission SEM model electron microscope available at Çukurova University Central Research Laboratory (CUMERLAB). Thermogravimetric analysis (TGA) was performed using a thermal analyzer (Perkin-Elmer Diamond) in a nitrogen atmosphere with a heating rate of 20 °C/min in the temperature range of 20 to 750 °C. FT-IR spectrum measurements were taken with the Perkin Elmer Spectrum 400 device in the range of 4000–400 cm^{-1}. UV–Vis absorption measurements were obtained with a Shimadzu-1800 UV spectrometer. XRD, TGA, FTIR and UV measurements were obtained in the USKIM laboratory.

2.4. Photocatalytic test

The photocatalytic performance of the produced gCN, gCN-Fe and gCN-Zn structures was tested with methylene blue (MB) dye. 20 mg of the photocatalyst gCN, 5 ppm was dropped into 50 mL MB solution (with water). First of all, the solutions to which the catalyst was added were kept in the dark for 30 minutes, taking into account the absorption-desorption balance. It was then tested by irradiation under a Xeon lamp light source (300 W Luzchem). Photocatalytic performances of the samples were investigated with a Shimadzu UV1800 spectrometer in 10-minute time [.

3. RESULTS AND DISCUSSION

Graphically showing the XRD patterns of gCN, gCN-Fe and gCN-Zn are presented (Figure 2). Two characteristic peaks of pure gCN appear prominently at 12.8° and 27.3° both (100) and (002) peaks can be attributed to interplanetary structural stacking of conjugated aromatic systems indexed for graphite materials. These peaks are consistent with the XRD data of the reported studies available in the literature for the gCN structure [31, 32]. It is clearly seen in the XRD graph that the intensity of the (002) peak decreases with the doping of Zn and Fe. This suggests that adding Zn and Fe can limit the crystal growth of gCN. The decrease in peak intensity can be attributed to an interaction between Zn/Fe and gCN. This effect deforms the nitride pore structure and changes the distance between the holes [33]. In addition,

the decrease in crystallinity in the (002) crystal planes can be attributed to the effects of Fe and Zn additions on the thermal condensation of urea/thiourea [34]. When the XRD graph was examined, no diffraction peak was observed for Zn and Fe structures.

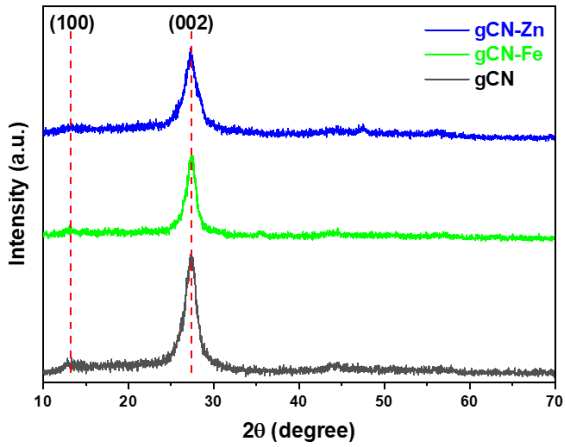

Figure 2 XRD pattern of gCN, gCN-Fe and gCN-Zn

SEM images illuminating the SEM surface morphologies of gCN, gCN-Fe and gCN-Zn are given in Figure 3. Characteristic plate-like structures are seen and the construction of pronounced 2D layered bulk sheets that remain grouped together is celarly seen from this figure. Fe and Zn additives did not affect gCN morphology [35]. This demonstrates that introducing Fe to gCN does not modify its sheet structure. According to result of similar research related to 5% Fe doped gCN that obtained composite not contain any iron nanoparticles, proving that Fe was ionically added to the gCN framework [36]. The addition of Fe to the carbon nitride structure does not alter the stacking of chain layers, implying that Fe-gCN preserves the original crystal structure of gCN [37]. The morphology of ZnO incorporated gCN was observed by SEM and the images reveal its 2-D layered nanosheet structures without much variation in its morphology upon incorporating zinc metal into gCN.

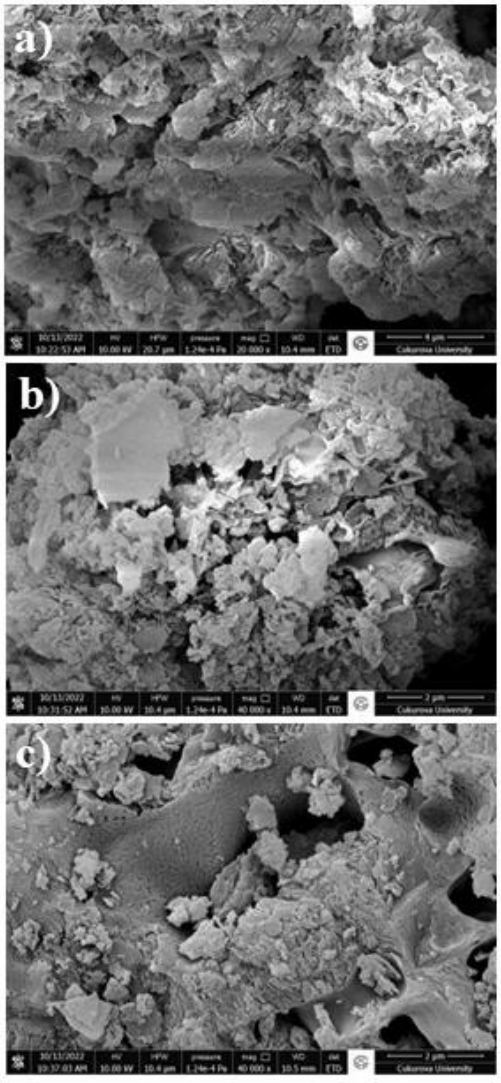

Figure 3 SEM images of gCN (a) gCn-Fe (b) and gCN-Zn (c)

EDX analysis was performed to determine the chemical composition of gCN, gCN-Fe and gCN-Zn nanocatalysts (Figure 4). The EDX spectra of the samples confirm the presence of C, N, O, Fe and Zn elements.

Optical band gap energies of the synthesized samples were determined by using optical absorption spectra. Optical band gaps were obtained with the Tauc plot. $(\alpha h\nu)^2$ for samples as a function of photon energy is plotted graphically in Figure 5. The band gap energy for gCN was found to be 2.75 eV. In the literature, some researchers found the same result for gCN [38, 39]. The addition of Zn and Fe decreased the band gap energy. Band gap energies for gCN-Zn and gCN-Fe

were found to be 2.58 eV and 2.50 eV, respectively. The results found are in agreement with previous studies. In the literature, some studies found that the forbidden energy gap decreases with the addition of Zn and Fe to gCN [33, 40, 41].

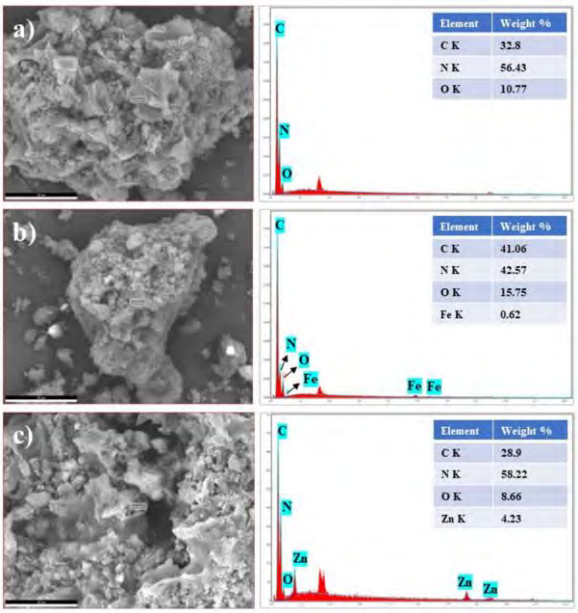

Figure 4 EDX spectra of gCN (a) gCn-Fe (b) and gCN-Zn (c)

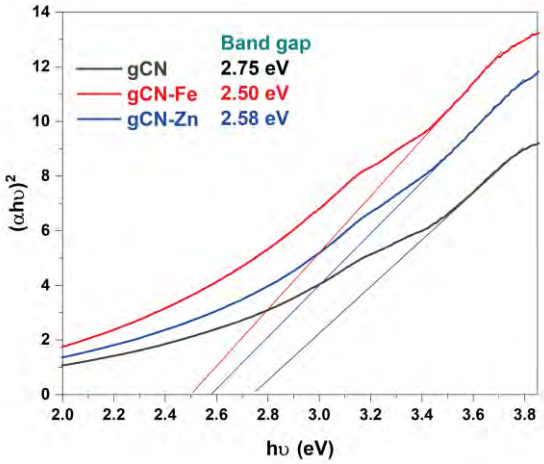

Figure 5 Bandgap graph gCN, gCN-Fe and gCN-Zn

The TGA pattern of gCN, gCN-Fe and gCN-Zn are presented in Figure 6. It is observed that the remarkable thermal decomposition of the samples starts around 400 °C. It is clearly seen that the samples show a tendency to decompose at temperatures higher than 600 °C. This result indicates that thermally gCN structures are one of the highly stable organic materials [42]. The degree of condensation seriously affects thermal stability. Complete degradation of the synthesized gCN sample takes place at 620 °C and no material remains. However, complete degradation does not occur in Zn and Fe doped gCN samples.

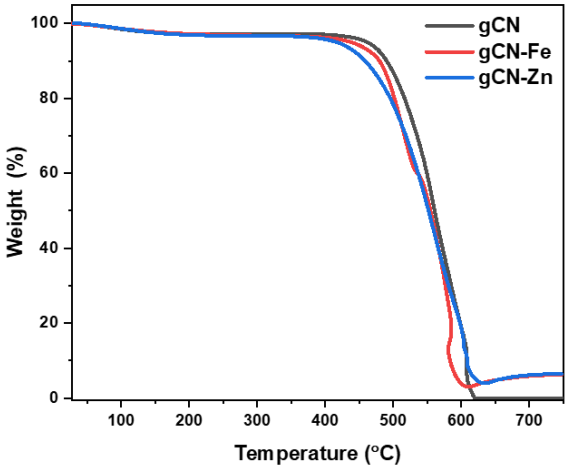

Figure 6 TG thermograms for the gCN, gCN-Fe and gCN-Zn

FTIR spectroscopy is used to detect tensile and bending vibrational bands of synthesized gCN structures and to examine the functional groups and types of chemical bonds of gCN structures. Figure 7 shows the FT-IR spectra of the synthesized gCN constructs. Measurements in the range of 450–4000 cm^{-1} were taken for the FTIR analysis. The broad absorption peak centered at 3150 cm^{-1} is attributed to the tensile vibration of the N–H group. The peaks seen in the 1000-1750 cm^{-1} range indicate the characteristic stretching modes of C-N heterocycles. The sharp peak observed at 805 cm^{-1} can be assigned to the respiratory mode typical of triazine units [43, 44]. As a result of the addition of Zn and Fe, the intensity of the peaks observed between 3150 cm^{-1} and 1000-1750 cm^{-1} decreased. This indicates that the crystallization of Fe and Zn can affect the thermal polymerization of Thiourea. It is consistent with the result of the XRD analysis, which shows that the addition of Fe and Zn can lead to the deterioration of the graphite structure of gCN [33].

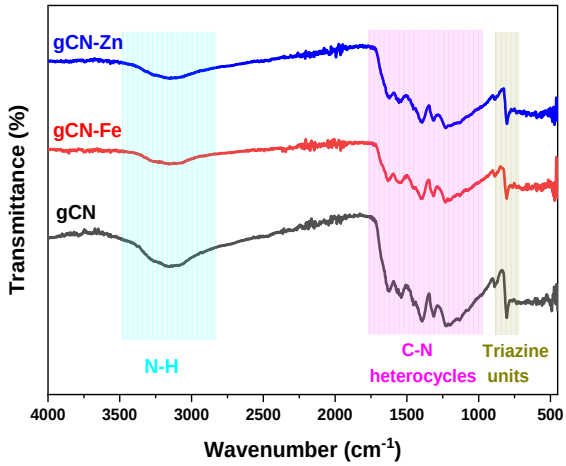

Figure 7 FTIR pattern of obtained samples

Optical absorptions of synthesized gCN samples were measured between 450-750 nm wavelengths using UV-vis spectroscopy. All samples were kept in the dark for 30 minutes and then measurements were taken with a UV-Vis spectrophotometer every 10 minutes for 60 minutes. The photocatalytic degradation of the catalyst-free and gCN-catalyzed dyestuff solutions with respect to time was investigated under normal conditions under 300 W Xenon light. In Figure 8, absorption graphs of gCN, gCN-Fe and gCN-Zn samples are given. The maximum peak in the UV-Vis absorption spectra of the dyestuffs was determined as 664 nm for methylene blue. 50 ml of 5 ppm methylene blue solution was taken and kept under xenon and room light for 60 minutes without a catalyst. The degradation rates under room conditions (called day in Figure 9) and under a xenon lamp (called sim in Figure 9) were determined as 2.7% and 5.4%, respectively (Figure 9).

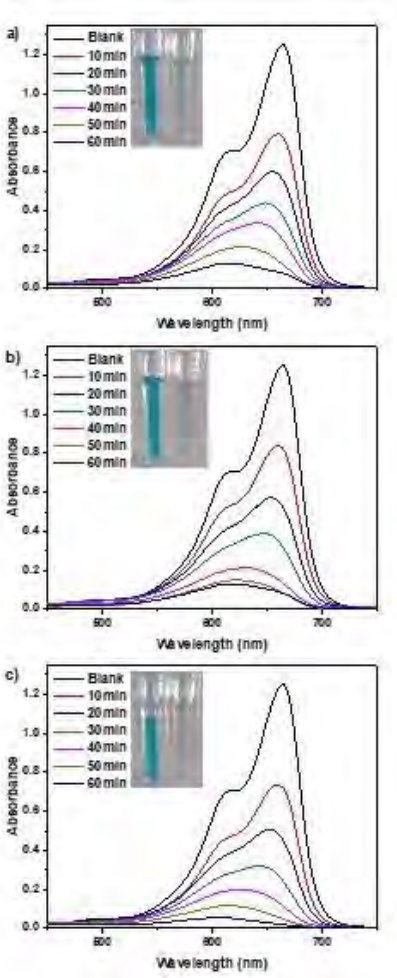

Figure 8 UV-visible absorption spectra for MB in a) gCN, b) gCN-Fe and c) gCN-Zn

In Figure 9, the graph of the decay rates with respect to time is given. In Figure 9, the degradation rates of gCN samples on MB after 60 minutes were determined as 92.7% for gCN, 93.3% for gCN-Fe and 98.4% for gCN-Zn.

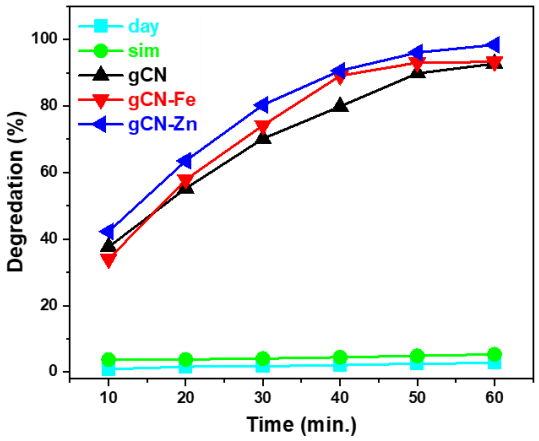

Figure 9 The degradation graph of MB in all samples

It was observed that the synthesized Zn-doped gCN sample was more effective on MB. Figure 10 presents the graph of ln (C_0/C_t) versus time. k (min^{-1}) rate constants (pseudo-first order) were calculated using the slope of the graphs [45]. As can be seen from the graph, the gCN-Zn sample with the highest degradation rate has the largest k value (k=0,06839 min^{-1}).

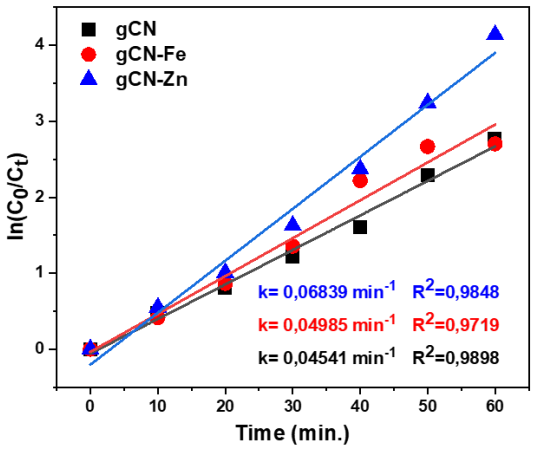

Figure 10 Graph of ln(C_0/C_t) to time gCN, gCN-Fe and gCn-Zn

Photocatalytic evaluation of prepared gCN, gCN-Fe and gCN-Zn samples was investigated through the degradation of MB. gCN-Fe and gCN-Zn were found to exhibit better photocatalytic activity compared to pure gCN. The primary factors of photocatalytic activity are light-absorption capacity, surface composition, and photogenerated charge-separation efficiency [46]. The improvement in photocatalytic activity of gCN-Fe and gCN-Zn composites can be attributed to (i) gCN-Fe and gNC-Zn have a well-developed synergistic interaction in the obtained structure, (ii) a reduction in the bandgap energy of a binary composite can increase the transfer of photo-induced electrons while decreasing electron-hole pair recombination [47, 48]. Zinc oxide absorbe more light quanta than iron oxide and this may the reason of the syhtesized gNC-Zn shows better performance than the gCN-Fe sample [49]. This can increase photocatalytic activity. In addition, the development of photocatalytic activity can be attributed to the promotion of hydroxyl radical formation [40, 41, 50–52].

4. CONCLUSION

In summary, the prisitne gCN, gCN-Zn and gCN-Fe structures were successfully synthesized by the combustion method. The structural properties of the obtained samples were detailly characterized with X-Ray diffraction, SEM-EDX, FTIR and UV-Vis spectroscopy. The bandgap value of pure gCN was found as 2.75 eV and the band gap values of gCN-Zn and gCN-Fe syhtesized binary composites decrease to 2.58 eV and 2.50 eV respectively. The results of the elemental analysis show the apparent differences between the pure forms of gCN, gCN-Zn, and gCN-Fe indicating that syhtesized binary composites have different composition. The obtained FTIR results are comparable with the XRD study, which reveals that the addition of Fe and Zn can cause the graphite structure of gCN to deteriorate. The photocatalytic performances of the synthesized materials were investigated. The degradation effect of synthesized nanocomposites on MB was enhanced with metal ion doping. The obtained results also demonstrated that adding a zinc and iron elements increased the photocatalytic activity remarkably. Among the samples examined, gCN-Zn exhibited the highest photocatalytic performance. The degradation effect of gCN-Zn sample on MB was found to be 98.4% after 60 minutes. The results showed strong photocatalytic effects of Fe and Zn doped gCN structures. Therefore, the prepared gCN-Zn nanocomposite has significant potential and a promising candidate for the destruction of environmental pollutants.

Funding
This work was financially supported by Kahramanmaraş Sütçü İmam University, (KSU) Scientific Research Projects Coordination Department, under Project No. 2021/1-7 YLS and 2020/3-7 YLS.

Authors' Contribution
The authors contributed equally to the study.

The Declaration of Conflict of Interest/ Common Interest
No conflict of interest or common interest has been declared by the authors.

The Declaration of Ethics Committee Approval
This study does not require ethics committee permission or any special permission.

The Declaration of Research and Publication Ethics
The authors of the paper declare that they comply with the scientific, ethical and quotation rules of SAUJS in all processes of the paper and that they do not make any

REFERENCES

[1] S. Kerli, H. Eskalen, "Synthesis of titanium oxide thin films by spray pyrolysis method and its photocatalytic activity for degradation of dyes and ciprofloxacin," Physics and Chemistry of Solid State, vol. 21, no. 3, pp. 426–432, 2020.

[2] H. Eskalen, S. Uruş, Ş. Özgan, "Microwave-Assisted Synthesis of Mushrooms Like MWCNT/SiO2@ZnO Nanocomposite: Influence on Nematic Liquid Crystal E7 and Highly Effective Photocatalytic Activity in Degradation of Methyl Blue," Journal of Inorganic and Organometallic Polymers and Materials, vol. 31, no. 2, pp. 763–775, 2021.

[3] H. Eskalen, H. Yaykaşlı, M. Kavgacı, A. Kayış, "Investigating the PVA/TiO2/CDs polymer nanocomposites: effect of carbon dots for photocatalytic degradation of Rhodamine B," Journal of Materials Science: Materials in Electronics, vol. 33, no. 7, pp. 4643–4658, 2022.

[4] S. Uruş, M. Çaylar, H. Eskalen, Ş. Özgan, "Synthesis of GO@Fe3O4@TiO2 type organic–inorganic nanohybrid material: Investigation of the effect of nanohybrid doped liquid crystal E7 and the photocatalytic degradation of ciprofloxacin," Journal of Materials Science: Materials in Electronics, vol. 33, no. 7, pp. 4314–4329, 2022.

[5] H. Eskalen, S. Kerli, "Synthesis of Gd Doped Tio2 Thin Film for Photocatalytic Degradation of Malachite Green," Sakarya University Journal of Science, vol. 24, no. 6, pp. 1210–1215, 2020.

[6] M. Ikram, F. Jamal, A. Haider, S. Dilpazir, T. Shujah, M. Naz, M. Imran, A. Ul-Hamid, I. Shahzadi, H. Ullah, W. Nabgan, S. Ali, "Efficient Photocatalytic Dye Degradation and Bacterial Inactivation by Graphitic Carbon Nitride and Starch-Doped Magnesium Hydroxide Nanostructures," ACS Omega, p. 2022.

[7] S. Kerli, Ü. Alver, H. Eskalen, S. Uruş, A.K. Soğuksu, "Structural and Morphological Properties of Boron Doped V2O5 Thin Films: Highly Efficient Photocatalytic Degradation of Methyl Blue," Russian Journal of Applied Chemistry 2019 92:2, vol. 92, no. 2, pp. 304–309, 2019.

[8] C. Kursun, M. Gogebakan, H. Eskalen, S. Uruş, J.H. Perepezko, "Microstructural Evaluation and Highly Efficient Photocatalytic Degradation Characteristic of Nanostructured Mg65Ni20Y15−xLax (X = 1, 2, 3) Alloys," Journal of Inorganic and Organometallic Polymers and Materials, vol. 30, no. 2, pp. 494–503, 2020.

[9] H. Eskalen, S. Uruş, H. Yaykaşlı, M. Gögebakan, "Microstructural Characterization of Ball Milled Co60Fe18Ti18Nb4 Alloys and Their Photocatalytic Performance," Alloy Materials and Their Allied Applications, pp. 91–103, 2020.

[10] N. Venkatesh, G. Murugadoss, A.A.A. Mohamed, M.R. Kumar, S.G. Peera, P. Sakthivel, "A Novel Nanocomposite Based on Triazine Based Covalent Organic Polymer Blended with Porous g-C3N4 for Photo Catalytic Dye Degradation of Rose Bengal and Fast Green," Molecules 2022, Vol. 27, Page 7168, vol. 27, no. 21, p. 7168, 2022.

[11] H. Özlü Torun, R. Kırkgeçit, F. Kılıç Dokan, E. Öztürk, "Preparation of La-Dy-CeO2 ternary compound: Examination of photocatalytic and photoluminescence properties," Journal of Photochemistry and Photobiology A: Chemistry, vol. 418, p. 113338, 2021.

[12] M. Atashkadi, A. Mohadesi, M.A. Karimi, S.Z. Mohammadi, V. Haji Aghaei, "Synthesis and characterization of Black Au nanoparticles deposited over g-C_3N_4 nanosheets: enhanced photocatalytic degradation of methylene blue," Environmental Technology, pp. 1–17, 2022.

[13] V. Ugraskan, F. Karaman, "Enhanced thermoelectric properties of highly conductive poly (3,4-ethylenedioxy thiophene)/exfoliated graphitic carbon nitride composites," Synthetic Metals, vol. 287, p. 117070, 2022.

[14] S. Yılmaz, E.G. Acar, G. Yanalak, E. Aslan, M. Kılıç, İ. Hatay Patır, Ö. Metin, "Enhanced hydrogen evolution by using ternary nanocomposites of mesoporous carbon nitride/black phosphorous/transition metal nanoparticles (m-gCN/BP-M; M = Co, Ni, and Cu) as photocatalysts under visible light: A comparative experimental and theoretical study," Applied Surface Science, vol. 593, p. 153398, 2022.

[15] A. Sudhaik, P. Raizada, S. Thakur, A.K. Saini, P. Singh, A. Hosseini-Bandegharaei, "Metal-free photo-activation of peroxymonosulfate using graphene supported graphitic carbon nitride for enhancing photocatalytic activity," Materials Letters, vol. 277, p. 128277, 2020.

[16] G. K. Dutta, N. Karak, "Bio-based waterborne polyester supported oxygeneous graphitic carbon nitride nanosheets as a sustainable photocatalyst for aquatic environment remediation," Journal of Cleaner Production, vol. 285, p. 124906, 2021.

[17] M. S. Khan, F. Zhang, M. Osada, S. S. Mao, S. Shen, "Graphitic Carbon Nitride-Based Low-Dimensional Heterostructures for Photocatalytic Applications," Solar RRL, vol. 4, no. 8, p. 1900435, 2020.

[18] W. Xu, S. Lai, S. C. Pillai, W. Chu, Y. Hu, X. Jiang, M. Fu, X. Wu, F. Li, H. Wang, "Visible light photocatalytic degradation of tetracycline with porous Ag/graphite carbon nitride plasmonic composite: Degradation pathways and mechanism," Journal of Colloid and Interface Science, vol. 574, pp. 110–121, 2020.

[19] V. Balakumar, R. Manivannan, C. Chuaicham, S. Karthikeyan, K. Sasaki, "A simple tactic synthesis of hollow porous graphitic carbon nitride with significantly enhanced photocatalytic performance," Chemical Communications, vol. 57, no. 55, pp. 6772–6775, 2021.

[20] J. Tan, Z. Li, J. Li, Y. Meng, X. Yao, Y. Wang, Y. Lu, T. Zhang, "Visible-light-assisted peroxymonosulfate activation by metal-free bifunctional oxygen-doped graphitic carbon nitride for enhanced degradation of imidacloprid: Role of non-photochemical and photocatalytic activation pathway," Journal of Hazardous Materials, vol. 423, p. 127048, 2022.

[21] D. Gogoi, A. K. Shah, M. Qureshi, A. K. Golder, N. R. Peela, "Silver grafted graphitic-carbon nitride ternary hetero-junction Ag /gC3N4(Urea) -gC3N4 (Thiourea) with efficient charge transfer for enhanced visible-light photocatalytic green H2 production," Applied Surface Science, vol. 558, p. 149900, 2021.

[22] R. Kavitha, P. M. Nithya, S. Girish Kumar, "Noble metal deposited graphitic carbon nitride based heterojunction photocatalysts," Applied Surface Science, vol. 508, p. 145142, 2020.

[23] N. Rono, J. K. Kibet, B. S. Martincigh, V. O. Nyamori, "A comparative study between thermal etching and liquid exfoliation of bulk graphitic carbon nitride to nanosheets for the photocatalytic degradation of a model environmental pollutant, Rhodamine B," Journal of Materials Science: Materials in Electronics, vol. 32, no. 1, pp. 687–706, 2021.

[24] H. Lin, X. Tang, J. Wang, Q. Zeng, H. Chen, W. Ren, J. Sun, H. Zhang, "Enhanced visible-light photocatalysis of clofibric acid using graphitic carbon nitride modified by cerium oxide nanoparticles," Journal of Hazardous Materials, vol. 405, p. 124204, 2021.

[25] A. Hayat, A. G. Al-Sehemi, K. S. El-Nasser, T. A. Taha, A. A. Al-Ghamdi, Jawad Ali Shah Syed, M. A. Amin, T. Ali, T. Bashir, A. Palamanit, J. Khan, W. I. Nawawi, "Graphitic carbon nitride (g–C3N4)–based semiconductor as a beneficial candidate in photocatalysis diversity," International Journal of Hydrogen Energy, vol. 47, no. 8, pp. 5142–5191, 2022.

[26] S. Sivasakthi, K. Gurunathan, "Graphitic carbon nitride bedecked with CuO/ZnO hetero-interface microflower towards high photocatalytic performance," Renewable Energy, vol. 159, pp. 786–800, 2020.

[27] C. Saka, "Phosphorus decorated g-C3N4-TiO2 particles as efficient metal-free catalysts for hydrogen release by NaBH4 methanolysis," Fuel, vol. 322, p. 124196, 2022.

[28] M. U. Rahman, U. Y. Qazi, T. Hussain, N. Nadeem, M. Zahid, H. N. Bhatti, I. Shahid, "Solar driven photocatalytic degradation potential of novel graphitic carbon nitride based nano zero-valent iron doped bismuth ferrite ternary composite," Optical Materials, vol. 120, p. 111408, 2021.

[29] Y. Orooji, M. Ghanbari, O. Amiri, M. Salavati-Niasari, "Facile fabrication of silver iodide/graphitic carbon nitride nanocomposites by notable photo-catalytic performance through sunlight and antimicrobial activity," Journal of Hazardous Materials, vol. 389, p. 122079, 2020.

[30] U. Saeed, A. Jilani, J. Iqbal, H. Al-Turaif, "Reduced graphene oxide-assisted graphitic carbon nitride@ZnO rods for enhanced physical and photocatalytic degradation," Inorganic Chemistry Communications, vol. 142, p. 109623, 2022.

[31] L. Ge, "Synthesis and photocatalytic performance of novel metal-free g-C3N4 photocatalysts," Materials Letters, vol. 65, no. 17–18, pp. 2652–2654, 2011.

[32] H. Zou, X. Yan, J. Ren, X. Wu, Y. Dai, D. Sha, J. Pan, J. Liu, "Photocatalytic activity enhancement of modified g-C3N4 by ionothermal copolymerization ," Journal of Materiomics, vol. 1, no. 4, pp. 340–347, 2015.

[33] D. R. Paul, S. Gautam, P. Panchal, S. P. Nehra, P. Choudhary, A. Sharma, "ZnO-Modified g-C3N4: A Potential Photocatalyst for Environmental Application," ACS Omega, vol. 5, no. 8, pp. 3828–3838, 2020.

[34] J. Hu, P. Zhang, W. An, L. Liu, Y. Liang, W. Cui, "In-situ Fe-doped g-C3N4 heterogeneous catalyst via photocatalysis-Fenton reaction with enriched photocatalytic performance for removal of complex wastewater," Applied Catalysis B: Environmental, vol. 245, pp. 130–142, 2019.

[35] M. Piri, M. M. Heravi, A. Elhampour, F. Nemati, "Silver nanoparticles supported on P, Se-codoped g-C3N4 nanosheet as a novel heterogeneous catalyst for reduction of nitroaromatics to their corresponding amines," Journal of Molecular Structure, vol. 1242, p. 130646, 2021.

[36] J. Hu, P. Zhang, W. An, L. Liu, Y. Liang, W. Cui, "In-situ Fe-doped g-C3N4 heterogeneous catalyst via photocatalysis-Fenton reaction with enriched photocatalytic performance for removal of complex wastewater," Applied Catalysis B: Environmental, vol. 245, pp. 130–142, 2019.

[37] Y. Oh, J.O. Hwang, E.S. Lee, M. Yoon, V.D. Le, Y.H. Kim, D.H. Kim, S.O. Kim, "Divalent Fe Atom Coordination in Two-Dimensional Microporous Graphitic Carbon Nitride," ACS Applied Materials and Interfaces, vol. 8, no. 38, pp. 25438–25443, 2016.

[38] C. Liu, H. Huang, W. Cui, F. Dong, Y. Zhang, "Band structure engineering and efficient charge transport in oxygen substituted g-C3N4 for superior photocatalytic hydrogen evolution," Applied Catalysis B: Environmental, vol. 230, pp. 115–124, 2018.

[39] M. A. Mohamed, M. F. M. Zain, L. Jeffery Minggu, M. B. Kassim, N. A. Saidina Amin, W. N. W. Salleh, M. N. I. Salehmin, M. F. Md Nasir, Z. A. Mohd Hir, "Constructing bio-templated 3D porous microtubular C-doped g-C3N4 with tunable band structure and enhanced charge carrier separation," Applied Catalysis B: Environmental, vol. 236, pp. 265–279, 2018.

[40] S. Babar, N. Gavade, H. Shinde, A. Gore, P. Mahajan, K. H. Lee, V. Bhuse, K. Garadkar, "An innovative transformation of waste toner powder into magnetic g-C3N4-Fe2O3 photocatalyst: Sustainable e-waste management," Journal of Environmental Chemical Engineering, vol. 7, no. 2, p. 103041, 2019.

[41] S. Liu, S. Wang, Y. Jiang, Z. Zhao, G. Jiang, Z. Sun, "Synthesis of Fe2O3 loaded porous g-C3N4 photocatalyst for photocatalytic reduction of dinitrogen to ammonia," Chemical Engineering Journal, vol. 373, pp. 572–579, 2019.

[42] C. Daikopoulos, Y. Georgiou, A. B. Bourlinos, M. Baikousi, M. A. Karakassides, R. Zboril, T. A. Steriotis, Y. Deligiannakis, "Arsenite

remediation by an amine-rich graphitic carbon nitride synthesized by a novel low-temperature method," Chemical Engineering Journal, vol. 256, pp. 347–355, 2014.

[43] Y. Yang, J. Chen, Z. Mao, N. An, D. Wang, B. D. Fahlman, "Ultrathin g-C 3 N 4 nanosheets with an extended visible-light-responsive range for significant enhancement of photocatalysis," RSC Advances, vol. 7, no. 4, pp. 2333–2341, 2017.

[44] H. Leelavathi, R. Muralidharan, N. Abirami, S. Tamizharasan, A. Kumarasamy, R. Arulmozhi, "Exploration of ZnO decorated g-C3N4 amphiphilic anticancer drugs for antiproliferative activity against human cervical cancer," Journal of Drug Delivery Science and Technology, vol. 68, p. 103126, 2022.

[45] A. K. Soğuksu, S. Kerli, M. Kavgacı, A. Gündeş, "Electrochemical Properties, Antimicrobial Activity and Photocatalytic Performance of Cerium-Iron Oxide Nanoparticles," Russian Journal of Physical Chemistry A, vol. 96, no. 1, pp. 209–215, 2022.

[46] F. Shi, L. Chen, C. Xing, D. Jiang, D. Li, M. Chen, "ZnS microsphere/g-C3N4 nanocomposite photo-catalyst with greatly enhanced visible light performance for hydrogen evolution: synthesis and synergistic mechanism study," RSC Advances, vol. 4, no. 107, pp. 62223–62229, 2014.

[47] S. Iqbal, A. Bahadur, S. Ali, Z. Ahmad, M. Javed, R. M. Irfan, N. Ahmad, M. A. Qamar, G. Liu, M. B. Akbar, M. Nawaz, "Critical role of the heterojunction interface of silver decorated ZnO nanocomposite with sulfurized graphitic carbon nitride heterostructure materials for photocatalytic applications," Journal of Alloys and Compounds, vol. 858, p. 158338, 2021.

[48] S. Le, T. Jiang, Y. Li, Q. Zhao, Y. Li, W. Fang, M. Gong, "Highly efficient visible-light-driven mesoporous graphitic carbon nitride/ZnO nanocomposite photocatalysts," Applied Catalysis B: Environmental, vol. 200, pp. 601–610, 2017.

[49] S. Sakthivel, B. Neppolian, M. v. Shankar, B. Arabindoo, M. Palanichamy, V. Murugesan, "Solar photocatalytic degradation of azo dye: comparison of photocatalytic efficiency of ZnO and TiO2," Solar Energy Materials and Solar Cells, vol. 77, no. 1, pp. 65–82, 2003.

[50] H. Xing, H. Ma, Y. Fu, M. Xue, X. Zhang, X. Dong, X. Zhang, "Preparation of g-C3N4/ZnO composites and their enhanced photocatalytic activity," Materials Technology, vol. 30, no. 2, pp. 122–127, 2015.

[51] Q. Zhong, H. Lan, M. Zhang, H. Zhu, M. Bu, "Preparation of heterostructure g-C3N4/ZnO nanorods for high photocatalytic activity on different pollutants (MB, RhB, Cr(VI) and eosin)," Ceramics International, vol. 46, no. 8, pp. 12192–12199, 2020.

[52] X. Li, M. Li, J. Yang, X. Li, T. Hu, J. Wang, Y. Sui, X. Wu, L. Kong, "Synergistic effect of efficient adsorption g-C3N4/ZnO composite for photocatalytic property," Journal of Physics and Chemistry of Solids, vol. 75, no. 3, pp. 441–446, 2014.

ISSN 1070-3632, Russian Journal of General Chemistry, 2023, Vol. 93, No. 8, pp. 2152–2160. © Pleiades Publishing, Ltd., 2023.

Carbon Quantum Dot (CQD) Nanoparticles Synthesized by Sucrose and Urea: Application as Reinforcement Effect on Al–Mg–Cu–Zn Composite

M. Aslan[a,*], H. Eskalen[b,d], and M. Kavgaci[c,d]

[a] *Department of Metallurgical and Material ScienceEngineering, Gaziantep University, Gaziantep, 27310 Turkey*
[b] *Vocational School of Health Services, Department of Opticianry, Kahramanmaras Sutcu Imam University, Kahramanmaraş, 46050 Turkey*
[c] *Elbistan Vocational School of Health Services, Department of Opticianry, Kahramanmaras Istiklal University, Kahramanmaraş, 46100 Turkey*
[d] *Material Science and Engineering, Institute of Science, Kahramanmaraş Sütçü İmam University, Kahramanmaraş, 46050 Turkey*
**e-mail: mikailsln@gmail.com*

Received May 28, 2023; revised August 4, 2023; accepted August 8, 2023

Abstract—Water-soluble carbon quantum dot (CQD) nanoparticles were synthesized using a one-step hydrothermal method, with sucrose and urea selected as carbon precursors. The synthesized CQDs were characterized through SEM, TEM, X-ray diffraction, UV-Vis spectrum, FTIR, and fluorescence spectra analyses. HR-TEM results revealed the microstructure of CQDs as spherical-shaped particles, while XRD plots indicated their amorphous nature. XPS analysis confirmed the successful synthesis of N-doped CQDs. Moreover, this study introduced the reinforcing effect of CQD nanoparticles for the Al composites. The incorporation of CQD particles led to improved hardness properties of the Al–Zn–Mg–Cu composites by using Vickers tester. Additionally, SEM results suggested that CQD particles contributed to a grain fining effect, thereby reducing grain boundary separation.

Keywords: carbon quantum dots, new carbon materials, hydrothermal method, carbon nanodot reinforced Al–Mg–Zn–Cu composite, Al composites

DOI: 10.1134/S1070363223080236

INTRODUCTION

Recently, carbon quantum dots (CQDs) have attracted increasing attention due to their extraordinary properties. CQDs are alternatives for semiconductor quantum dots (SCDs). CQDs have many advantages compared to SCDs, such as outstanding optical properties, low toxicity, high stability, water solubility, and good biocompatibility [1, 2]. These lead to use in bioimaging, optical sensing, optoelectronics, light-emitting diodes, solar cells, displays, photocatalysis, supercapacitors, food packaging, and drug delivery applications [3–5]. Pyrolysis, microwave-assisted methods, ultrasound, and hydrothermal treatment are some examples of synthesizing CQDs. Among them, the hydrothermal method is commonly used for its simplicity, energy efficiency, and economic and practical approach to generating cost-efficient and nontoxic carbon dots [6–9].

Superior nanosized materials reinforced composite materials play a crucial role, but these materials are often quite expensive to produce [10]. Here, carbon-based nanostructures, especially carbon quantum dots can be produced cheaply. Aluminum matrix composites (AMCs) are obtained by incorporating a specific content of reinforcement phase into Al or Al alloy matrix [11]. In literature, 0.2 wt % graphane is used as a reinforcement material for $AlSi_{10}Mg$ alloy, and the hardness improved by approximately 30% [11]. Another study revealed that the hardness of aluminum matrix composite with 0.5 wt % graphenes was enhanced by 41.7% compared to pristine

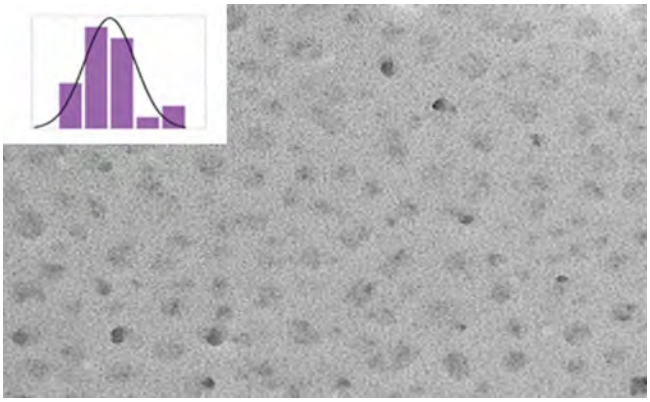

Fig. 1. The TEM image of the prepared CQDs (inset particle size distribution).

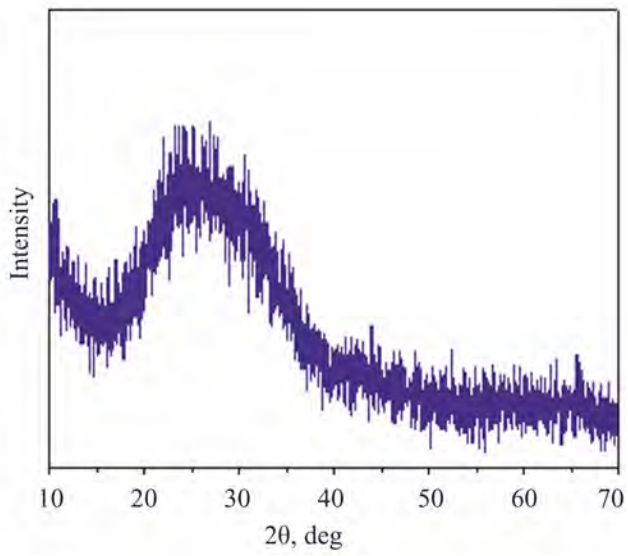

Fig. 2. The XRD pattern of the carbon dots.

aluminum [12]. The thermal expansion coefficient (CTE) of aluminum matrix composite reinforced with 1.0 wt % multiwall carbon nanotubes (MWCNT) decreased by 12% [13]. Dorbani et al. reported that introducing 0.25% MWCNT to aluminum resulted in significant changes in structural and thermodynamic properties [10]. The addition of 1.5 wt % carbon nanotubes to the aluminum matrix resulted in a threefold increase in microhardness [14]. The remarkable increase in hardness of the aluminum-graphane (0.2 wt %) composite was reported from 65±0.5 VHN to 165±0.8 VHN [15]. Carbon nanotube-reinforced Al composite was fabricated and the hardness of the system was enhanced from 83±2 to 117±4 HV [15]. The CQDs/Copper (Cu) composite was synthesized, and the mechanical strength of 0.4 wt % CQD/Cu composite increased up to 47% relative to pure Cu [16]. Another study is related to 0.2 wt % CQDs/Cu composite tensile strength which was enhanced by about 31% [17]. The ultra-tensile strength of 0.2 CQDs/Cu composite is improved by about 17% in the study [18].

In this study, carbon quantum dots (CQDs) were synthesized using sucrose and urea as precursors. The hydrothermal method was chosen for CQD synthesis due to its simplicity and energy efficiency. Furthermore, this study introduced the utilization of carbon dots as reinforcement particles.

RESULTS AND DISCUSSION

Carbon quantum dots. Figure 1 displays the transmission electron microscopy (TEM) image, revealing the synthesized carbon quantum dot (CQD) nanoparticles. The TEM image showcases spherical-shaped structures, characteristic of the CQDs' morphology. Through the image analysis, the average particle size of the CQD nanoparticles was determined to be 28.18 nm, with a standard deviation of 5.87 nm. This statistical analysis provides valuable information about the size distribution and homogeneity of the synthesized nanoparticles.

The XRD patterns of the particles were scanned in the 2θ range of 10 to 70°. No sharp peaks are observed in Fig. 2, which means the structure of the carbon dots (CDs) is amorphous type. This has also been observed in previous studies of CDs synthesized with different carbon sources [19, 20]. A single broad peak observed on the XRD graph is centered at around 2θ = 25°. The peak at 25° corresponds to the crystal lattice spacing (002), which is a fundamental characteristic of carbon nanomaterials [21].

The elemental analysis and surface composition of the synthesized CDs were characterized by X-ray photoelectron spectroscopy (XPS). As seen in Fig. 3, there are peaks at 282 eV, 397 eV, and 529 eV, indicating C1s,

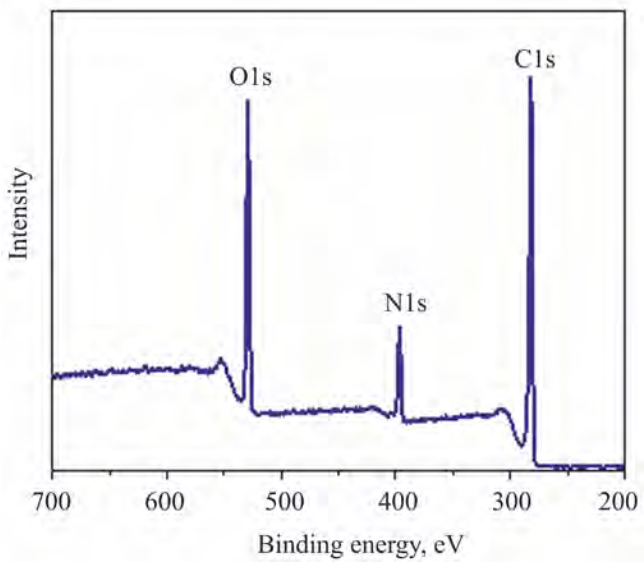

Fig. 3. The X-ray photoelectron spectrum (XPS) of the carbon dots.

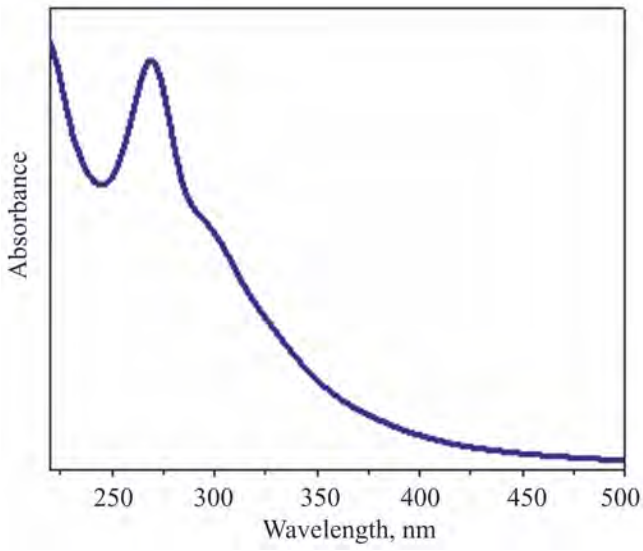

Fig. 4. The UV-vis spectra of the carbon dot solutions.

N1s, and 01s, respectively, which means that *N*-doped CQDs were synthesized [22–24].

Figure 4 depicted that the synthesized CDs give a characteristic absorption peak at 269 nm in the UV spectrum, which was attributed to the *n*–π* transition of the C=O band and the π–π* transition of the conjugated C=C bond [25].

The PL spectra of the CQDs solutions are given in Fig. 5. When excitation is at 350 nm, the CDs exhibit maximum emission at 432 nm (see Fig. 5a). PL spectra at various excitation wavelengths ranging from 300 to 600 nm (Fig. 5b). It was observed that the emission peak red-shifted from 411 to 506 nm when the excitation wavelength was increased from 300 nm to 450 nm. The redshift observed in the emission spectrum reveals the possibility of adjusting the PL emission color so the excitation wavelength creates a variety of emission spectra. With the increase in the excitation wavelength, the fluorescence intensity decreases and weakens.

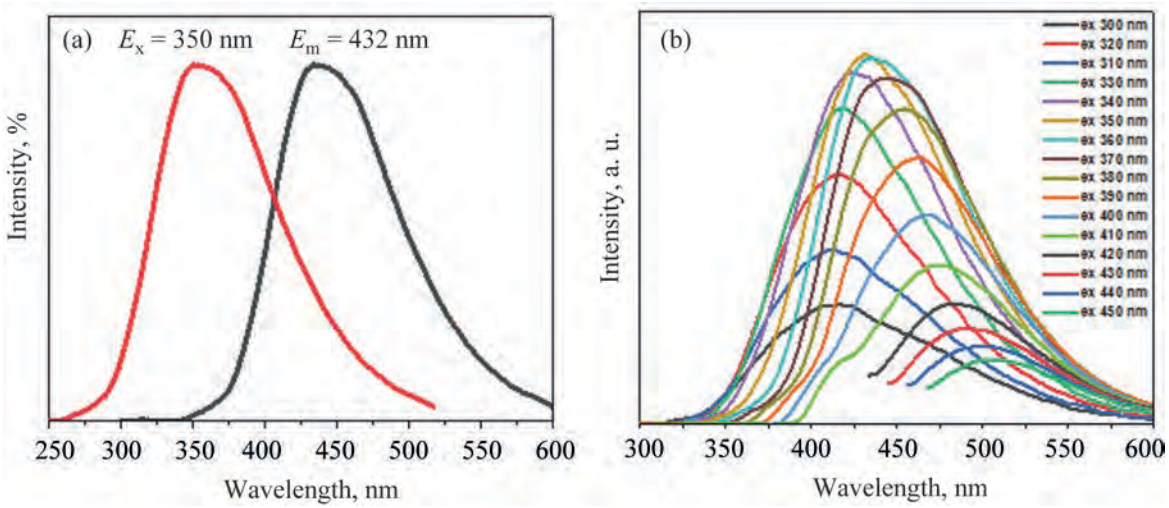

Fig. 5. The PL excitation and PL emission spectrum of the carbon dots (a), and the corresponding excitation-depended PL emission spectra for the carbon dots (b).

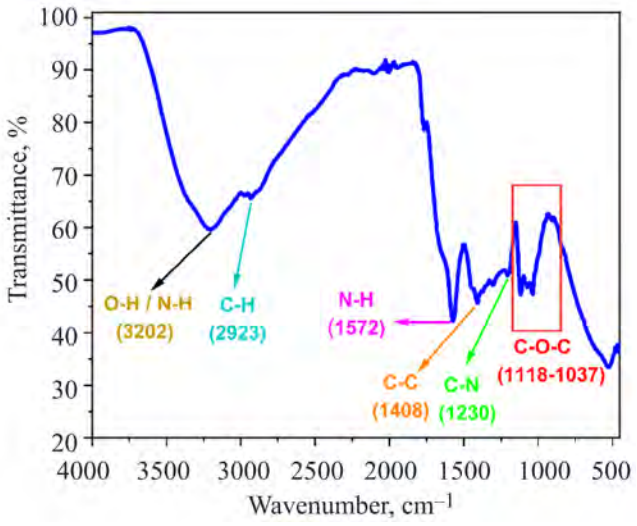

Fig. 6. The FTIR spectra of the synthesized carbon dots.

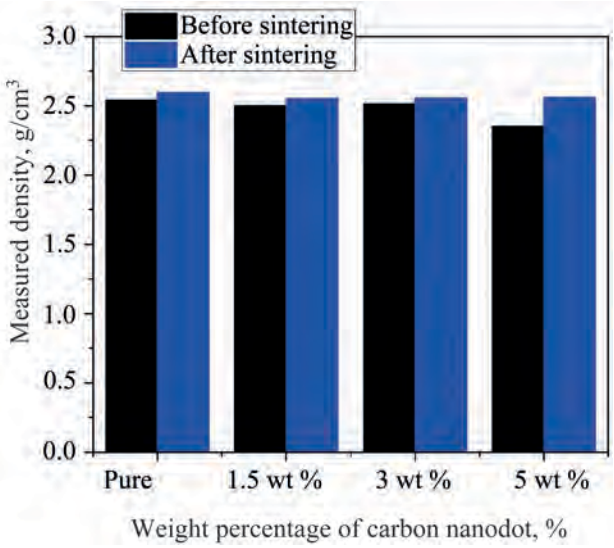

Fig. 7. The measured densities of the composites according to their carbon nanodot weight percentages.

The functional groups on CQD nanoparticles were examined by the FTIR spectrum (Fig. 6). The O-H (broad) and N–H (stretching) bands were observed on the peak of 3202 cm^{-1}. The stress vibrations of C–H (stretching) were seen at 2923 cm^{-1} [26].The peaks at 1572 cm^{-1} correspond to N–H bending vibrations [27]. The absorptions at 1037–1118 cm^{-1} show the existence of C–O–C groups in the CDs [28]. The peaks at 1400 and 1230 cm^{-1} can be attributed to the C–C and C–N bonds [29].

Al–Zn–Mg–Cu composites reinforced with the carbon nanodots. Al (99.9% purity, ~44 μm), Zn (99.8% purity, ~44 μm), Mg (99.9% purity, ~100 μm), and Cu (99.9% purity, ~44 μm) powders were purchased from Nanografi Co., Ltd. and ethyl alcohol (99% purity) was provided by Isolab Chemicals. The chemical composition of Al–Zn–Mg–Cu alloy is presented below. To produce the CQDs-reinforced Al–Zn–Mg–Cu composites, 1.5, 3, and 5 wt % of CQDs were additionally mixed with the Al alloy.

Element	Al	Zn	Mg	Cu
wt %	90.5	5.5	2.4	1.6

The densities of the composites were obtained by the Archimedes principle, including the stages of weighing the composite first in the air and then in distilled water. The measured densities of the composites in terms of the weight percentages of the CQDs are shown in Fig. 7. The density of the samples decreased with increasing the weight percentages of the CQDs. This kind of behavior may be associated with the agglomerations of CQD particles and act as a porosity which results in the composite density diminishing. This may also be attributed to the lower density of the carbon nanodot than those of the constituent elements of the aluminum alloy. The same results were observed in the study conducted by Garg et al. [30]. In their study, the density of the graphene-reinforced aluminum composites was lower when compared to the pure form. Differently, the density of the composite with 3 wt % of the CQDs is higher than those of the other CQDs reinforced composites but lower than that of pure one. This may be due to the lower intergranular friction forces between CQDs and other elements. This is also supported by the hardness results since the 3 wt % of the CQDs reinforced composites has higher hardness values before the sintering process. After the sintering process, as expected, due to the decrease in the porosities of the structures, the densities of the composites increase. The efficiency of the sintering process was seen mainly on the structure of the 5 wt % of the CQDs reinforced composites (Fig. 7). This means that the sintering process leads to a considerable decrease in the porosity of these structures.

Before testing the specimens, metallographic processes were applied as sanding, polishing, and etching, respectively. The sanding method was applied to the

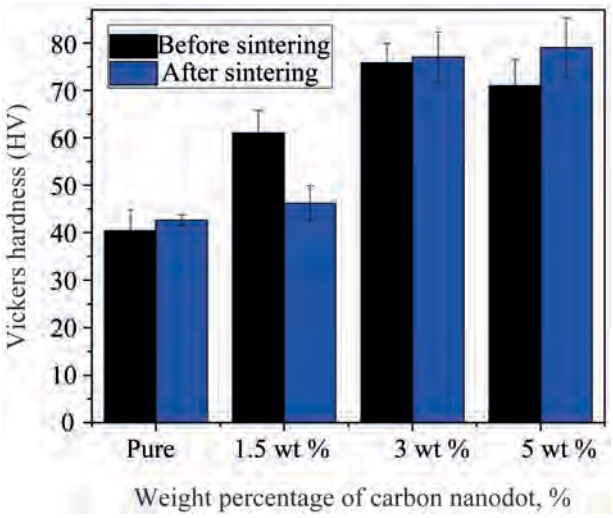

Fig. 8. The microhardness values of the composites according to their carbon nanodot weight percentages.

surfaces of the samples with 600, 1000, and 2000 mesh sanders, respectively. Then, the surfaces of the samples were polished with 6 and 3 μ diamond suspensions, respectively. Finally, the specimens were subjected to the etching process by the dipping method. Keller's reagent (95 mL water, 2.5 mL HNO_3, 1.5 mL HCl, 1.0 mL HF), a popular general-purpose reagent for Al alloys and composites, was used as an etching agent. To examine the mechanical properties of the studied composites, measurements were carried out using an AOB Vickers Microhardness tester with a load of 0.5 kg and 15 s of dwell time. At least five indentations were made for each hardness measurement, and the average hardness values were reported. The Vicker hardness values of the given composites are reported in Fig. 8. Results indicate that introducing CQD particles into the matrix results

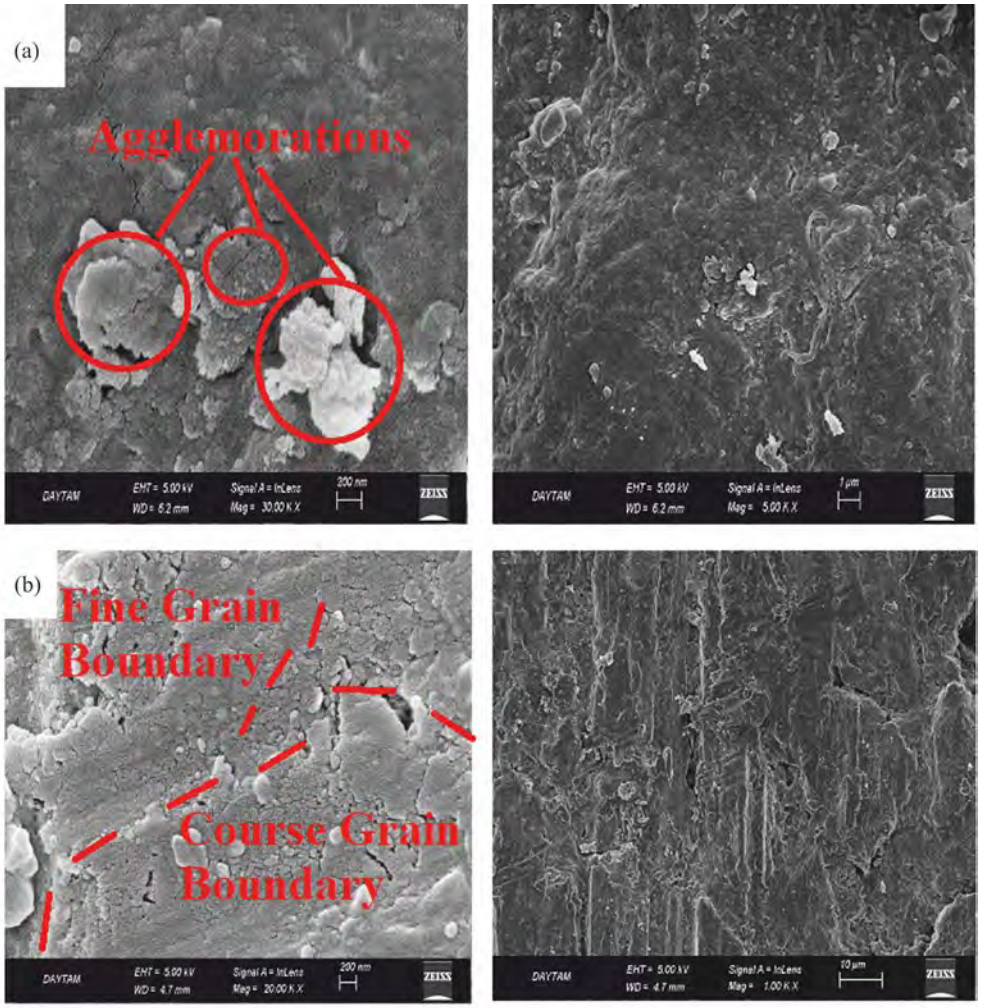

Fig. 9. The SEM images of the composites with 0 (a) and 1.5 wt % (b) of CDs respectively.

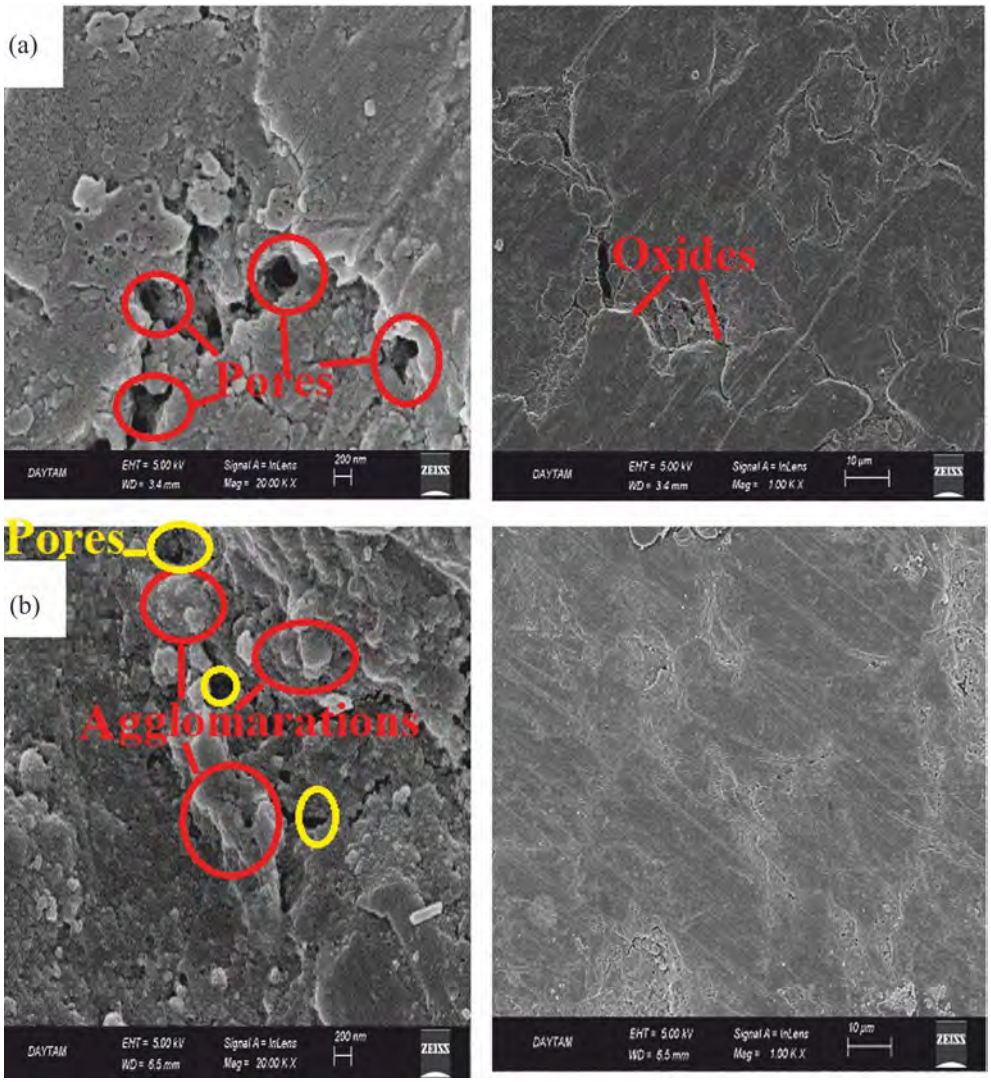

Fig. 10. The SEM images of the composites with 3 (a) and 5 wt % (b) of CQDs, respectively.

in incrementing the Vickers microhardness values. On the other hand, before the sintering process, the highest value was not seen on the 5 wt % of the CQDs reinforced composites. In this structure, this was caused by the agglomerated CQDs, which hindered the particle-particle contact and gave rise to insufficient bonding between the matrix and the CQDs. This leads to higher porosity and causes a decrease in hardness, but after the sintering process, the effect of the aggregation relatively decreases, especially in this structure (Fig. 8).

The SEM images of the composites with the reinforcements of 0, 1.5, 3, and 5 wt % of CQD nanoparticles, respectively, are given in Figs. 9 and 10. The agglomerations reducing the hardness are observed in the pure form of the composite (Fig. 9a). The CQDs addition in the composites may lead to the grain fining effect, which reduces the grain boundary separation. This can be seen clearly in Fig. 9b. Excellent grains are formed and long grain boundary separation can also be observed in this structure. Figures 10a and 10b depict the formations of the pores. Furthermore, oxidations are predominant effects on the microstructure of all structures.

The produced nanostructured composite was examined with EDX to determine the compositional homogeneity. Fig. 11 shows the EDX analysis of the alloy. It is seen in Fig. 11 that there are Al, Mg, Cu, Zn, and C elements in the produced alloy. In addition, the composition of the alloy is close to the initial ratio of the composite, revealing

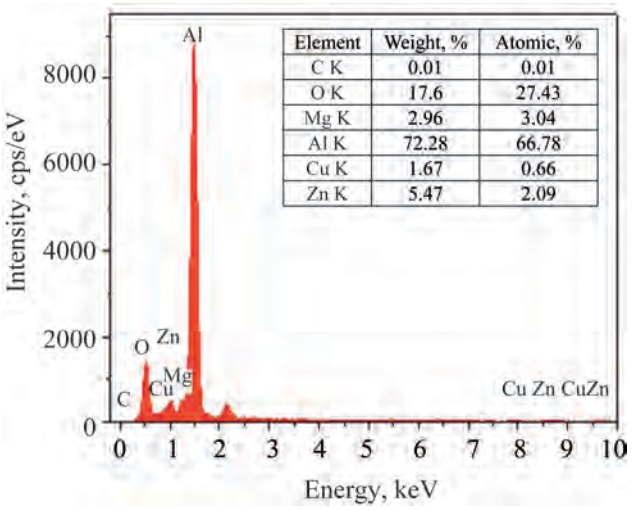

Element	Weight, %	Atomic, %
C K	0.01	0.01
O K	17.6	27.43
Mg K	2.96	3.04
Al K	72.28	66.78
Cu K	1.67	0.66
Zn K	5.47	2.09

Fig. 11. The EDX graph of nanostructured composite.

that all elements and carbon are included in the alloy without significant loss.

CONCLUSION

The present study presents a green and facile hydrothermal approach for synthesizing carbon dots and producing CQD nanoparticle-reinforced Al–Mg–Zn–Cu composites using a powder metallurgy routine. In this synthesis, sucrose and urea were used as natural carbon sources, eliminating the need for any chemical additives or complicated post-treatment. TEM results indicate an average particle size of 28.18±5.87 nm for the CQDs. XRD analysis shows a single broad peak at around $2\theta = 25°$, corresponding to the crystal lattice spacing (002), which is a fundamental characteristic of carbon nanomaterials. XPS analysis confirms the efficiency of the produced *N*-doped CQDs. The CQDs-reinforced Al–Zn–Mg–Cu composites were produced through mechanical alloying. The composite density with 3 wt % CQDs is higher than that of the other composites and lower than the pure form, likely due to lower intergranular friction forces. Before the sintering process, the composite with 3 wt % CQDs exhibited the highest microhardness value, while after the sintering process, the highest value was observed in the composite with 5 wt % CQDs. The sintering process had a significant effect on the structure of the 5 wt % CQDs-reinforced Al–Zn–Mg–Cu composites, leading to a considerable decrease in the aggregation of this structure. Moreover, the incorporation of CQDs in the composites may induce a grain refining effect, reducing the grain boundary separation.

EXPERIMENTAL

The transmission electron microscope images of the carbon dots were obtained using a Hitachi HT7700 with EXALENS operating at 120 kV. The X-ray diffraction analysis was performed on a Philips X'Pert PRO XRD instrument with CuK_α radiation ($\lambda = 0.154056$ nm, set at 40 kV and 30 mA). The UV-Vis absorption spectra were recorded using a Shimadzu UV-Vis 1800 spectrometer. The X-Ray photoelectron spectroscopy (XPS) measurements were obtained on a Specs-Flex Mod electron spectrometer, utilizing a monochromatized AlK_α excitation source. The FTIR spectroscopy analyses were performed with a PerkinElmer Spectrum 400 in the range of 4000–500 cm^{-1}. The photoluminescence (PL) spectrum was measured using the Varian Cary Eclipse spectrometer. The microstructures of the studied materials were examined with a ZEISS EVO LS10 scanning electron microscope.

Preparation of the carbon dots. Carbon quantum dots were synthesized using a hydrothermal reaction method with sucrose and urea as the carbon sources purchased, from AFG Bioscience and Tekkim, respectively. Distilled water was served as the solvent. To synthesize the carbon quantum dots, 2.95 g of sucrose was dissolved in 250 mL of distilled water, followed by the addition and mixing of 2.05 g of urea. The resulting mixture was then sealed in a teflon container and transferred to a steel autoclave. The hydrothermal reaction was carried out at 180°C for 10 h. Finally, the synthesized carbon quantum dot solution was separated and purified using filtration and a centrifuge instrument.

Preparation of the aluminum composite. Carbon nanodot-reinforced aluminum alloy composites, with a composition similar to 7075 aluminum alloy, were produced using the powder metallurgy (PM) technique. Elemental powder precursors of Al, Zn, Mg, Cu, and carbon nanodots served as starting materials. Mechanical alloying (MA) was conducted in a planetary high-energy ball mill (Retsch PM 100) equipped with 120 mL stainless steel grinding jars.

In the initial stage, the planetary ball mill (PM) was operated without any balls for 30 min to ensure the homogeneous distribution of raw elemental powders during mechanical alloying. The rotation speed was set at 150 rpm with direction reversal every 2 min.

Subsequently, in the second stage, to alloy the Al, Zn, Mg, and Cu powders, the planetary ball mill was used for a 2 h working period, employing 10 mm diameter stainless steel balls. The ball-powder weight ratio was maintained at 3 : 1, with a speed of 150 rpm and direction reversal every 5 min. To prevent overheating, the PM was stopped for 2 min after every 5 min of working period. Furthermore, 5 mL of ethanol was used as a process control agent (PCA). In the final stage, the 5 mL CQD solutions with the specified weight percentages were added to the grinding jar. The composite was synthesized in a planetary ball mill for 2.5 h, operating at a speed of 100 rpm with a ball-powder weight ratio of 1 : 1. Direction reversal occurred every 5 min, and the ball milling was paused for 2 min after each 5 min run to prevent overheating.

The obtained powders were subsequently dried in oven at 100°C for 24 h. To ensure a homogeneous distribution, the powder samples were mixed for 10 min using mechanical stirring and then cold-pressed in a steel die at 200 MPa to form bulk alloy representations. Finally, the bulk samples were sintered in a furnace at 400°C for 2 h, followed by immediate cooling to room temperature.

FUNDING

This study was supported by the Scientific Research Projects Coordination Unit of Kahramanmaraş Sütçü İmam University and Gaziantep University (project no. 2023/2-22 A and MF. DT.20.06, respectively).

CONFLICT OF INTEREST

The authors declare no conflict of interests.

REFERENCES

1. Dinç, S., Kara, M., and Yavuz, E., *Carbon Dots in Agricultural Systems*, Elsevier, 2022, p. 69.
2. Kaur, R., Singh, J., Kathuria, D., and Matharu, A.S., *Sust. Chem. Pharm*., 2022, vol. 29, p. 100813. https://doi.org/10.1016/j.scp.2022.100813
3. Kir, Ş., Dehri, İ., Önal, Y., Esen, R., and Başar, C.A., *Surf. Interfaces*, 2022, vol. 29, p. 101679. https://doi.org/10.1016/j.surfin.2021.101679
4. Rohde, L.E., Clausell, N, Pinto Ribeiro, J., Goldraich, L., Netto, R., Dec, G.W., DiSalvo, T.G., and Polanczyk, C.A., *Int. J. Cardiol*., 2005, vol. 102, p. 71. https://doi.org/10.1016/j.ijcard.2004.04.006
5. Şen, F.B., Beğiç, N., Bener, M., and Apak, R., *Spectrochim. Acta (A)*, 2022, vol. 271, p. 120884. https://doi.org/10.1016/j.saa.2022.120884
6. Radnia, F., Mohajeri, N., and Zarghami, N., *Talanta*, 2020, vol. 209, p. 120547. https://doi.org/10.1016/j.talanta.2019.120547
7. Polatoğlu, B. and Bozkurt, E., *Res. Chem. Intermed.*, 2021, vol. 47, p. 1865. https://doi.org/10.1007/s11164-021-04404-y
8. Eskalen, H., Uruş, S., Kavgacı, M., Kalmış, H.V., and Tahta, B., *Biomass Conv. Bioref.,* 2023, p. 1. https://doi.org/10.1007/s13399-023-04048-5
9. Başkaya, S.K., Tahta, B., Uruş, S., Eskalen, H., Çeşme, M., and Özğan, Ş., *Biomass Conv. Bioref.*, 2022, p. 1. https://doi.org/10.1007/s13399-022-03017-8
10. Dorbani, T., Bouleklab, M.C., Settar, A., Chetehouna, K., Naoui, Y., Revo, S., and Hamamda, S., *J. Mater. Res. Technol.*, 2022, vol. 19, p. 1484. https://doi.org/10.1016/j.jmrt.2022.05.111
11. Tiwari, J.K., Mandal, A., Sathish, N., Agrawal, A.K., and Srivastava, A.K., *Addit. Manuf.,* 2020, vol. 33, p. 101095. https://doi.org/10.1016/j.addma.2020.101095
12. Wang, F., Liu, H., Liu, Z., Guo, Z., and Sun, F., *Sci. Rep*., 2022, vol. 12, p. 9561. https://doi.org/10.1038/s41598-022-13793-y
13. Deng, C., Ma, Y., Zhang, P., Zhang, X., and Wang, D., *Mater. Lett.*, 2008, vol. 62, p. 2301. https://doi.org/10.1016/j.matlet.2007.11.086
14. Abdullahi, U., Maleque, M.A., and Ali, M.Y., *Mater. Today Proc.*, 2021, vol. 46, p. 6097. https://doi.org/10.1016/j.matpr.2020.03.333
15. Palei, B.B., Dash, T., and Biswal, S.K., *J. Mater. Sci.*, 2022, vol. 57, p. 8544. https://doi.org/10.1007/s10853-022-07043-9
16. Zhao, W., Bao, R., Yi, J., Tao, J., Guo, S., and Tan, S., *Mater. Sci. Eng. (A)*, 2021, vol. 805, p. 140573. https://doi.org/10.1016/j.msea.2022.143222
17. Huang, X., Bao, R., and Yi, J.-h., *J. Cent. South Univ.*, 2021, vol. 28, p. 1255. https://doi.org/10.1007/s11771-021-4693-y
18. Zhao, W.-m., Bao, R., and Yi, J.-h., *J. Mater. Sci.*, 2021, vol. 56, p. 12753. https://doi.org/10.1007/s10853-021-06116-5
19. Eskalen, H., Çeşme, M., Kerli, S., and Özğan, Ş., *J. Chem. Res.*, 2021, vol 45, p. 428. https://doi.org/10.1177/1747519820953823

20. Aslan, M. and Eskalen, H., *Fuller. Nanotub. Carbon Nanostructures*, 2021, vol. 29, p. 1026. https://doi.org/10.1080/1536383X.2021.1926452
21. Lin, H., Ding, L., Zhang, B., and Huang, J., *R. Soc. Open Sci.*, 2018, vol. 5, p. 172149. https://doi.org/10.1098/rsos.172149
22. Eskalen, H., *Appl. Phys. (A)*, 2020, vol. 126, p. 708. https://doi.org/10.1007/s00339-020-03906-7
23. Pandiyan, S., Arumugam, L., Srirengan, S.P., Pitchan, P., Sevugan, S., Kannan, K., Pitchan, G., Hegde, T.A., and Gandhirajan, V., *ACS Omega*, 2020, vol. 5, p. 30363. https://doi.org/10.1021/acsomega.0c03290
24. Swapna, M. and Sankararaman, S., *Int. J. Mater. Sci.*, 2017, vol. 12, p. 541. https://doi.org/10.1088/2053-1591/aaa656
25. Xu, X., Chen, Z., Li, Q., Meng, D., Jiang, H., Zhou, Y., Feng, S., and Yang, Y., *Microchem. J.*, 2021, vol. 160, p. 105708. https://doi.org/10.1016/j.microc.2020.105708
26. Azizi, Z., Alamdari, A., and Doroodmand, M.M., *J. Therm. Anal. Calorim.*, 2018, vol. 133, p. 951. https://doi.org/10.1007/s10973-018-7293-9
27. Gedda, G., Lee, C.-Y., Lin, Y.-C., and Wu, H.-f., *Sens. Actuators (B)*, 2016, vol. 224, p. 396. https://doi.org/10.1016/j.snb.2015.09.065
28. Ma, X., Li, S., Hessel, V., Lin, L., Meskers, S., and Gallucci, F., *Chem. Eng. Sci.*, 2020, vol. 220, p. 115648. https://doi.org/10.1016/j.ces.2020.115648
29. Asgari, M., Khanahmad, H., Motaghi, H., Farzadniya, A., Mehrgardi, M.A., and Shokrani, P., *Appl. Phys. (A)*, 2021, vol. 127, p. 1. https://doi.org/10.1007/s00339-020-04171-4
30. Garg, P., Gupta, P., Kumar, D., and Parkash, O., *J. Mater. Environ. Sci.*, 2016, vol. 7, p. 1461. https://doi.org/10.1016/j.jmrt.2019.06.028

Applied Radiation and Isotopes 198 (2023) 110858

Contents lists available at ScienceDirect

Applied Radiation and Isotopes

journal homepage: www.elsevier.com/locate/apradiso

Preparation and study of radiation shielding features of ZnO nanoparticle reinforced borate glasses

Hasan Eskalen [a,d,*], Yusuf Kavun [b,d], Mustafa Kavgacı [c,d]

[a] Vocational School of Health Services, Dept. of Opticianry, Kahramanmaraş Sütçü İmam University, Kahramanmaraş, Turkey
[b] Vocational School of Health Services, Dept. of Medical, Imaging Techniques, Kahramanmaras Sütçü Imam Univ, Kahramanmaras, Turkey
[c] Department of Opticianry, Elbistan Vocational School of Health Services, Kahramanmaraş İstiklal University, Kahramanmaraş, 46300, Turkey
[d] Department of Material Science and Engineering, Graduate School of Natural and Applied Sciences, Kahramanmaraş Sütçü İmam University, Kahramanmaraş, Turkey

ARTICLE INFO

Keywords:
Radiation shielding
Zinc oxide nanoparticles
Glass

ABSTRACT

With the development of technology, the application areas of radiation have expanded and have an important place in our daily life. For this reason, we need more advanced and effective shielding materials to protect lives from the harmful effects of radiation. In this study, a simple combustion method was utilized to synthesize zinc oxide (ZnO) nanoparticles, and obtained nanoparticles' structural and morphological features were examined. The synthesized ZnO particles are used to produce different percentages (0, 2.5, 5, 7.5, 10%) of ZnO-doped glass samples. The structural and radiation shielding parameters of obtained glasses are examined. For this purpose, the Linear attenuation coefficient (LAC) has been measured via ^{65}Zn and ^{60}Co gamma sources and NaI(Tl) (ORTEC® 905–4) detector system has been used. Using the obtained LAC values, Mass Attenuation Coefficient (MAC), Half-Value Layer (HVL), Tenth-Value Layers (TVL), and Mean-Free Path (MFP) for glass samples have been calculated. According to these radiation shielding parameters, it was concluded that these ZnO doped glass samples provide effective results in radiation shielding and can be used as a shielding material effectively.

1. Introduction

Today, the use of devices emitting high-energy particles and radiation has increased considerably. Medical analysis, food sterilization, agricultural enterprises, and nuclear power plants are the most well-known areas where radioactive sources are used intensively. It is quite possible for personnel working in these areas to encounter serious health problems from exposure to X-rays or high-energy photons such as gamma rays (Alzahrani et al., 2021b; Kurtulus et al., 2021). Radiation exposure can cause genetic damage, damage to vascular cells, skin, and cancer (El-Mallawany et al., 2020a; Hannachi et al., 2023; Lakshminarayana et al., 2020). For this reason, it is crucial to develop materials for radiation shielding to protect against ionizing radiation (Arif et al., 2023; Issa et al., 2017a). For this purpose, many materials(Kavun et al., 2022) that can be used in radiation shielding have been developed and the most widely used one is Lead (Pb). However, lead is not preferred much today due to its harmful effects (Akman et al., 2023). Therefore, as an alternative to lead, radiation shielding materials such as concrete, alloy, rock, polymer and glass are being researched by scientists (Al-Buriahi et al., 2020; Saudi et al., 2021). Glass can be used as a radiation shield instead of traditional materials such as rocks, soil, blocks, concretes, compounds and polymers because the glasses have high corrosion resistance and are environmentally friendly (El-Mallawany et al., 2020b). In addition, glass has many advantages, such as high stability, high transmittance for visible light, low cost and easy synthesis (Rammah et al., 2020c, 2021). The composition of the glasses can be easily changed and used in many scientific and technological applications (Boukhris et al., 2020c). Radiation shielding properties can be improved by adding various compounds to the glasses (Alalawi, 2020). Oxide glasses attract the attention of researchers due to their many structural advantages (Boukhris et al., 2020b; El-Denglawey et al., 2021; Sayyed et al., 2018). The radiation shielding abilities of glass structures were investigated by doping with various metal oxides such as Li_2O (Al-Hadeethi and Sayyed, 2020a), MgO (Hanfi et al., 2021), ZnO (Khodadadi and Taherian, 2020), NiO (Boukhris et al., 2020a), Na_2O (Alzahrani et al., 2021a), GeO (Al-Hadeethi et al., 2020), WO_3 (Al-Buriahi et al., 2021), K_2O (Kilicoglu and Tekin, 2020), La_2O_3 (Issa et al., 2020), Nb_2O_5 (Liu et al., 2021), Gd_2O_3 (Al-Hadeethi and Sayyed, 2020b) and Sm_2O_3 (Abouhaswa et al., 2021).

ZnO has good thermal stability and increases the durability of glass

* Corresponding author. Vocational School of Health Services, Dept. of Opticianry, Kahramanmaraş Sütçü İmam University, Kahramanmaraş, Turkey.
E-mail addresses: heskalen@gmail.com, eskalen@ksu.edu.tr (H. Eskalen).

https://doi.org/10.1016/j.apradiso.2023.110858
Received 20 December 2022; Received in revised form 27 April 2023; Accepted 17 May 2023
Available online 18 May 2023

matrices (Kaky et al., 2020). Zinc oxide (ZnO) is known for lowering the melting temperature in producing oxide glasses. Glasses doped with ZnO in various proportions are of interest for radiation shielding research (Singh et al., 2014). For instance, Rammah et al. investigated the gamma radiation shielding effect of the increased ZnO doping in the TeO2–Li2O–ZnO glass matrix (Rammah et al., 2020b) Abd-Allah et al. Glasses were synthesized by a traditional melting method by increasing the ZnO ratio in the chemical composition of ZnO–BaO–PbO–B2O3. And they studied the radiation protection parameters theoretically and experimentally. These parameters show that the prepared glass samples exhibit better shielding properties than standard concrete (Abd-Allah et al., 2019). Zinc tellurium glasses were synthesized by Shams et al. by increasing the zinc oxide ratio in their chemical composition. Mass attenuation coefficient (MAC), half value layer (HVL) and mean free path (MFP) for glass samples have been measured. Experimental MAC was found to increase with increasing ZnO concentration. HVL and MFP decreased with increasing ZnO concentration (Issa et al., 2017b). Although work has been done to investigate radiation attenuation in many glass samples, there is a need to improve the radiation shielding properties of glasses. For this reason, glass samples were produced by increasing the zinc oxide ratio in its composition. Also, Radiation shielding parameters such as LAC, MAC, HVL, TVL and MFP values of produced glass samples were investigated.

2. Materials and method

2.1. Preparation of ZnO nanoparticles

The combustion method is preferred because it is fast, simple and economical for synthesizing zinc oxide nanoparticles. Urea was used as a fuel to synthesize nanostructured ZnO. 1 unit of urea was used for five units of zinc nitrate. Zinc nitrate and urea were carefully mixed mechanically. The mixture was transferred to a glass crucible. It was left in the oven at 500 °C for 4 h with the mixture in the crucible. Then the obtained ZnO was ground in a mortar.

2.2. Glasses fabrication

Glass samples were prepared using the melt-quenching method. The glass samples of $_{(55-x)}H_3BO_3$: $_x$ ZnO: $_{20}$ Na_2CO_3: $_{15}$ $BaCO_3$: $_{10}$ $NaBF_4$, where x = 0, 2.5, 5, 7.5 and 10 mol%, were prepared. First, the chemical reagents were thoroughly mixed. The chemicals were mixed in specific proportions, as shown in Table 1. Mechanically mixed powder mixtures were transferred to alumina crucibles. The chemical reagents in the alumina crucibles were put into the oven for 180 min and the temperature of the oven was adjusted to 1100 °C. During the melting of the samples, the melt was stirred frequently to avoid bubble formation. Then the melting mixtures were poured into steel molds, placed in another furnace at 300 °C, and annealed for 3 h. At the end of this period, it was left to cool on its own. All glass samples produced showed good transparency, and the synthesized glass samples are illustrated in Fig. 1.

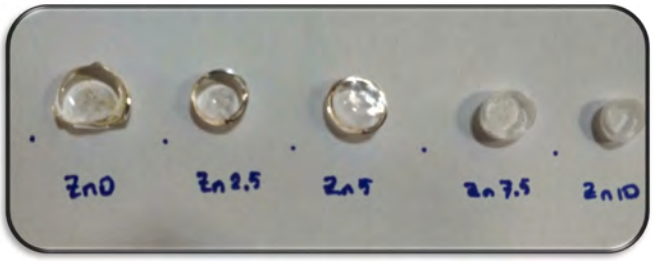

Fig. 1. Synthesized glass samples.

2.3. Characterization

Microstructure and size distribution of ZnO nanoparticles was investigated using high-resolution transmission electron microscopy (HR-TEM) with JEOL JEM 2100, UHR instrument. The structural properties of ZnO nanoparticles and glass samples were analyzed by X-ray diffraction (XRD). Philips X'Pert PRO XRD with Cu Kα radiation (λ = 0,154056 nm, tuned at 40 kV and 30 mA) was used to determine the XRD pattern. The optical properties of ZnO nanoparticles were recorded with a UV–Visible Spectrophotometer (Shimadzu UV 1800) at room temperature.

2.4. Radiation measurements

As shown in the experimental setup in Fig. 2, gamma radiation interacting with the material interacts with the material according to the Lambert-Beer law (Kavun, 2019; Kavun et al., 2019; Krane and Lynch, 1989; Singh et al., 2008). According to Eq. (2), gamma radiation interacting with the material is absorbed in the material to some extent.

$$\mu = \ln\left(\frac{I}{I_0}\right) \Big/ (-x)\left(\mathrm{cm}^{-1}\right) \tag{2}$$

In Eq. (2), μ is the linear attenuation coefficient in this equation, x is the material thickness, I is the number of gamma-rays reaching the detector after interacting with the material, and I_0 is the number of gamma-rays reaching the detector without interacting with the material.

The standard deviation of μ is calculated using equation (3) (Krane,

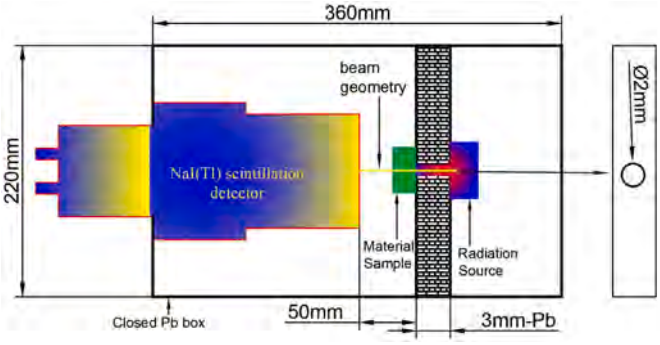

Fig. 2. Experimental Schema of radiation shielding measurements.

Table 1
Chemical composition of the glasses.

Glass code	Composition (mol%)					Thickness (mm)	Density (g/cm^3)
	ZnO	H_3BO_3	$NaCO_3$	$BaCO_3$	$NaBF_4$		
Zn0	0	55	20	15	10	5.66 ± 0.11	2.892
Zn2.5	2.5	52.5	20	15	10	5.71 ± 0.09	3.067
Zn5	5	50	20	15	10	5.58 ± 0.02	3.030
Zn7.5	7.5	47.5	20	15	10	5.47 ± 0.09	3.150
Zn10	10	45	20	15	10	5.76 ± 0.05	3.145

1991a).

$$\sigma = \sqrt{\frac{\sum_{i=1}^{N}(\mu_i - \overline{\mu})^2}{N-1}} \tag{3}$$

where μ_i represents each measurement and $\overline{\mu}$ is the average of the measurements. Also, the measurement number of every sample is represented by N (Krane, 1991b).

The mass attenuation coefficient of a material characterizes how easily it can be penetrated by a radiation beam and it has given by Eq. (4). (Kaewjang et al., 2015):

$$\mu_m = \frac{\mu}{\rho} = \sum w_i \left(\frac{\mu}{\rho}\right)_i \left(\mathrm{cm}^2/\mathrm{g}\right) \tag{4}$$

here, w_i is the weight fraction and ρ is density. The formulas that we can use to determine the required material thickness for halving the incident gamma radiation Half Value Layer (HVL) and for reducing it to one tenth (Tenth value layer-TVL) are given in Eqs. (5) and (6), respectively (Weibler, 1993) (Sayyed, 2016):

$$\textit{Half Value Layer}\ (HVL) = \frac{\ln 2}{\mu}(\mathrm{cm}) \tag{5}$$

$$\textit{Tenth Value Layer}\ (TVL) = \frac{\ln 10}{\mu}(\mathrm{cm}) \tag{6}$$

Mean Free Path (MFP) is the average distance the gamma-ray moves without interacting with the material, and it is given in Eq. (7) (Singh et al., 2014):

$$\textit{Mean Free Path}\ (MFP) = \frac{1}{\mu}(\mathrm{cm}) \tag{7}$$

The irradiation of materials has been performed with 1 mCi ^{65}Zn and ^{60}Co point radiation sources at 1165 keV, 1173 keV and 1333 keV gamma energies, respectively. NaI(Tl) detector systems have been used (ORTEC® 905–4) to detection of gamma-rays (Breur, 2013). As seen in Table 1, the thicknesses of the glasses are very close to each other. In this experimental setup, point radiation sources (1 mCi ^{65}Zn and ^{60}Co) and shielding material sample were placed on both sides of the Ø 2 mm window in the collimator opposite the detector and the measurement was made. The statistical error was calculated from ray-sum measurement and thickness measurement. Accordingly, the total standard error was determined by combining the errors made for the ray-sum and thickness measurements (Issa, 2016).

3. Results and discussion

Zinc oxide nanoparticles are obtained by a simple combustion method. This method is easy to handle and suitable for mass production. The crystalline properties of the obtained ZnO nanoparticles are investigated with X-ray diffraction methods, and the obtained results are given in Fig. 3. In this figure, the reddish lines that are intercepted with the x-axis represent the reference pattern and the intensities of the reddish lines are also proportional to the intensities in the reference pattern. The bluish lines are the X-ray diffraction patterns of the produced ZnO nanoparticles. As shown in the figure, the diffraction peaks of the synthesized ZnO and the reference diffraction pattern are quite compatible with each other. The obtained ZnO has a hexagonal structure and the peaks are compatible with ZnO shown with reference code PDF: 01-079-0207.

TEM image of synthesized ZnO nanoparticles is illustrated in Fig. 4. It is apparent from this image that synthesized particles are slightly agglomerated, and the morphological size of nanoparticles is close to each other. The particle size distribution of the obtained ZnO nanoparticles is given in Fig. 5. The average diameter of ZnO particles is

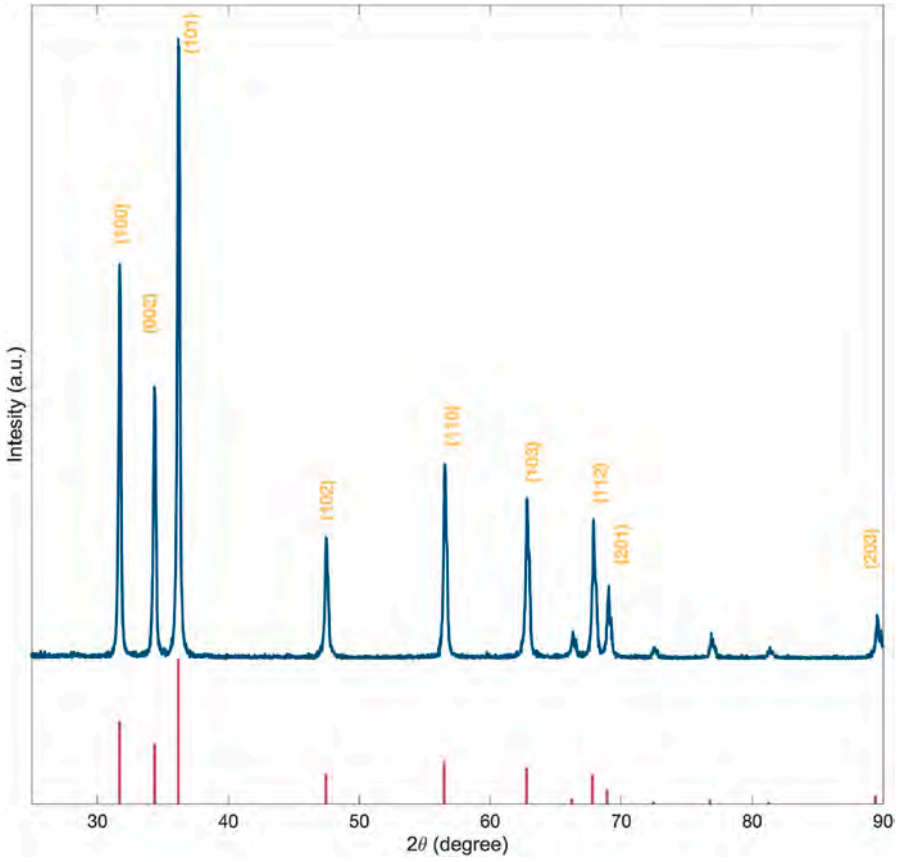

Fig. 3. XRD pattern of ZnO nanoparticles.

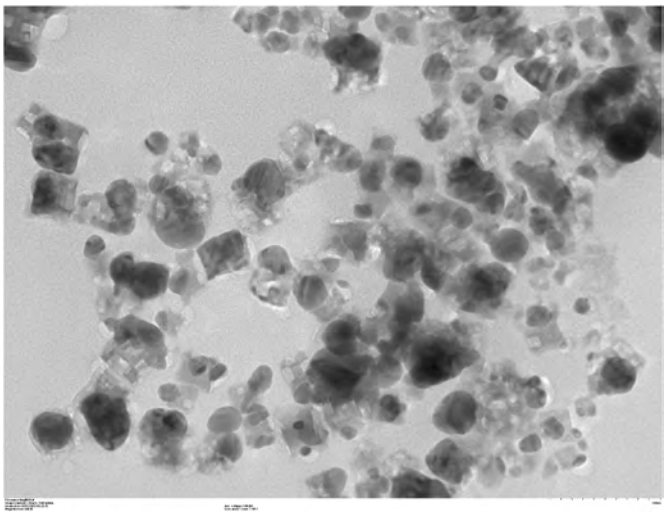

Fig. 4. TEM image of the ZnO nanoparticles.

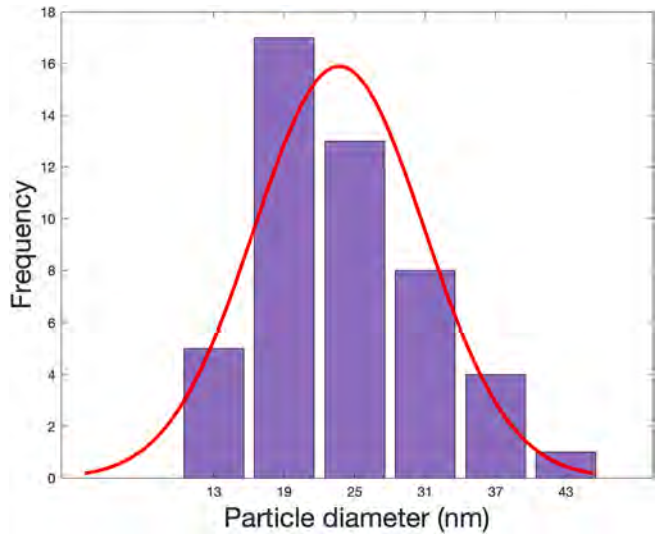

Fig. 5. Particle size distribution of the synthesized ZnO nanoparticles.

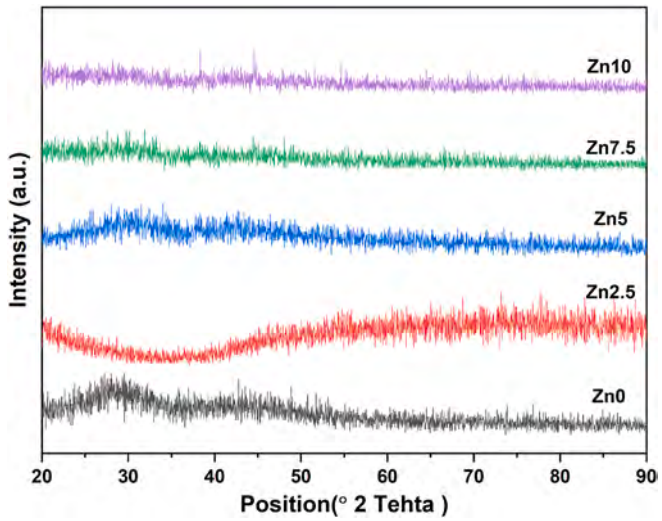

Fig. 6. XRD pattern of glasses.

calculated as 23.69 nm.

The X-ray diffraction pattern of the obtained glass samples is given in Fig. 6. ZnO nanoparticles do not affect the amorph nature of the synthesized glass sample. All samples have a lock of crystalline phase that indicates obtained samples are amorphous.

FTIR spectroscopy provides information about the interactions that can occur between the borate matrix and metal ions. Examination by FTIR spectroscopy helps us to get an idea of the ionic transport in the glass matrix. It is assumed that the vibrations of the various structures within the glass web are independent of each other (Elbashar et al., 2021). FTIR graphs of glass samples are shown in Fig. 7. It is thought that the bands around the 530 cm^{-1} and 730 cm^{-1} peaks are caused by ZnO_4 vibrations. These vibrations can be attributed to Zn–O/Zn–O–Zn vibrations (Rammah et al., 2020a, 2022). Bands saw around 875 cm^{-1} and 1035 cm^{-1} can be attributed to the B–O stretching vibrations of the BO_4 units (Bashar et al., 2019; Elbashar et al., 2021). The band observed around 1343 cm^{-1} can be attributed to the BO_3 unit at B–O stretching vibrations (Bashar et al., 2019; Pal Singh and Singh, 2011).

Fig. 8 shows the Linear Attenuation Coefficient (LAC) values. Here, according to the measurements performed at 1165 keV, while the Linear Attenuation Coefficient (LAC) values obtained in glasses containing 0% ZnO was 0.31161 ± 0.0533 cm^{-1}, this value increased to 1.02098 ± 0.1221 cm^{-1} until 10% ZnO contribution. It started from 0.29865 ± 00.0461 cm^{-1} at 1173 keV and increased to 0.90515 ± 0.1172 cm^{-1} in 10% ZnO doped glasses. Finally, it began from 0.23555 ± 0.0486 cm^{-1} at 1333 keV and reached a value of 0.67721 ± 0.0986 cm^{-1} for the same 10% ZnO ratio. Here, the R^2 values obtained according to the changing energy values were obtained as 0.992, 0.983 and 0.884 respectively. Compared with other shielding materials, LAC value was obtained as 0.0078 ± 0.001 cm^{-1} for 0% B-doped ZnO thin films, while it is 0.0106 ± 0.0003 cm^{-1} for 10% B-doped ZnO coated thin films (H. Eskalen et al., 2020).

However, the LAC value started from 0.0297 ± 0.0015 cm^{-1} in graphitic carbon nitride (gCN) samples containing 0% Thiourea at 1173 keV and increased to 1031 ± 0.0052 cm^{-1} until the Thiourea reached 100%. These LAC values increase from 0.0254 ± 0.0013 cm^{-1} to 0.1566 ± 0.0078 cm^{-1} at 1333 keV (Kavun et al., 2023). As another comparison example, LAC values changes from 0.80 ± 0.008 cm^{-1} to 0.86 ± 0.006 cm^{-1} at 1173 keV in Al–B–Mg alloy at 1173 keV (Yaykaşlı et al., 2022a).

Half-Value Layer (HVL) values obtained by using LAC values in equation (5) are shown in Fig. 9. According to the energy value of 1165 keV, the HVL value of the glass samples with 0% ZnO doped glass is

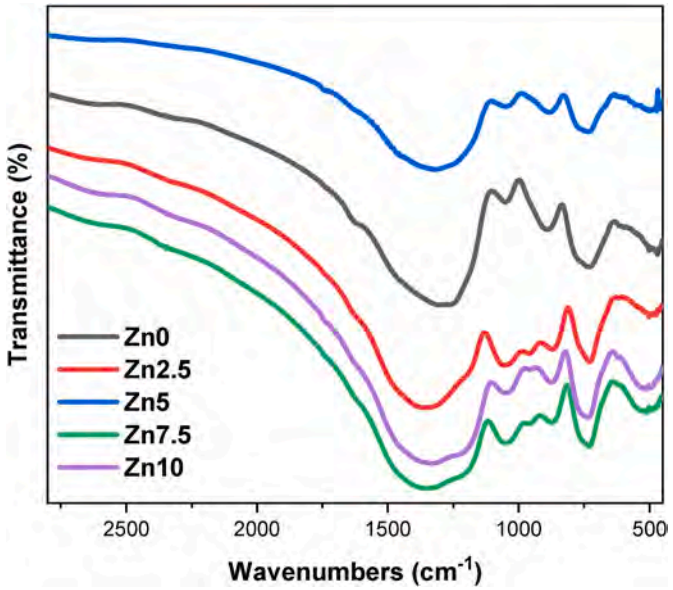

Fig. 7. FTIR spectra of glass samples.

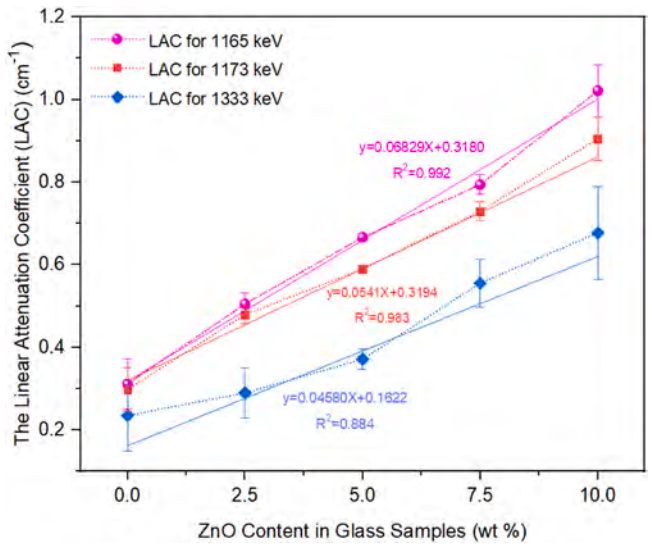

Fig. 8. Linear attenuation coefficient (LAC) values.

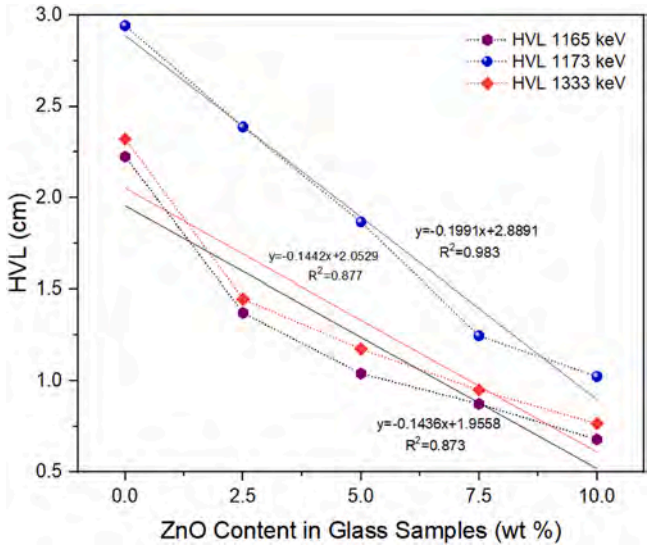

Fig. 9. Half Value Layer (HVL) values.

2.2244 cm and it decreases to 0.6789 cm at 10%. For 1173 keV gamma energy, 0% ZnO doped glass is 2.9426 cm and similarly 1.0235 cm at 10% ZnO doped glass. Lastly, to the 1333 keV energy, 0% ZnO doped glass is 2.3209 cm and 0.7657 cm at 10%. According to the obtained these HVL results, it can be seen that our ZnO-doped glass samples are much more effective for radiation shielding than different glass samples that are investigated by ALMisned et al. (2021). While the HVL value was found to be around 4–5 cm in studies conducted by ALMisned et al. (2021) in various energy ranges, it was seen that these values were obtained much better and lower in our study. To compare with the literature data, HVL value is 89.291 cm in 0% B-doped ZnO thin films and 65.601 cm in 10% B-doped ZnO thin films (Eskalen et al., 2020a). Also, this LAC value similarly decreased from 23.2917 in gCN samples containing 0% Thiourea at 1173 keV to 6.7208 until the Thiourea was 100%. The LAC values decreased from 27.2752 to 4.4253 at 1333 keV in gCN samples (Kavun et al., 2023). As another example, it changes from 0.86 to 0.80 at 1173 keV in the Al–B–Mg alloy (Kavun et al., 2023; Yaykaşlı et al., 2022a). This behavior can be explained as follows, because of the photoelectric process at low energy values, small density is required for glasses, and high density is required for medium energy ranges. In addition, when photons with high energy values enter the material, a significant amount of photons can penetrate the material (Ezzeldin et al., 2023; Madbouly et al., 2022a). Glasses were produced by adding ZnO at various rates in the prepared glass content. The amount of H_3BO_3 decreases with the increase of ZnO contribution in amorphous glasses. Thus, the density of the glass increases. As shown in Fig. 8, the LAC results improve as the ZnO concentration of the glass system increases. The reason for the positive effect in the obtained values is that the increase in the weight fraction and the presence of ZnO rises the effective atomic numbers as well as the densities. It could be the photoelectric effect that favors photons with low photon energy and attenuators with high atomic number (Madbouly et al., 2022b; Uosif et al., 2023).

Tenth-Value Layer (TVL) values have been calculated via equation (6) by using LAC values and results can be seen in Fig. 10. For the 1165 keV energy, the TVL value of 0% ZnO doped glass is 7.3893 cm, decreasing to 2.2552 cm at 10% ZnO ratio. At the 1173 keV energy, 0% ZnO doped glass is 7.7100 cm and the TVL value decreased to 2.5438 cm for 10% ZnO ratio. Lastly, to the 1333 keV energy, 0% ZnO doped glass is 9.7753 cm and 3.4001 cm at 10% ZnO. This TVL value is 89.291 cm in 0% B-doped ZnO thin films and 65.601 cm in 10% B ratio (Eskalen et al., 2020b). The TVL values changed between 77.37 cm and 22.32 cm in gCN samples according to the Thiourea ratio at 1173 keV (Kavun et al., 2023). Also, TVL values decreased from 2.87 to 2.66 cm for Al–B–Mg alloy at 1173 keV gamma energy (Yaykaşlı et al., 2022a).

The Mean Free Path (MFP) values express the path that the gammas emitted from the source take in the material by interacting with the material, and the MFP values calculated in this study are shown in Fig. 11. The MFP values were calculated using the LAC values in equation (7), the values obtained for 1165 keV started from 3.2091 cm and decreased up to 0.9794 cm with the increase of ZnO ratios in these glass samples. For 1173 keV energized gamma, MFP values are changed between 3.3484 cm and 1.1047 cm according to the 0%–10% ZnO ratio in glass samples. Also, to the 1333 keV energy, MFP values changed from 4.2453 cm to 1.4766 cm for 0% up to 10% ZnO doped glass samples. Here, to compare with B-doped ZnO coated thin films (Eskalen et al., 2020b), the MFP value is 128.82 cm for 0% B and this value drops to 94.64 cm at 10% B. The MFP value was obtained as 33.6028 cm when the Thiourea ratio was 0% at an energy of 1173 keV, and as 9.6961 cm when it was 100%. In the same way, 39.3497 cm and 6.3844 cm were obtained at 1333 keV energy (Kavun et al., 2023). The values measured in alloys vary between 1.25 cm and 1.15 cm for 1173 keV gamma energy (Yaykaşlı et al., 2022a).

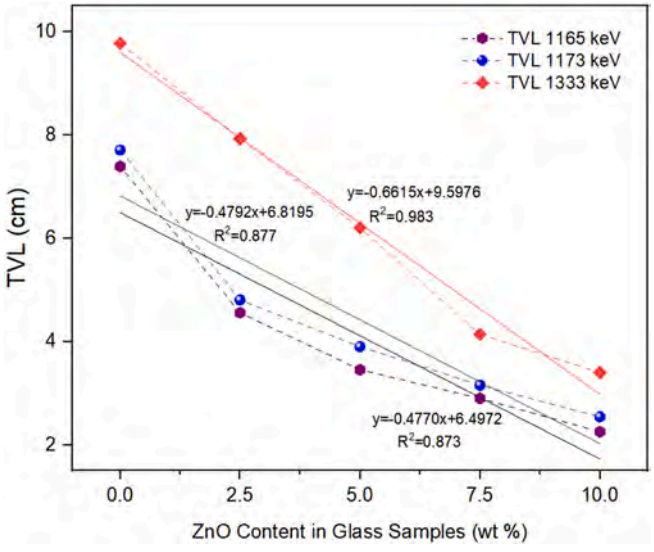

Fig. 10. Tenth value layer (TVL) values.

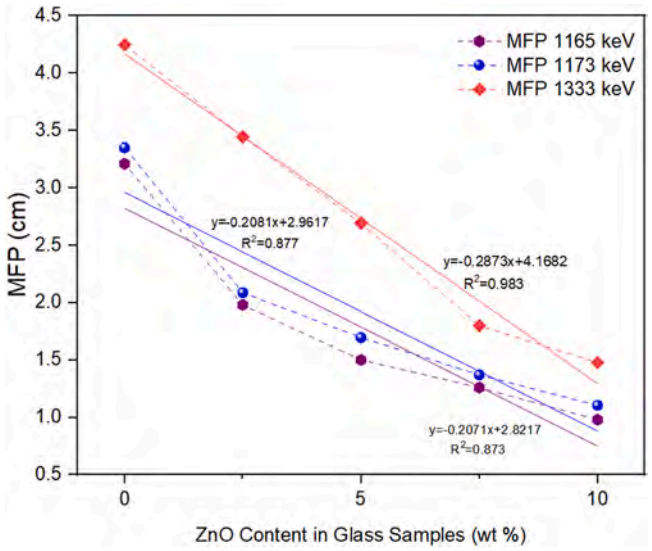

Fig. 11. Mean free path (MFP) values.

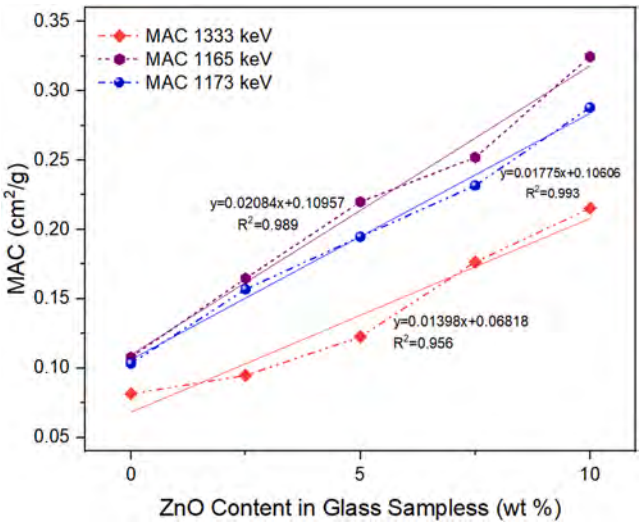

Fig. 12. Mass attenuation coefficient (MAC) values.

The mass attenuation coefficient (MAC) is seen in Fig. 12. The MAC values for 1165 keV energized gammas took for 0.1077 cm^2/g value for 0% ZnO doped glasses. These values increased up to 0.3246 cm^2/g for 10% ZnO doped glass samples. At 1173 keV energy, ZnO rate increased in glasses from 0% to 10%, and MAC values obtained from 0.1032 cm^2/g to 0.2878 cm^2/g, respectively. Finally, the MFP value for 1333 keV energy ranged from 0.0814 cm to 0.2153 cm. The obtained experimental MAC results have been compared with the bismuth borate glasses systems, which were the MAC values around 0.06 cm^2/g (Singh et al., 2002) but in this study, that is found between 0.1098 and 0.3490. Moreover, in theoretical and experimental study related to heavy metal-containing borate glasses, the MAC values were found to be around 0.06 cm^2/g (Sayyed et al., 2019); this also implies that our results are more acceptable than the mentioned literature. In the gCN study, at 1173 keV energy, the Thiourea ratio ranged from 0% to 100% and obtained values found 0.0203 ± 0.0192 cm^2/g and 0.1327 ± 0.0361 cm^2/g, respectively. At 1333 keV gamma energy, these MAC values are between 0.0173 ± 0.0308 cm^2/g and 0.1986 ± 0.0598 cm^2/g for same Thiourea ratio (Kavun et al., 2023). To compare with another alloy study in the literature, it varies between 0.3381 ± 0.0099 cm^2/g and 0.3656 ± 0.003 cm^2/g at 1173 keV energy (Yaykaşlı et al., 2022a).

4. Conclusion

In this study, ZnO nanoparticles are simple and one-pot synthesized by using the combustion method. The structural and morphological properties of obtained ZnO are examined with X-ray diffraction and TEM analysis, the obtained results show that ZnO nanoparticles are hexagonal in structure with an average diameter size of 23.69 nm.

Radiation shielding parameters of different percentages (0, 2.5, 5, 7.5, 10%) synthesized ZnO nanoparticles doped glasses were investigated for 1165 keV, 1173 keV and 1333 keV gamma energies.

The linear attenuation coefficient (LAC) at 1165 keV gamma energy was obtained between 0.31161 ± 0.0533 cm^{-1} and 1.02098 ± 0.1221 cm^{-1}. It was obtained between 0.29865 ± 0.0461 cm^{-1} and 0.90515 ± 0.1172 cm^{-1} for 1173 keV gamma energy. Finally, it was observed that these LAC values were obtained between 0.23555 ± 0.0486 cm^{-1} and 0.67721 ± 0.0986 cm^{-1} for 1333 keV, and it was increased with the ZnO ratio in the glasses at all energy values. These LAC values obtained were used to calculate other shielding parameters.

According to these results, HVL, TVL, MFP and MAC values gave effective results at all these energies. Here, measurements were made in 1165 keV, 1173 keV and 1333 keV different energies, and it was observed that 10% added to glass in all of them produced more effective results. As can be seen from all the results obtained, 10% ZnO added glasses give more effective results in radiation shielding. Thus, it has been demonstrated that ZnO doped glasses can be used effectively for radiation shielding.

CRediT authorship contribution statement

Hasan Eskalen: Writing – original draft, Supervision, Project administration, Conceptualization. **Yusuf Kavun:** Supervision, Project administration, Methodology, Investigation, Conceptualization. **Mustafa Kavgacı:** Writing – original draft, Visualization, Investigation, Formal analysis, Data curation.

Declaration of competing interest

The authors declare that they have no known competing financial interests or personal relationships that could have appeared to influence the work reported in this paper.

Hasan ESKALEN reports financial support was provided by Kahramanmaras Sutcu Imam University. Yusuf KAVUN reports financial support was provided by Kahramanmaras Sutcu Imam University.

Data availability

Data will be made available on request.

Acknowledgment

This study was supported by the Scientific Research Projects Coordination Unit of Kahramanmaraş Sütçü İmam University. Project numbers 2020/7–18 M, 2020/7–19 M, 2020/7–21 M and 2021/3–2 YLS. We gradefully thank Dr. Erdem Selver for the use of KSU, Textile Engineering, Composite Lab.

References

Abd-Allah, W.M., Saudi, H.A., Shaaban, K.S., Farroh, H.A., 2019. Investigation of structural and radiation shielding properties of 40B2O3–30PbO–(30-x) BaO-x ZnO glass system. Appl. Phys. Mater. Sci. Process 125. https://doi.org/10.1007/S00339-019-2574-0.

Abouhaswa, A.S., Sayyed, M.I., Altowyan, A.S., Al-Hadeethi, Y., Mahmoud, K.A., 2021. Synthesis, optical and radiation shielding capacity of the Sm2O3 doped borate glasses. J. Non-Cryst. Solids 553, 120505. https://doi.org/10.1016/J.JNONCRYSOL.2020.120505.

Akman, F., Kilicoglu, O., Agar, O., 2023. Feasibility of a novel shield of nuclear radiation with W–Ni–Fe–Co and La–Bi alloys alternative to Pb and ordinary concrete absorbers. Prog. Nucl. Energy 156, 104537. https://doi.org/10.1016/J.PNUCENE.2022.104537.

Alalawi, A., 2020. Experimental and Monte Carlo investigations on the optical properties and nuclear shielding capability of Bi2O3Na2O-B2O3Cu2O glasses. J. Non-Cryst. Solids 548, 120321. https://doi.org/10.1016/J.JNONCRYSOL.2020.120321.

Al-Buriahi, M.S., Bakhsh, E.M., Tonguc, B., Khan, S.B., 2020. Mechanical and radiation shielding properties of tellurite glasses doped with ZnO and NiO. Ceram. Int. 46, 19078–19083. https://doi.org/10.1016/J.CERAMINT.2020.04.240.

Al-Buriahi, M.S., Taha, T.A., Alothman, M.A., Donya, H., Olarinoye, I.O., 2021. Influence of WO3 incorporation on synthesis, optical, elastic and radiation shielding properties of borosilicate glass system. The European Physical Journal Plus 7 (136), 1–23. https://doi.org/10.1140/EPJP/S13360-021-01790-5, 2021 136.

Al-Hadeethi, Y., Sayyed, M.I., 2020a. BaO–Li2O–B2O3 glass systems: potential utilization in gamma radiation protection. Prog. Nucl. Energy 129, 103511. https://doi.org/10.1016/J.PNUCENE.2020.103511.

Al-Hadeethi, Y., Sayyed, M.I., 2020b. Effect of Gd2O3 on the radiation shielding characteristics of Sb2O3–PbO–B2O3–Gd2O3 glass system. Ceram. Int. 46, 13768–13773. https://doi.org/10.1016/J.CERAMINT.2020.02.166.

Al-Hadeethi, Y., Sayyed, M.I., Rammah, Y.S., 2020. Fabrication, optical, structural and gamma radiation shielding characterizations of GeO2-PbO-Al2O3–CaO glasses. Ceram. Int. 46, 2055–2062. https://doi.org/10.1016/J.CERAMINT.2019.09.185.

Almisned, G., Elshami, W., Issa, S.A.M., Susoy, G., Zakaly, H.M.H., Algethami, M., Rammah, Y.S., Ene, A., Al-Ghamdi, S.A., Ibraheem, A.A., Tekin, H.O., 2021. Enhancement of gamma-ray shielding properties in cobalt-doped heavy metal borate glasses: the role of lanthanum oxide reinforcement. Materials. https://doi.org/10.3390/ma14247703.

Alzahrani, J.S., Alothman, M.A., Eke, C., Al-Ghamdi, H., Aloraini, D.A., Al-Buriahi, M.S., 2021a. Simulating the radiation shielding properties of TeO2–Na2O–TiO glass system using PHITS Monte Carlo code. Comput. Mater. Sci. 196, 110566 https://doi.org/10.1016/J.COMMATSCI.2021.110566.

Alzahrani, J.S., Kavas, T., Kurtulus, R., Olarinoye, I.O., Al-Buriahi, M.S., 2021b. Physical, structural, mechanical, and radiation shielding properties of the PbO–B2O3–Bi2O3–ZnO glass system. J. Mater. Sci. Mater. Electron. 32, 18994–19009. https://doi.org/10.1007/S10854-021-06414-3/FIGURES/15.

Arif, F.T., Heryanto, H., Sulieman, A., Bradley, D.A., Tahir, D., 2023. Geopolymer cellulose-based composite Black Carbon (BC)/Fe/Cu/polyvinyl alcohol for eco-friendly apron X-ray. Radiat. Phys. Chem. 207, 110843 https://doi.org/10.1016/J.RADPHYSCHEM.2023.110843.

Bashar, K.A., Lakshminarayana, G., Baki, S.O., Mohammed, A.B.F.A., Caldiño, U., Meza-Rocha, A.N., Singh, V., Kityk, I.V., Mahdi, M.A., 2019. Tunable white-light emission from Pr3+/Dy3+ co-doped B2O3 - TeO2 PbO - ZnO Li2O - Na2O glasses. Opt. Mater. 88, 558–569. https://doi.org/10.1016/J.OPTMAT.2018.12.028.

Boukhris, I., Alalawi, A., Al-Buriahi, M.S., Kebaili, I., Sayyed, M.I., 2020a. Radiation attenuation properties of bioactive glasses doped with NiO. Ceram. Int. 46, 19880–19889. https://doi.org/10.1016/J.CERAMINT.2020.05.047.

Boukhris, I., Kebaili, I., Al-Buriahi, M.S., Sriwunkum, C., Sayyed, M.I., 2020b. Effect of lead oxide on the optical properties and radiation shielding efficiency of antimony-sodium-tungsten glasses. Appl. Phys. Mater. Sci. Process 126, 1–10. https://doi.org/10.1007/S00339-020-03932-5/FIGURES/12.

Boukhris, I., Kebaili, I., Al-Buriahi, M.S., Tonguc, B., AlShammari, M.M., Sayyed, M.I., 2020c. Effect of bismuth oxide on the optical features and gamma shielding efficiency of lithium zinc borate glasses. Ceram. Int. 46, 22883–22888. https://doi.org/10.1016/J.CERAMINT.2020.06.061.

Breur, S., 2013. The Performance of NaI(Tl) Scintillation Detectors. University of Amsterdam, Master Thesis.

Elbashar, Y.H., ElGabaly, S.G., Rayan, D.A., 2021. FTIR and NIR spectroscopic analyses of Co3O4-doped sodium zinc borate glass matrix. J. Opt. 50, 559–568. https://doi.org/10.1007/S12596-021-00724-9.

El-Denglawey, A., Zakaly, H.M.H., Alshammari, K., Issa, S.A.M., Tekin, H.O., AbuShanab, W.S., Saddeek, Y.B., 2021. Prediction of mechanical and radiation parameters of glasses with high Bi2O3 concentration. Results Phys. 21, 103839 https://doi.org/10.1016/J.RINP.2021.103839.

El-Mallawany, R., El-Agawany, F.I., Al-Buriahi, M.S., Muthuwong, C., Novatski, A., Rammah, Y.S., 2020a. Optical properties and nuclear radiation shielding capacity of TeO2-Li2O-ZnO glasses. Opt. Mater. 106, 109988 https://doi.org/10.1016/J.OPTMAT.2020.109988.

El-Mallawany, R., El-Agawany, F.I., Al-Buriahi, M.S., Muthuwong, C., Novatski, A., Rammah, Y.S., 2020b. Optical properties and nuclear radiation shielding capacity of TeO2-Li2O-ZnO glasses. Opt. Mater. 106, 109988 https://doi.org/10.1016/J.OPTMAT.2020.109988.

Eskalen, H., Kavun, Y., Kerli, S., Eken, S., 2020a. An investigation of radiation shielding properties of boron doped ZnO thin films. Opt. Mater. 105, 109871 https://doi.org/10.1016/j.optmat.2020.109871.

Eskalen, H., Kavun, Y., Kerli, S., Eken, S., 2020b. An investigation of radiation shielding properties of boron doped ZnO thin films. Opt. Mater. 105, 109871 https://doi.org/10.1016/J.OPTMAT.2020.109871.

Ezzeldin, M., Al-Harbi, L.M., Sadeq, M.S., Mahmoud, A.E. razek, Muhammad, M.A., Ahmed, H.A., 2023. Impact of CdO on optical, structural, elastic, and radiation shielding parameters of CdO–PbO–ZnO–B2O3–SiO2 glasses. Ceram. Int. 49, 19160–19173. https://doi.org/10.1016/J.CERAMINT.2023.03.042.

Eskalen, H., Kavun, Y., Kerli, S., Eken, S., 2020. An investigation of radiation shielding properties of boron doped ZnO thin films. Opt. Mater. 105 https://doi.org/10.1016/j.optmat.2020.109871.

Hanfi, M.Y., Sayyed, M.I., Lacomme, E., Akkurt, I., Mahmoud, K.A., 2021. The influence of MgO on the radiation protection and mechanical properties of tellurite glasses. Nucl. Eng. Technol. 53, 2000–2010. https://doi.org/10.1016/J.NET.2020.12.012.

Hannachi, E., Sayyed, M.I., Slimani, Y., Elsafi, M., 2023. Structural, optical and radiation shielding peculiarities of strontium titanate ceramics mixed with tungsten nanowires: an experimental study. Opt. Mater. 135, 113317 https://doi.org/10.1016/J.OPTMAT.2022.113317.

Issa, S.A.M., 2016. Effective atomic number and mass attenuation coefficient of PbO–BaO–B2O3 glass system. Radiat. Phys. Chem. 120, 33–37. https://doi.org/10.1016/J.RADPHYSCHEM.2015.11.025.

Issa, S.A.M., Ali, A.M., Tekin, H.O., Saddeek, Y.B., Al-Hajry, A., Algarni, H., Susoy, G., 2020. Enhancement of nuclear radiation shielding and mechanical properties of YBiBO3 glasses using La2O3. Nucl. Eng. Technol. 52, 1297–1303. https://doi.org/10.1016/J.NET.2019.11.017.

Issa, S.A.M., Sayyed, M.I., Kurudirek, M., 2017a. Study of gamma radiation shielding properties of ZnO−TeO2 glasses. Bull. Mater. Sci. 40, 841–857. https://doi.org/10.1007/S12034-017-1425-X/FIGURES/9.

Issa, S.A.M., Sayyed, M.I., Kurudirek, M., 2017b. Study of gamma radiation shielding properties of ZnO−TeO2 glasses. Bull. Mater. Sci. 40, 841–857. https://doi.org/10.1007/S12034-017-1425-X/FIGURES/9.

Kaewjang, S., Maghanemi, U., Kothan, S., Kim, H.J., Limkitjaroenporn, P., Kaewkhao, J., 2015. New gadolinium based glasses for gamma-rays shielding materials. Nucl. Eng. Des. 280, 21–26. https://doi.org/10.1016/j.nucengdes.2014.08.030.

Kaky, K.M., Sayyed, M.I., Ati, A.A., Mhareb, M.H.A., Mahmoud, K.A., Baki, S.O., Mahdi, M.A., 2020. Germanate oxide impacts on the optical and gamma radiation shielding properties of TeO2-ZnO-Li2O glass system. J. Non-Cryst. Solids 546, 120272. https://doi.org/10.1016/J.JNONCRYSOL.2020.120272.

Kavun, Y., 2019. Pb(NO3)2 Katkılı Duvar Kâğıtlarının radyasyon Soğurma Özelliklerinin İncelenmesi. Bitlis Eren Üniversitesi Fen Bilimleri Dergisi 8, 1–6. https://doi.org/10.17798/bitlisfen.630618.

Kavun, Y., Eskalen, H., Kavgacı, M., 2023. A study on gamma radiation shielding performance and characterization of graphitic carbon nitride. Chem. Phys. Lett. 811, 140246 https://doi.org/10.1016/J.CPLETT.2022.140246.

Kavun, Y., Kerli, S., Eskalen, H., Kavgacı, M., 2022. Characterization and nuclear shielding performance of Sm doped In_2O_3 thin films. Radiat. Phys. Chem. 194, 110014 https://doi.org/10.1016/J.RADPHYSCHEM.2022.110014.

Kavun, Y., Tutus, A., Uruş, S., Tutuş, A., Eken, S., Özbek, R., 2019. Investigation of radiation absorption properties of tungstate and molibdate doped wallpapers. Cumhuriyet Science Journal CSJ e 40, 846–853. https://doi.org/10.17776/csj.600967.

Khodadadi, A., Taherian, R., 2020. Investigation on the radiation shielding properties of lead silicate glasses modified by ZnO and BaO. Mater. Chem. Phys. 251, 123136 https://doi.org/10.1016/J.MATCHEMPHYS.2020.123136.

Kilicoglu, O., Tekin, H.O., 2020. Bioactive glasses and direct effect of increased K2O additive for nuclear shielding performance: a comparative investigation. Ceram. Int. 46, 1323–1333. https://doi.org/10.1016/J.CERAMINT.2019.09.095.

Krane, K.S., 1991a. Introductory Nuclear Physics. John Wiley & Sons.

Krane, K.S., 1991b. Introductory Nuclear Physics. John Wiley & Sons.

Krane, K.S., Lynch, W.G., 1989. Introductory nuclear physics. Phys. Today. https://doi.org/10.1063/1.2810884.

Kurtulus, R., Kavas, T., Mahmoud, K.A., Akkurt, I., Gunoglu, K., Sayyed, M.I., 2021. The effect of Nb2O5 on waste soda-lime glass in gamma-rays shielding applications. J. Mater. Sci. Mater. Electron. 32, 4903–4915. https://doi.org/10.1007/S10854-020-05230-5/FIGURES/10.

Lakshminarayana, G., Elmahroug, Y., Kumar, A., Rekik, N., Lee, D.E., Yoon, J., Park, T., 2020. Reckoning of nuclear radiation attenuation capabilities for binary GeO2-Tl2O, GeO2-Bi2O3, and ternary GeO2-Tl2O–Bi2O3 glasses utilizing pertinent theoretical and computational approaches. Opt. Mater. 108, 110113 https://doi.org/10.1016/J.OPTMAT.2020.110113.

Liu, G., Chen, X., Liu, H., Wang, Y., Sun, M., Yan, N., Qian, Q., Yang, Z., 2021. The radiation resistance property of doping Nb2O5 into barium gallo-germanate glass. Chin. Phys. B. https://doi.org/10.1088/1674-1056/AC2B1A.

Madbouly, A.M., Sallam, O.I., Issa, S.A.M., Rashad, M., Hamdy, A., Tekin, H.O., Zakaly, H.M.H., 2022a. Experimental and FLUKA evaluation on structure and optical properties and γ-radiation shielding capacity of bismuth borophosphate glasses. Prog. Nucl. Energy 148, 104219. https://doi.org/10.1016/J.PNUCENE.2022.104219.

Madbouly, A.M., Sallam, O.I., Issa, S.A.M., Rashad, M., Hamdy, A., Tekin, H.O., Zakaly, H.M.H., 2022b. Experimental and FLUKA evaluation on structure and optical properties and γ-radiation shielding capacity of bismuth borophosphate glasses. Prog. Nucl. Energy 148, 104219. https://doi.org/10.1016/J.PNUCENE.2022.104219.

Pal Singh, G., Singh, D.P., 2011. Spectroscopic study of ZnO doped CeO2–PbO–B2O3 glasses. Phys. B Condens. Matter 406, 3402–3405. https://doi.org/10.1016/J.PHYSB.2011.06.007.

Rammah, Y.S., Alsaif, N.A.M., Khattari, Z.Y., Shams, M.S., Elsad, R.A., Sadeq, M.S., 2022. Synthesis, physical, FTIR, and optical characteristics of B2O3·CaO·ZnO glasses doped with Nb2O5 oxide: experimental investigation. J. Mater. Sci. Mater. Electron. 33, 23749–23760. https://doi.org/10.1007/S10854-022-09133-5.

Rammah, Y.S., El-Agawany, F.I., Mahmoud, K.A., El-Mallawany, R., Ilik, E., Kilic, G., 2020a. FTIR, UV–Vis–NIR spectroscopy, and gamma rays shielding competence of novel ZnO-doped vanadium borophosphate glasses. J. Mater. Sci. Mater. Electron. 31, 9099–9113. https://doi.org/10.1007/S10854-020-03440-5.

Rammah, Y.S., El-Agwany, F.I., Mahmoud, K.A., Novatski, A., El-Mallawany, R., 2020b. Role of ZnO on TeO2.Li2O.ZnO glasses for optical and nuclear radiation shielding

applications utilizing MCNP5 simulations and WINXCOM program. J. Non-Cryst. Solids 544, 120162. https://doi.org/10.1016/J.JNONCRYSOL.2020.120162.
Rammah, Y.S., Mahmoud, K.A., Sayyed, M.I., El-Agawany, F.I., El-Mallawany, R., 2020c. Novel vanadyl lead-phosphate glasses: P2O5–PbO–ZnONa2O–V2O5: synthesis, optical, physical and gamma photon attenuation properties. J. Non-Cryst. Solids 534, 119944. https://doi.org/10.1016/J.JNONCRYSOL.2020.119944.
Rammah, Y.S., Tekin, H.O., Issa, S.A.M., El-Agawany, F.I., Mahmoud, K.A., Abdel-Hafez, S.H., Abouhaswa, A.S., 2021. On B2O3/Bi2O3/Na2O/Gd2O3 glasses: synthesis, structure, physical characteristics, and gamma-ray attenuation competence. Appl. Phys. Mater. Sci. Process 127, 1–16. https://doi.org/10.1007/S00339-021-04995-8/FIGURES/23.
Saudi, H.A., Issa, S.A.M., Elazaka, A.I., Zakaly, H.M.H., Kilic, G., Tekin, H.O., 2021. Exploration of material characteristics of tantalum borosilicate glasses by experimental, simulation, and theoretical methods. J. Phys. Chem. Solid. 159, 110282 https://doi.org/10.1016/J.JPCS.2021.110282.
Sayyed, M.I., 2016. Bismuth modified shielding properties of zinc boro-tellurite glasses. J. Alloys Compd. 688, 111–117. https://doi.org/10.1016/j.jallcom.2016.07.153.
Sayyed, M.I., Kaky, K.M., Gaikwad, D.K., Agar, O., Gawai, U.P., Baki, S.O., 2019. Physical, structural, optical and gamma radiation shielding properties of borate glasses containing heavy metals (Bi2O3/MoO3). J. Non-Cryst. Solids 507, 30–37. https://doi.org/10.1016/j.jnoncrysol.2018.12.010.
Sayyed, M.I., Rammah, Y.S., Abouhaswa, A.S., Tekin, H.O., Elbashir, B.O., 2018. ZnO-B2O3-PbO glasses: synthesis and radiation shielding characterization. Phys. B Condens. Matter 548, 20–26. https://doi.org/10.1016/J.PHYSB.2018.08.024.
Singh, K., Singh, H., Sharma, V., Nathuram, R., Khanna, A., Kumar, R., Singh Bhatti, S., Singh Sahota, H., 2002. Gamma-ray attenuation coefficients in bismuth borate glasses. Nucl. Instrum. Methods Phys. Res. B 194, 1–6. https://doi.org/10.1016/S0168-583X(02)00498-6.
Singh, S., Kumar, A., Singh, D., Thind, K.S., Mudahar, G.S., 2008. Barium–borate–flyash glasses: as radiation shielding materials. Nucl. Instrum. Methods Phys. Res. B 266, 140–146. https://doi.org/10.1016/j.nimb.2007.10.018.
Singh, V.P., Badiger, N.M., Kaewkhao, J., 2014. Radiation shielding competence of silicate and borate heavy metal oxide glasses: comparative study. J. Non-Cryst. Solids 404, 167–173. https://doi.org/10.1016/J.JNONCRYSOL.2014.08.003.
Uosif, M.A.M., Issa, S.A.M., Ene, A., Mostafa, A.M.A., Atta, A., Agammy, E.F. El, Zakaly, H.M.H., 2023. Lead-free ternary glass for radiation protection: composition and performance evaluation for Solar cell coverage, 2023 Materials 16, 3036. https://doi.org/10.3390/MA16083036, 16, 3036.
Weibler, J., 1993. Properties of Metals Used for RF Shielding. EMC Test & Design.
Yaykaşlı, H., Eskalen, H., Kavun, Y., Gögebakan, M., 2022. Microstructural, thermal, and radiation shielding properties of Al50B25Mg25 alloy prepared by mechanical alloying. J. Mater. Sci. Mater. Electron. 33, 2350–2359. https://doi.org/10.1007/s10854-021-07434-9.

Chemical Physics Letters 811 (2023) 140246

Contents lists available at ScienceDirect

Chemical Physics Letters

journal homepage: www.elsevier.com/locate/cplett

A study on gamma radiation shielding performance and characterization of graphitic carbon nitride

Yusuf Kavun [a,d,*], Hasan Eskalen [b,d], Mustafa Kavgacı [c,d]

[a] Vocational School of Health Services, Dept. of Medical Imaging Techniques, Kahramanmaras Sütçü Imam University, Kahramanmaras, Turkey
[b] Vocational School of Health Services, Dept. of Opticianry, Kahramanmaraş Sütçü İmam University, Kahramanmaraş, Turkey
[c] Department of Opticianry, Elbistan Vocational School of Health Services, Kahramanmaraş İstiklal University, Kahramanmaraş 46300, Turkey
[d] Material Science and Engineering, Institute of Science, Kahramanmaraş Sütçü İmam University, Kahramanmaraş 46 050, Turkey

ARTICLE INFO

Keywords:
Radiation shielding
gCN
Gama shielding

ABSTRACT

Graphitic Carbon Nitride (gCN) can be used in many fields such as sensing, solar energy and device construction. In this study, gCN obtained from urea and thiourea precursors were produced to determine the radiation shielding properties. The structural features and optical properties of these produced samples were investigated. Also, the radiation shielding properties were determined experimentally. Here, Linear Attenuation Coefficient values were determined experimentally and Mass Attenuation Coefficient, Half-Value Layer, Tenth-Value Layer and Mean Free Path values were calculated employing this value. According to obtained results, it is seen that obtained gCN can be used effectively in radiation shielding.

1. Introduction:

Today, in parallel with the process in technology, the applications that use radiation sources have been enormously increased [1]. For example, two common types of an ionizing radiation sources, gamma and X-rays, have been used in nuclear power plants, radiological imaging, nuclear medicine, agriculture, research centers and industry [2]. Although radiation provides advantages to people in many different areas, especially in healthcare, it is known that it has a negative effect on human and living health depending on the exposure time [3]. Traditionally, lead and materials that contain lead element are commonly used for radiation protection since lead provide extraordinary shielding capability, but lead is toxic material [4].Therefore, today functional materials for radiation shielding are more important than ever before. Scientists are making extraordinary efforts to produce materials with good radiation shielding properties. Some of these materials are alloys, glasses, thin films and polymer composites [5-10].

Another method for achieving new shielding materials other than changing material types the composition of materials could be changed. In literature, the specific materials shieling capability enhanced with introducing of nanoparticles [11]. Recent studies reveal that, radiation shielding performance of materials that contain Bi_2O_3 nanoparticles is better than bulk Bi_2O_3 [12]. Another study show that nano-structured ZnO nanoparticles enhanced shielding performance of ball clay and the use of nanoparticle is more promising than micro ZnO [13]. The micron and nanosized PbO are tested and the result shows that the radiation shielding performance of nanosized PbO is better than the micron sized PbO [14].

Graphitic carbon nitride (gCN) is 2D material and known as a polymeric semiconductor with unexpected thermal and chemical stability[15]. It has unique applications in electronics, biomedicine, sensors and CO_2 separation and utilization [16] because of non-toxic nature, biocompatible, low cost, high area, easy to obtain and feasibility in surface engineering [17,18]. The gCN is a mainly lightweight, non-toxic and inexpensive semiconductor material. This type of materials can convert high energetic particles or photon into electronic signal; thusthey have potential use in dosimetry and X-ray detection. It is critical to evaluate, the attenuation coefficients of semiconductor materials used in computing photon penetration in shielding materials [19-21]. In this experimental work, gCN have been synthesized by simple combustion methods by using two different precursors. Structural, morphological and thermal properties of it characterized. The precursor dependent radiation shielding performance of the obtained gCN was studied.

The use of gCN as photocatalysts has increased recently. It has been obtained as a result of the search for metal-free materials that can absorb

* Corresponding author at: Vocational School of Health Services, Dept. of Medical Imaging Techniques, Kahramanmaras Sütçü Imam University, Kahramanmaras, Turkey.
E-mail address: yusufkavun@gmail.com (Y. Kavun).

https://doi.org/10.1016/j.cplett.2022.140246
Received 9 August 2022; Received in revised form 30 November 2022; Accepted 3 December 2022
Available online 9 December 2022

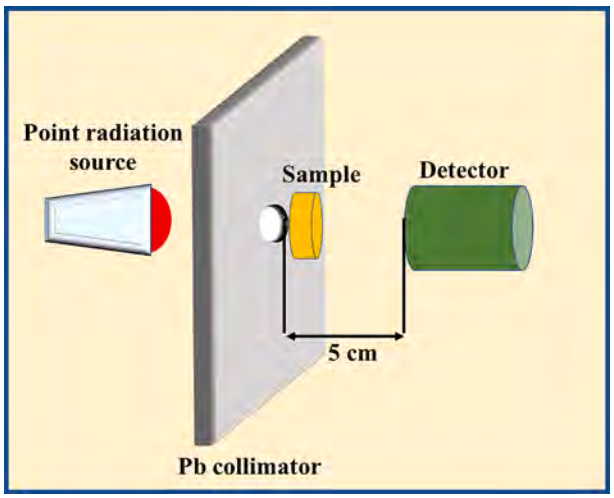

Fig. 1. Experimental Schema of radiation shielding measurements [25].

efficiently within the solar spectrum and use solar energy at the maximum level. Most of the solar spectrum (46%) falls into visible light, while only 5% falls in the ultraviolet region. A large number of gCN-based nanocomposites have been developed as photocatalysts. It is considered suitable for low energy activation (2.7 eV) with seven different phases. Its relatively low bandgap allows it to absorb light. This low band gap of gCN could be as a result of nitrogen and sp2- hybridized carbon, which resulted in the electronic structures that contain π-conjugated systems [22].

In this study, the gCN samples of Urea $_{(100-x)}$.Thiourea$_{(x)}$, where x = 0, 25, 50, 75, and 100 samples, were prepared to investigate radiation shielding and optical properties characterization. For this reason, Linear Attenuation Coefficients (LAC) (μ) of these samples have been obtained using an experimental measurement system. To reveal gamma shielding properties, Half-Value Layer (HVL), Tenth-Value Layer (TVL), Mean Free Path (MFP) and Mass attenuation Coefficients (MAC) have been calculated via μ value. In addition, XRD, SEM, FTIR and BET adsorption analyzes of these samples were also carried out.

2. Materials and method

2.1. Preparation of gCN

The gCN (graphitic carbon nitride) samples were synthesized from Urea and Thiourea by a thermal decomposition method. Urea and Thiourea were bought in high purity from Tekkim chemistry and Merck. The gCN samples of Urea $_{(100-x)}$ - Thiourea $_x$, where x = 0, 25, 50, 75 and 100 were prepared. Typically, samples (30 g) were placed in a covered ceramic crucible. The crucible was then placed in an oven and heated to 550 °C at a heating rate of 3 °C per minute under atmospheric pressure in the presence of air. It was kept at 550 °C for 4 h. After heating, the crucible was allowed to cool to room temperature in the furnace. Samples synthesized from urea and thiourea were labelled as U_{100}, $U_{75}T_{25}$, $U_{50}T_{50}$, $U_{25}T_{75}$ and T_{100}, respectively.

2.2. Characterization

SEM micrograph for all synthesized gCN samples were examined by SEM JOEL microscope at the Eastern Anatolian High Technology Research Center of Atatürk University (DAYTAM, Erzurum, Turkey).

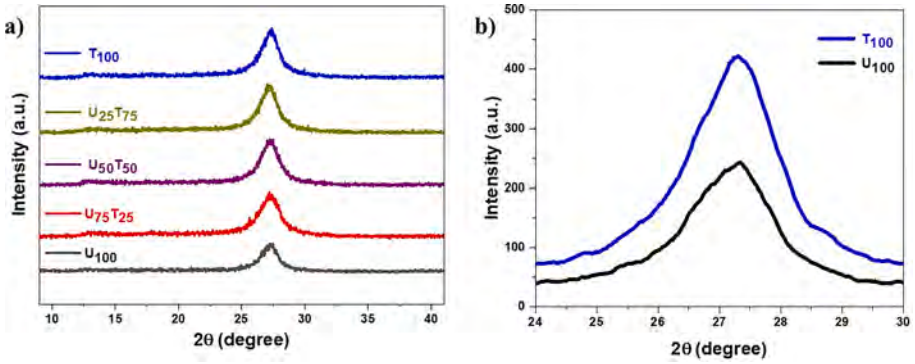

Fig. 2. XRD pattern of gCN nanoparticles (a) with increasing thiourea concentration, (b) comparison of precursor urea and thiourea.

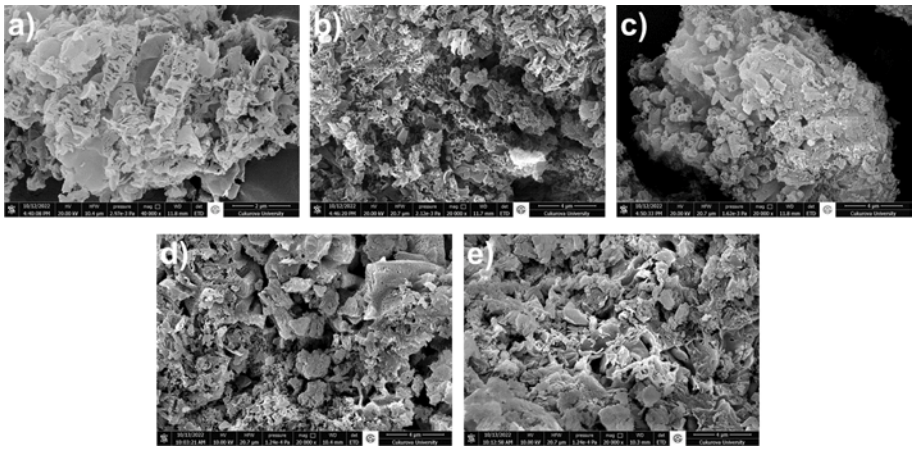

Fig. 3. SEM image of the gCN nanoparticles (a) U_{100} (b) $U_{75}T_{25}$ (c) $U_{50}T_{50}$ (d) $U_{25}T_{75}$ (e) T_{100}.

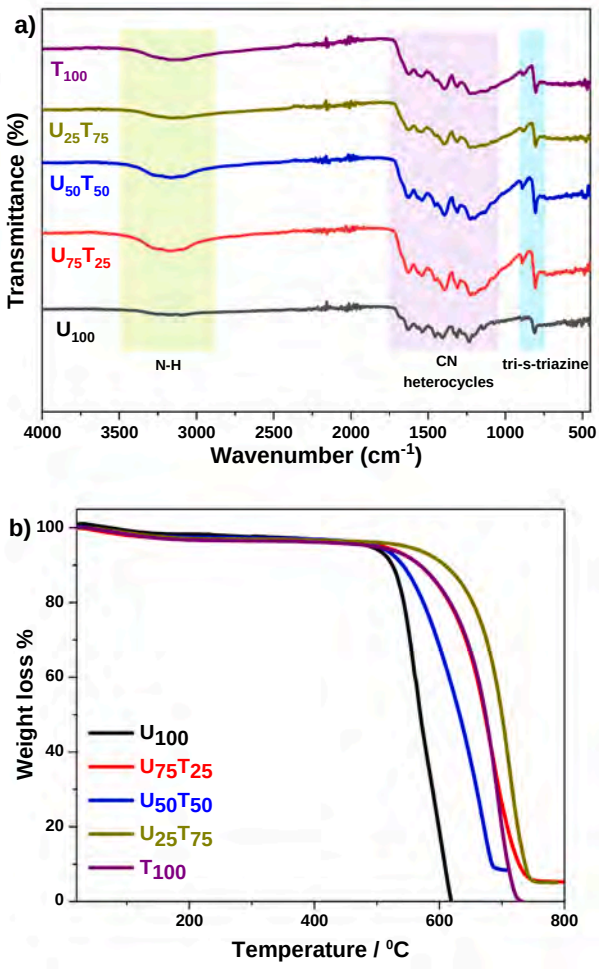

Fig. 4. (a) FTIR pattern (b) TGA pattern of the gCN nanoparticles.

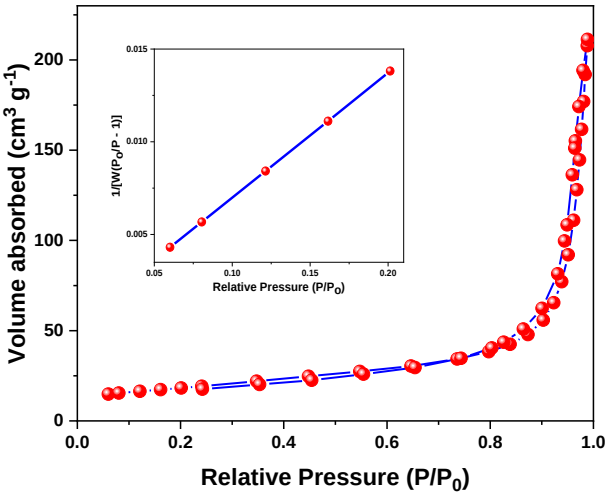

Fig. 5. Nitrogen adsorption-desorption isotherm along with BET adsorption isotherm in the inset for U_{100} sample.

The structural properties of obtained samples were investigated by X-ray diffraction (XRD). Philips X'Pert PRO XRD with Cu Kα radiation (λ = 0,154056 nm, tuned at 40 kV and 30 mA) was used to determine the XRD pattern. The Brunauer–Emmett–Teller (BET) specific surface area of the carbon was measured by obtaining nitrogen adsorption isotherms

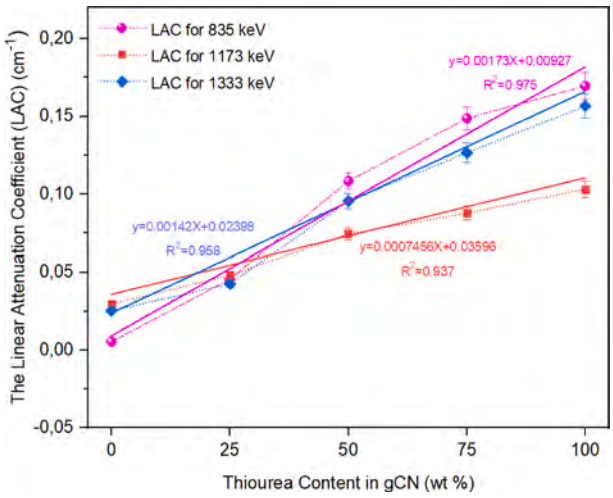

Fig. 6. The Linear Attenuation Coefficient of gCN samples at 835 keV, 1173 keV and 1333 keV gamma energies.

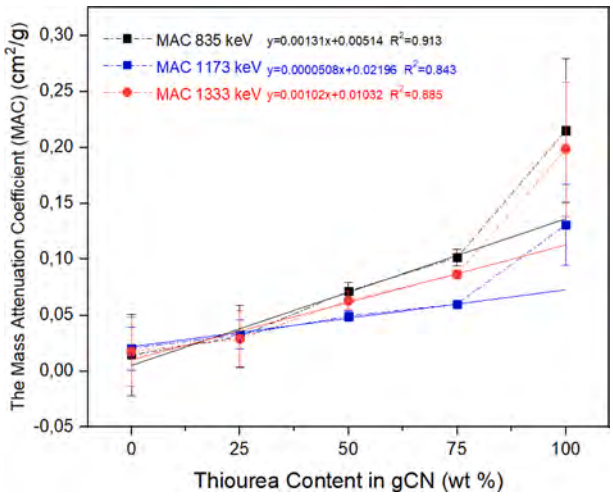

Fig. 7. The Mass Attenuation Coefficient of gCN samples at 835 keV, 1173 keV and 1333 keV gamma energies.

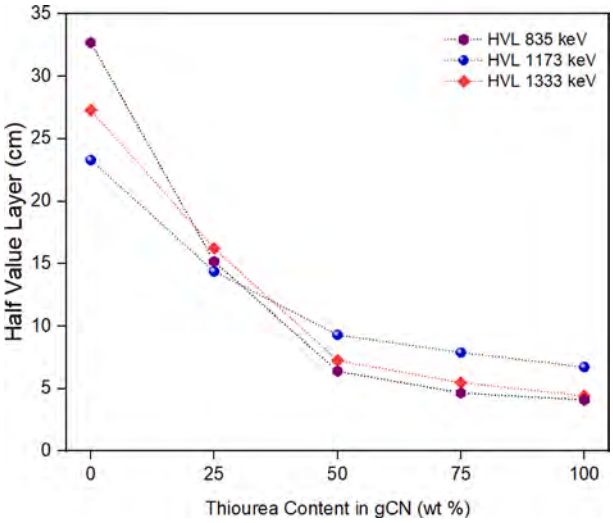

Fig. 8. Half-Value Layer values of gCN samples at 835 keV, 1173 keV and 1333 keV gamma energies.

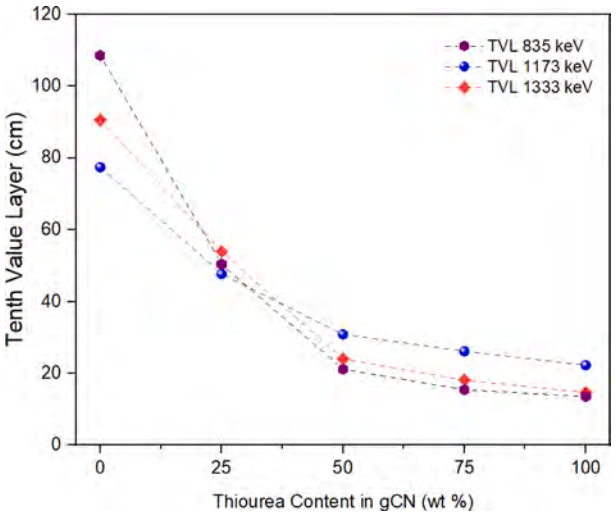

Fig. 9. Tenth-Value Layer values of gCN samples at 835 keV, 1173 keV and 1333 keV gamma energies.

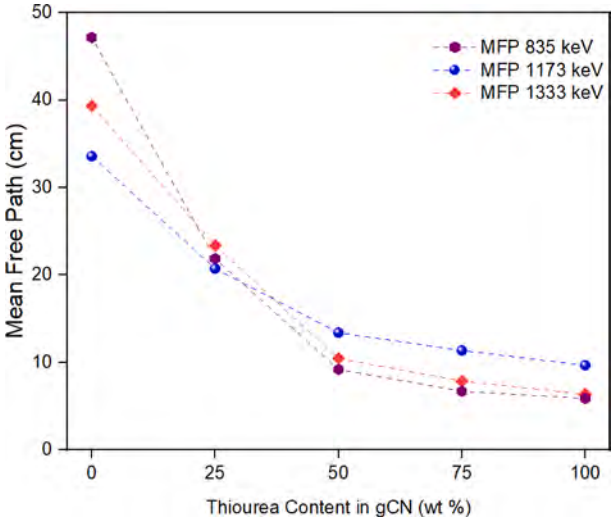

Fig. 10. Mean Free Path values of gCN samples at 835 keV, 1173 keV and 1333 keV gamma energies.

using a Tristar-II 3020 Micromeritics instrument at 77.3 K. For the BET measurements, 0.2–0.3 g of the samples were taken and were subjected to degassing at 200 °C for about 3 h prior to the testing [23].

2.3. Radiation measurements

The radiation attenuation properties of materials are determined by Lambert-Beer's law. The experimental setup shown in Fig. 1 was used for these measurements. The linear attenuation coefficient (LAC) has been given in Eq. (1) as;

$$\mu = \ln\left(\frac{I}{I_0}\right) \Big/ (-x)(\mathrm{cm}^{-1}) \tag{1}$$

x is the thickness in the Lambert-Beer law [24], μ represents the absorption coefficient. I is the gamma number that reaches the detector after interacting with the material and I_0 is the number of gamma that reaches the detector without interacting with the material. The standard deviation of these experimental measurements is found in Eq. (2) [24];

$$\sigma = \sqrt{\frac{\sum_{i=1}^{N}(\mu_i - \overline{\mu})^2}{N-1}} \tag{2}$$

where μ_i is each measurement, $\overline{\mu}$ is the average of the measurements, and N is the number of measurements. The mass attenuation coefficient (MAC) [5] expresses the amount of radiation absorbed by the unit mass and is given in Eq. (3).

$$\mu_m = \frac{\mu}{\rho} = \sum w_i \left(\frac{\mu}{\rho}\right)_i (\mathrm{cm}^2/\mathrm{g}) \tag{3}$$

As can be seen Eq. (3), ρ is the density and w_i is the weight fraction. The material thickness required to reduce the number of incoming gammas by half is Half Value Layer (HVL), the material thickness required to reduce it to one-tenth is Tenth Value Layer (TVL), and the path that gammas can take in the material is Mean Free Path (MFP) [5]. These are given in Eq. 4–6.

$$Half\ \ Value\ \ Layer\ \ (HVL) = \frac{\ln 2}{\mu}(\mathrm{cm}) \tag{4}$$

$$Tenth\ \ Value\ \ Layer\ \ (TVL) = \frac{\ln 10}{\mu}(\mathrm{cm}) \tag{5}$$

$$Mean\ \ Free\ \ Path\ \ (MFP) = \frac{1}{\mu}(\mathrm{cm}) \tag{6}$$

The measurements have been performed using ^{54}Mn and ^{60}Co point radiation sources with 1 μCi activity and 835, 1173 and 1333 keV gamma energies, respectively. To detect ionizing gamma photons experimentally, NaI(Tl) detector (ORTEC® 905–4) based gamma spectrometer have been used as seen in Fig. 1.

3. Results and discussion

The structural properties of the gCN samples were analyzed by X-ray diffraction (XRD) and the XRD patterns are given in Fig. 2. The XRD patterns of all samples are similar. The strong peak at 2θ = 27.3° corresponds to the (0 0 2) plane of gCN, which is attributed to the stacking of the conjugated aromatic layers [26,27]. For the U_{100} sample, there is a broadening at this peak and the peak intensity is lower. The peak intensity of the samples increased with thiourea doping in the samples. This can be attributed to its better crystallinity. Similar XRD peak intensity change is also found in literature [28,29].

Scanning electron microscopy (SEM) was used to investigate the morphology of all samples. SEM images of all samples are shown in Fig. 3. A layered structure similar to graphene is observed in all synthesized samples [30]. When the morphological information obtained is combined, gCN synthesized from urea has a flatter and layered structure compared to gCN synthesized by doped thiourea.

FTIR analysis was performed in the range of 450–4000 cm^{-1} to examine the chemical states of the synthesized gCN samples. FTIR patterns are presented in Fig. 4.a. The broad absorption peak at 3000–3600 cm^{-1} is attributed to the stretching vibration belonging to the N–H group. The peaks in the 1200–1700 cm^{-1} region are characteristic stretching modes of CN heterocycles. The sharp peak seen at 810 cm^{-1} corresponds to the typical breathing mode of triazine units [31,32]. The TGA graph has presented in Fig. 4.b. gCN is known as the most stable allotrope of carbon nitride. It starts to decompose around 500 °C and completely decomposes at 600 °C. The samples exhibited fairly good temperature resistance up to 620 °C. For this reason, it is suitable for application at normal temperatures and even at high temperatures [30-32]. The highest temperature resistance of the samples was observed for $U_{25}T_{75}$.

In the process of synthesizing graphitic carbon nitride from different precursor sources, under the same processing conditions; the change in the properties of the final products is mainly originated from the precursors used have different oxygen and sulfur heteroatoms. Increasing

Table 1
Radiation shielding parameters of gCN samples.

Mn54 835 keV	μ (cm^{-1})	Density (g/cm^3)	HVL (cm)	TVL (cm)	MFP (cm)	μ_m (cm^2/g)
0% Thiourea	0.0212 ± 0.0011	1.4651	32.6922	108.6012	47.1649	0.0144 ± 0.0361
25% Thiourea	0.0456 ± 0.0023	1.4705	15.1756	50.4123	21.8938	0.0310 ± 0.0279
50% Thiourea	0.1084 ± 0.0054	1.5144	6.3936	21.2389	9.2240	0.0715 ± 0.0076
75% Thiourea	0.1487 ± 0.0074	1.4636	4.6587	15.4758	6.7211	0.1016 ± 0.0074
100% Thiourea	0.1696 ± 0.0085	0.7887	4.0869	13.5765	5.8962	0.2150 ± 0.0641
Co60 1173 keV						
0% Thiourea	0.0297 ± 0.0015	1.4651	23.2917	77.3733	33.6028	0.0203 ± 0.0192
25% Thiourea	0.0482 ± 0.0024	1.4705	14.3772	47.7600	20.7419	0.0327 ± 0.0129
50% Thiourea	0.0744 ± 0.0037	1.5144	9.3085	30.9221	13.4293	0.0491 ± 0.0047
75% Thiourea	0.0878 ± 0.0044	1.4636	7.8898	26.2094	11.3826	0.0600 ± 0.0007
100% Thiourea	0.1031 ± 0.0052	0.7887	6.7208	22.3262	9.6961	0.1307 ± 0.0361
Co60 1333 keV						
0% Thiourea	0.0254 ± 0.0013	1.4651	27.2752	90.6061	39.3497	0.0173 ± 0.0308
25% Thiourea	0.0427 ± 0.0021	1.4705	16.2249	53.8979	23.4076	0.0290 ± 0.0249
50% Thiourea	0.0954 ± 0.0048	1.5144	7.2584	24.1118	10.4716	0.0630 ± 0.0079
75% Thiourea	0.1266 ± 0.0063	1.4636	5.4729	18.1805	7.8957	0.0865 ± 0.0038
100% Thiourea	0.1566 ± 0.0078	0.7887	4.4253	14.7006	6.3844	0.1986 ± 0.0598

pyrolysis temperatures enhance surface areas of the synthesized gCN [33]. The surface area of melamine/urea precursors and urea/thiourea precursors have been examined both studies demonstrated that the surface areas increased with increasing concentration of urea [33,34]. In these pelletized materials, the gap between structures with high surface area is greater, which will reduce the effective absorption area [35]. A multi-point BET plot and the N_2 adsorption-desorption isotherm for the U_{100} gCN sample are given together in Fig. 5. It can be seen that the adsorption curve of the gCN sample has shifted upwards. This indicates that it has a larger surface area. Different type IV isotherm is presented with H3 type hysteresis loop in the high partial pressure range up to 1 for U_{100}gCN sample. This indicates that the sample has a mesoporous structure. The specific surface area was found to be approximately 64 m^2/g' from the BET plots [36,37].

The Linear Attenuation Coefficients (LAC) of gCN (graphitic carbon nitride) samples are shown in Fig. 6. Accordingly, the experimentally determined attenuation values at 835 keV gamma energy were determined as 0.0212 ± 0.0011 cm^{-1} for U_{100}, 0.0456 ± 0.0023 cm^{-1} for $U_{75}T_{25}$, 0.1084 ± 0.0054 cm^{-1} for $U_{50}T_{50}$, 0.1487 ± 0.0074 cm^{-1} for $U_{25}T_{75}$ and 0.1696 ± 0.0085 cm^{-1} for T_{100} contribution. When these values were fitted, the R^2 value was obtained as 0.975. At 1173 keV energy, these values were determined as 0.0297 ± 0.0015 cm^{-1}, 0.0482 ± 0.0024 cm^{-1}, 0.0744 ± 0.0037 cm^{-1}, 0.0878 ± 0.0044 cm^{-1} and 0.1031 ± 0.0052 cm^{-1} in samples containing thiourea in the same percentages, and at 1333 keV energy they were found as 0.0254 ± 0.0013 cm^{-1}, 0.0427 ± 0.0021 cm^{-1}, 0.0954 ± 0.0048 cm^{-1}, 0.1266 ± 0.0063 cm^{-1} and 0.1566 ± 0.0078 cm^{-1} for thiourea at the same percentages. When the results obtained at these energy values were fit, the R^2 value was obtained as 0.937 and 0.958, respectively.

In Fig. 7, the Mass Attenuation Coefficient (MAC) values obtained at 835, 1173 and 1333 keV of samples with different rates of urea and thiourea at (0, 25, 50, 75 and 100%) are seen. Similarly, the values obtained at 835 keV gamma energy were obtained as 0.0144 ± 0.0361 cm^2/g for 0%, 0.0310 ± 0.0279 cm^2/g for 25%, 0.0715 ± 0.0076 cm^2/g for 50%, 0.1016 ± 0.0074 cm^2/g for 75% and finally 0.2150 ± 0.0641 cm^2/g for 100%. R^2 values obtained when this value is fit are 0.913. It was obtained as 0.0203 ± 0.0192 cm^2/g, 0.0327 ± 0.0129 cm^2/g, 0.0491 ± 0.0047 cm^2/g, 0.0600 ± 0.0007 cm^2/g and 0.1307 ± 0.0361 cm^2/g for Thiourea contribution in the same ratios at 1173 keV energy and the R^2 value is 0.843. For the final energy value of 1333 keV, it was determined as 0.0173 ± 0.0308 cm^2/g, 0.0290 ± 0.0249 cm^2/g, 0.0630 ± 0.0079 cm^2/g, 0.0865 ± 0.0038 cm^2/g and 0.1986 ± 0.0598 cm^2/g. The R^2 value of these data is 0.885.

Half-Value Layer (HVL) values of synthesized samples are shown in Fig. 8. Firstly, it was measured at 835 keV and according to the results obtained, it was obtained as 32.6922 cm at 0% Thiourea contribution, 15.1756 cm at 25%, 6.3936 cm at 50%, 4.6587 cm at 75% and 4.0869 cm at 100% Thiourea contribution. At 1173 keV, these results were found to be 23.2917 cm at 0% Thiourea contribution, 14.3772 cm at 25%, 9,3085 cm at 50%, 7.8898 cm at 75% and 6.7208 cm at 100% Thiourea contribution. Finally, at 1333 keV, it was obtained as 27.2752 cm at 0% Thiourea, 16.2249 cm at 25%, 7.2584 cm at 50%, 5.4729 cm at 75%, and 4.4253 cm at 100% Thiourea.

Tenth-Value Layer values are shown in Fig. 9. Here, according to the values measured at 885 keV, it was found to be 108.6012 cm at 0% Thiourea contribution, 50.4123 cm at 25%, 21.2389 cm at 50%, 15.4758 cm at 75% and 13.5765 cm at 100% Thiourea contribution. At 1173 keV, these results were found to be 77.3733 cm at 0% Thiourea contribution, 47.7600 cm at 25%, 30.9221 cm at 50%, 26.2094 cm at 75% and 22.3262 cm at 100% Thiourea contribution. Finally, at 1333 keV, it was obtained as 90.6061 cm at 0% Thiourea, 53.8979 cm at 25%, 24.1118 cm at 50%, 18.1805 cm at 75%, and 14.7006 cm at 100% Thiourea.

Fig. 10 shows the mean free path values of gCN samples. Values of 47.1649 cm at U_{100}, 21.8938 cm at $U_{75}T_{25}$, 9.2240 cm at $U_{50}T_{50}$, 6.7211 cm at $U_{25}T_{75}$ and 5.8962 cm at T_{100} were obtained at 885 keV. At 1173 keV energy, it was obtained as 33.6028 cm in U_{100} contribution, 20.7419 cm in $U75T_{25}$ contribution, 13.4293 cm in $U_{50}T_{50}$ contribution, 11.3826 cm in $U_{25}T_{75}$ contribution and 9.6961 cm in T_{100} contribution. Finally, at 1333 keV energy, 39.3497 cm was obtained in U_{100} contribution, 23.4076 cm in $U_{75}T_{25}$ contribution, 10.4716 cm in $U_{50}T_{50}$ contribution, 7.8957 cm in $U_{25}T_{75}$ contribution and 6.3844 cm in T_{100} contribution. All obtained results can be seen in Table 1.

To make a comparison, considering the HVL values obtained with ^{60}Co point radiation source, for example, 7.43 cm value was obtained in concrete [38], while this value was obtained as 7.8898 cm at 1173 keV and 5.4729 cm in %75 thiourea doped gCN material. Also, TVL value of this concrete is 24.68 cm [38], while this value was obtained as 26.2094 cm at 1173 keV and 18.1805 cm in %75 thiourea doped gCN material.

4. Conclusion

gCN (graphitic carbon nitride) can be used in many areas such as sensing, biomedical applications, wastewater and environmental treatment, solar energy use and device construction. In addition to these, it is important to examine the radiation shielding properties of gCN. For this

purpose, gCN synthesized from different ratios of urea and thiourea (0, 25, 50, 75 and 100%) were produced and their radiation shielding properties were investigated. The radiation shielding properties of the synthesized samples is examined at three different (885, 1173 and 1333 keV) gamma energies. According to the results obtained here, the Linear Attenuation Coefficients of the samples increased as the amount of thiourea in the obtained samples. Again, the Mass Attenuation Coefficient values of the samples increased with the increase in the amount of thiourea. In the HVL, TVL and MFP calculations made using the LAC value, these values decreased as the thiourea contribution in the produced materials. As can be understood from these results, it has been determined that synthesized gCN provides effective results in radiation shielding.

5. Data availability

Data will be made available on request.

CRediT authorship contribution statement

Yusuf Kavun: Conceptualization, Methodology, Data curation, Writing – original draft, Visualization, Investigation, Validation, Writing – review & editing. **Hasan Eskalen:** Conceptualization, Methodology, Data curation, Writing – original draft, Visualization, Investigation, Validation, Writing – review & editing. **Mustafa Kavgacı:** Conceptualization, Methodology, Data curation, Writing – original draft, Visualization, Investigation, Validation, Writing – review & editing.

Declaration of Competing Interest

The authors declare that they have no known competing financial interests or personal relationships that could have appeared to influence the work reported in this paper.

Data availability

Data will be made available on request.

Acknowledgements

This study was supported by the Scientific Research Projects Coordination Unit of Kahramanmaraş Sütçü İmam University. Project numbers 2020/7-18M, 2020/7-19M, 2020/7-21M and 2021/3-2 YLS.

References

[1] R. Kurtulus, C. Kurtulus, T. Kavas, Nuclear radiation shielding characteristics and physical, optical, mechanical, and thermal properties of lithium-borotellurite glass doped with Rb2O, Prog. Nucl. Energy 141 (2021), 103961.
[2] M. Kamislioglu, Research on the effects of bismuth borate glass system on nuclear radiation shielding parameters, Results Phys. 22 (2021), 103844.
[3] H.A. Saudi, H.O. Tekin, H.M.H. Zakaly, S.A.M. Issa, G. Susoy, M. Zhukovsky, The impact of samarium (III) oxide on structural, optical and radiation shielding properties of thallium-borate glasses: Experimental and numerical investigation, Opt. Mater. (Amst). 114 (2021) 110948.
[4] Z. Li, W. Zhou, X. Zhang, Y. Gao, S. Guo, High-efficiency, flexibility and lead-free X-ray shielding multilayered polymer composites: layered structure design and shielding mechanism, Sci. Rep. 11 (2021) 4384, https://doi.org/10.1038/s41598-021-83031-4.
[5] Y. Kavun, S. Kerli, H. Eskalen, M. Kavgacı, Characterization and nuclear shielding performance of Sm doped In2O thin films, Radiat. Phys. Chem. 194 (2022), 110014.
[6] M. Alqahtani, F. Ercan, N.A. Saleh, M.H.A. Mhareb, N. Dwaikat, M.I. Sayyed, F. Abokhamis, A. Abdulrazzaq, B. Özcelik, I. Ercan, Structural, magnetic and gamma-ray shielding features of Zn doped Mg2FeTiO6 double perovskite, Phys. B Condens. Matter. 640 (2022), 414024.
[7] H. Yaykaşlı, H. Eskalen, Y. Kavun, M. Gögebakan, Microstructural, thermal, and radiation shielding properties of Al50B25Mg25 alloy prepared by mechanical alloying, J. Mater. Sci. Mater. Electron. 33 (2022) 2350–2359, https://doi.org/10.1007/s10854-021-07434-9.
[8] H. Eskalen, Y. Kavun, S. Kerli, S. Eken, An investigation of radiation shielding properties of boron doped ZnO thin films, Opt Mater (Amst). 105 (2020), 109871.
[9] Y. Kavun, H. Eskalen, S. Kerlï, M. Kavgaci, Fabrication and characterization of GdxFe2O3 (100-x)/PVA (x= 0, 5, 10, 20) composite films for radiation shielding, Appl. Radiat. Isotopes 177 (2021) 109918.
[10] M.I. Sayyed, O. Agar, A. Kumar, H.O. Tekin, D.K. Gaikwad, S.S. Obaid, Shielding behaviour of (20+ x) Bi2O3–20BaO–10Na2O–10MgO–(40–x) B2O3: An experimental and Monte Carlo study, Chem. Phys. 529 (2020), 110571.
[11] M. Elsafi, M.A. El-Nahal, M.I. Sayyed, I.H. Saleh, M.I. Abbas, Effect of bulk and nanoparticle Bi2O3 on attenuation capability of radiation shielding glass, Ceram. Int. 47 (2021) 19651–19658, https://doi.org/10.1016/j.ceramint.2021.03.302.
[12] M.A. El-Nahal, M. Elsafi, M.I. Sayyed, M.U. Khandaker, H. Osman, B.H. Elesawy, I. H. Saleh, M.I. Abbas, Understanding the effect of introducing micro-and nanoparticle bismuth oxide (Bi2o3) on the gamma ray shielding performance of novel concrete, Materials 14 (2021), https://doi.org/10.3390/ma14216487.
[13] Y. Al-Hadeethi, M.I. Sayyed, A.Z. Barasheed, M. Ahmed, M. Elsafi, Preparation and radiation attenuation properties of ceramic ball clay enhanced with micro and nano ZnO particles, J. Mater. Res. Technol. 17 (2022) 223–233, https://doi.org/10.1016/j.jmrt.2021.12.109.
[14] A.M. El-Khatib, T.I. Shalaby, A. Antar, M. Elsafi, Improving Gamma Ray Shielding Behaviors of Polypropylene Using PbO Nanoparticles: An Experimental Study, Materials 15 (2022) 3908, https://doi.org/10.3390/ma15113908.
[15] O. Altan, Impact of graphitic carbon nitrides synthesized from different precursors on Schottky junction characteristics, Turk J Chem. 45 (2021) 1057–1069, https://doi.org/10.3906/kim-2012-45.
[16] M. Aggarwal, S. Basu, N.P. Shetti, M.N. Nadagouda, E.E. Kwon, Y.-K. Park, T. M. Aminabhavi, Photocatalytic carbon dioxide reduction: Exploring the role of ultrathin 2D graphitic carbon nitride (g-C3N4), Chem. Eng. J. 425 (2021), 131402, https://doi.org/10.1016/j.cej.2021.131402.
[17] H. Medetalibeyoğlu, An investigation on development of a molecular imprinted sensor with graphitic carbon nitride (g-C3N4) quantum dots for detection of acetaminophen, Carbon Lett. 31 (2021) 1237–1248, https://doi.org/10.1007/s42823-021-00247-0.
[18] D. Nemati, M. Ashjari, H. Rashedi, F. Yazdian, M. Navaei-Nigjeh, <scp>PVA</scp> based nanofiber containing cellulose modified with graphitic carbon nitride/nettles/trachyspermum accelerates wound healing, Biotechnol. Prog. 37 (2021) e3200.
[19] O.G. Torres, G. Gordillo, M.C. Plazas, D.A. Landínez Té Llez, J. Roa-Rojas, Optical features of PbBr 2 semiconductor thin films for radiation attenuation application, (n.d.). 10.1007/s10854-021-06257-y.
[20] R. Rasmidi, M. Duinong, F.P. Chee, Radiation damage effects on zinc oxide (ZnO) based semiconductor devices– a review, Radiat. Phys. Chem. 184 (2021), 109455, https://doi.org/10.1016/J.RADPHYSCHEM.2021.109455.
[21] R.C. Dante, P. Martín-Ramos, A. Correa-Guimaraes, J. Martín-Gil, Synthesis of graphitic carbon nitride by reaction of melamine and uric acid, Mater. Chem. Phys. 130 (2011) 1094–1102, https://doi.org/10.1016/J.MATCHEMPHYS.2011.08.041.
[22] T.O. Ajiboye, A.T. Kuvarega, D.C. Onwudiwe, Graphitic carbon nitride-based catalysts and their applications: A review, Nano-Structures Nano-Objects 24 (2020), 100577, https://doi.org/10.1016/J.NANOSO.2020.100577.
[23] M.R. Toroghinejad, H. Pirmoradian, A. Shabani, Synthesis of FeCrCoNiCu high entropy alloy through mechanical alloying and spark plasma sintering processes, Mater. Chem. Phys. 289 (2022), 126433, https://doi.org/10.1016/j.matchemphys.2022.126433.
[24] K.S. Krane, W.G. Lynch, Introductory Nuclear Physics, Phys. Today (1989), https://doi.org/10.1063/1.2810884.
[25] H. Eskalen, Y. Kavun, S. Kerli, S. Eken, An investigation of radiation shielding properties of boron doped ZnO thin films, Opt. Mater. (Amst) 105 (2020), https://doi.org/10.1016/j.optmat.2020.109871.
[26] L. Florentino-Madiedo, E. Díaz-Faes, C. Barriocanal, Relationship between gCN structure and photocatalytic water splitting efficiency, Carbon N Y. 187 (2022) 462–476, https://doi.org/10.1016/j.carbon.2021.11.030.
[27] L. Yang, X. Liu, Z. Liu, C. Wang, G. Liu, Q. Li, X. Feng, Enhanced photocatalytic activity of g-C3N4 2D nanosheets through thermal exfoliation using dicyandiamide as precursor, Ceram. Int. 44 (2018) 20613–20619, https://doi.org/10.1016/j.ceramint.2018.06.105.
[28] J. Theerthagiri, R.A. Senthil, J. Madhavan, B. Neppolian, A Comparative Study on the Role of Precursors of Graphitic Carbon Nitrides for the Photocatalytic Degradation of Direct Red 81, Mater. Sci. Forum 807 (2015) 101–113, https://doi.org/10.4028/WWW.SCIENTIFIC.NET/MSF.807.101.
[29] V. Ragupathi, P. Panigrahi, N. Ganapathi Subramaniam, Bandgap engineering in graphitic carbon nitride: Effect of precursors, Optik (Stuttg). 202 (2020) 163601. 10.1016/J.IJLEO.2019.163601.
[30] S. Krishnaswamy, S. Gunasekar, P. ghosh, V. Ragupathi, P. Panigrahi, G.S. Nagarajan, Enhancement of photoluminescence intensity of epoxy thin-film resin by nano graphitic carbon nitride, Physica B Condens Matter. 632 (2022) 413718. 10.1016/J.PHYSB.2022.413718.
[31] Y. Yang, J. Chen, Z. Mao, N. An, D. Wang, B.D. Fahlman, Ultrathin g-C3N4 nanosheets with an extended visible-light-responsive range for significant enhancement of photocatalysis, RSC Adv. 7 (2017) 2333–2341, https://doi.org/10.1039/C6RA26172H.
[32] J. Wang, M. Li, S. Zhou, A. Xue, Y. Zhang, Y. Zhao, J. Zhong, Q. Zhang, Graphitic carbon nitride nanosheets embedded in poly(vinyl alcohol) nanocomposite membranes for ethanol dehydration via pervaporation, Sep. Purif. Technol. 188 (2017) 24–37, https://doi.org/10.1016/J.SEPPUR.2017.07.008.
[33] Y. Zheng, Z. Zhang, C. Li, A comparison of graphitic carbon nitrides synthesized from different precursors through pyrolysis, J. Photochem. Photobiol. A Chem. 332 (2017) 32–44, https://doi.org/10.1016/J.JPHOTOCHEM.2016.08.005.

[34] D. Gogoi, A.K. Shah, M. Qureshi, A.K. Golder, N.R. Peela, Silver grafted graphitic-carbon nitride ternary hetero-junction Ag/gC3N4(Urea)-gC3N4(Thiourea) with efficient charge transfer for enhanced visible-light photocatalytic green H2 production, Appl. Surf. Sci. 558 (2021), 149900, https://doi.org/10.1016/J.APSUSC.2021.149900.

[35] S. Kim, Y. Ahn, S.H. Song, D. Lee, Tungsten nanoparticle anchoring on boron nitride nanosheet-based polymer nanocomposites for complex radiation shielding, Compos. Sci. Technol. 221 (2022), 109353, https://doi.org/10.1016/J.COMPSCITECH.2022.109353.

[36] D. Rattan Paul, S.P. Nehra, Graphitic carbon nitride: a sustainable photocatalyst for organic pollutant degradation and antibacterial applications, Environ. Sci. Pollut. Res. 28 (2021) 3888–3896, https://doi.org/10.1007/s11356-020-09432-6.

[37] Y. Duan, X. Li, K. Lv, L. Zhao, Y. Liu, Flower-like g-C3N4 assembly from holy nanosheets with nitrogen vacancies for efficient NO abatement, Appl Surf Sci. 492 (2019) 166–176, https://doi.org/10.1016/j.apsusc.2019.06.125.

[38] Kayihan Kutlu Sevinc, Seda Tonuk, Elementary school buildings with the direction of sustainability awareness construction. , JOURNAL OF POLYTECHNIC-POLITEKNIK DERGISI. 14 (2011) 163–171.

Applied Radiation and Isotopes 203 (2024) 111086

Contents lists available at ScienceDirect

Applied Radiation and Isotopes

journal homepage: www.elsevier.com/locate/apradiso

A novel vanadium pentoxide doped glasses characterization for radiation shielding applications

Yusuf Kavun [a,e,*], Hasan Eskalen [b,e], Mustafa Kavgacı [c,e], Hakan Yaykaşlı [d,f], Medeni Bahşi [e]

[a] Vocational School of Health Services, Department of Medical Imaging Techniques, Kahramanmaraş Sütçü İmam University, Kahramanmaras, Turkey
[b] Vocational School of Health Services, Department of Opticianry, Kahramanmaraş Sütçü İmam University, Kahramanmaraş, Turkey
[c] Elbistan Vocational School of Health Services, Department of Opticianry, Kahramanmaraş İstiklal University, Kahramanmaraş, 46300, Turkey
[d] Elbistan Vocational School of Higher Education, Kahramanmaras İstiklal University, Kahramanmaraş, Turkey
[e] Institute of Science, Department of Material Science and Engineering, Kahramanmaraş Sütçü İmam University, Kahramanmaraş, 46050, Turkey
[f] Institute of Graduate Studies, Department of Material Science and Engineering, Kahramanmaraş İstiklal University, Kahramanmaraş, Turkey

ARTICLE INFO

Keywords:
Vanadium pentoxide
Glass
Radiation shielding
TGA
XRD

ABSTRACT

Glasses are actively used in various fields, from industry to health. Especially, special doped glasses used in radiation areas may vary depending on the type and energy of the radiation. Glasses made of high-density and effective radiation-absorbing materials generally provide adequate protection against X and gamma rays. As an example, in this study, a $42.5P_2O_5$–$42.5B_2O_3$–$(15-x)Li_2O$–xV_2O_5 (x = 0, 2.5, 5, 10 and 15) glass system was produced using the melt quenching technique. The obtained X-ray patterns indicated that lack of crystalline peaks, verifying the glassy nature of all synthesized glass series. The glass transition temperatures and the glass thermal stability were determined using a Differential Thermal Analysis (TGA). The glass transition temperature and thermal stability was found to deteriorate with increasing V_2O_5 content. The radiation absorption properties of these glass system produced were investigated with 384 keV, 1173 keV and 1333 keV energized gamma using narrow beam transmission geometry. The NaI(Tl) detector system have been used to obtain γ-ray spectra. According to the obtained mass attenuation coefficients (μ_m) results, it has been determined that as the V_2O_5 ratio in the glass increases, it provides more effective results in radiation shielding. When the experimental results are compared with the theoretical XCOM results, there are a good match between the values. Finally, the radiation shielding properties of this produced glass system are compared with previously studied standard glasses to refer to the superiority of the installed systems.

1. Introduction

Understanding the impact of radiation on human health is an evolving field. Effective shielding is crucial to minimize radiation exposure from natural and artificial sources. The key principle in radiation shielding involves using a material that interacts significantly with radiation particles, causing them to lose energy through various interactions and ultimately be absorbed by the material (Knoll and Kraner, 1981) (Niksarlıoğlu et al., 2023) (Hannachi et al., 2023) (James E. Martin and Tanır G, 2013). Glass, a rare and versatile substance, possesses qualities such as rigidity, brittleness, and high compression resistance. It also exhibits resistance to chemical effects from air, water, and various acids. Composed of inorganic substances fused at high temperatures, glass primarily consists of alkalis, earthy bases, or metallic oxides of silica. It is abundant in nature in forms such as silica, flint, quartz, and sand to create glass, sand, alkali, and lead oxide must be heated to high temperatures The mixture, when heated, undergoes solvent action from fused alkali and lead oxide until it transforms into a molten glass mass (Hlavae, 1983) (Holand and Beall, 2019) (Jeager, 1975).

Vanadium, possessing five outer valence electrons, shares chemical similarities with nitrogen, phosphorus, arsenic, and antimony (Fritsch et al., 1987). Much like nitrogen, it gives rise to oxides in states of five, four, three, and potentially monovalent. Additionally, it exhibits a propensity for the formation of various vanadates—ortho-, pyro-, meta- and poly-, nearly as abundantly as the radicals formed by pentavalent phosphorus. Notably, vanadium mirrors phosphorus in its tendency to produce glassy vanadium pentoxide (Gaddam et al., 2021). In terms of

* Corresponding author. Vocational School of Health Services, Department of Medical Imaging Techniques, Kahramanmaraş Sütçü İmam University, Kahramanmaras, Turkey.
E-mail addresses: yusufkavun@gmail.com, yusufkavun@ksu.edu.tr (Y. Kavun).

https://doi.org/10.1016/j.apradiso.2023.111086
Received 2 May 2023; Received in revised form 23 October 2023; Accepted 24 October 2023
Available online 27 October 2023

Table 1
Chemical composition of the glasses.

Glass code	Composition (mol%)				Density (g/cm^3)
	V_2O_5	Li_2O	B_2O_3	P_2O_5	
Y0	0	15	42.5	42.5	2.472
Y1	2.5	12.5	42.5	42.5	2.473
Y2	5	10	42.5	42.5	2.482
Y3	10	5	42.5	42.5	2.497
Y4	15	0	42.5	42.5	2.521

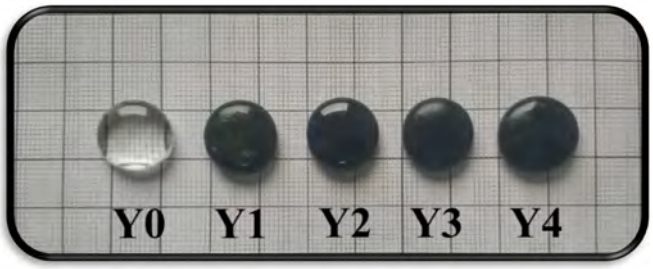

Fig. 1. Image of produced glass samples.

appearance, compounds of vanadium bear a closer resemblance to neighboring transition elements like Oria, iron, and notably, chromium. Bivalent vanadium stands out as a potent reducing agent, giving rise to salts with a distinctive lavender hue. In its oxide form, vanadium dioxide acts as an insulator, effectively retaining indoor heat while allowing the full spectrum of sunlight to permeate from the outside (Fritsch et al., 1987; Shen et al., 2021). However, at elevated surface temperatures, it undergoes a transformation into a metallic state, impeding the penetration of heat-causing infrared solar radiation (Weyl et al., 1939; Masayuki Yamane, 2004).

Boro-phosphate glasses find applications in nonlinear optics and solid-state batteries. Among these, lithium borophosphate stands out as a traditional yet highly acclaimed glass, particularly in the realm of storage batteries, owing to its distinct advantages. These batteries serve as essential energy storage solutions for both optical and electrical equipment (Alrowaili et al., 2022). Moreover, lithium-borate glasses are recognized for their capacity to maintain low production temperatures, enhanced solubility, and improved thermal stability, thanks to the robust ionic interactions among cations within the glass network. The introduction of Li_2O into these glasses leads to a transformation of bridging oxygen into non-bridging oxygen. Consequently, lithium-boro-phosphate glasses exhibit exceptional physical and chemical stability, coupled with reliable voltage performance, making them a valuable choice as solid electrolytes, especially due to their improved ionic conductivities (Madhu et al., 2023a).

The fundamental principle of radiation shielding hinges on the material's capacity to engage extensively with radiation particles. Through a series of interactions, these particles dissipate their energy, ultimately leading to their absorption by the shielding material (Krane, 1991). The Li_2O–B_2O_3–P_2O_5 glass series was synthesized and the influence of TeO_2 on its radiation shielding properties was examined. The results demonstrate that the incorporation of TeO_2 into the glass samples had a beneficial impact on their nuclear protection capabilities was reported (Susoy, 2020). Numerous studies have demonstrated the pivotal role of transition metal oxides (TMOs) in the fabrication of glass. Among these, vanadium oxide (V_2O_5) stands out as an intriguing TMO, serving as a conditioning agent to enhance the electrical, optical, and magnetic properties of the resultant glasses (Rammah et al., 2020a). To improve performance V_2O_5 -Li_2O– P_2O_5 glass system, the effects of incremental doping with a transition metal oxide (V_2O_5) on both the anticipated nonlinear and linear optical parameters was examined (Ravisankar et al., 2019). Recently, it has been reported that boron-rich glasses provide poorer radiation shielding than phosphate-rich glasses (Gomaa et al., 2021). Another study reported that as the WO_3 content in lithium borate glasses increases, there is an observed increase in the mass attenuation coefficient, effective atomic number, and stiffness values (Uosif et al., 2020). Also, vanadyl lead phosphate glasses have the potential to serve as an effective radiation shielding material was revealed from the recent study (Rammah et al., 2020b).

In this investigation, a glass system comprising $42.5P_2O_5$, $42.5B_2O_3$, and $(15-x)Li_2O$–xV_2O_5 (with x values of 0, 2.5, 5, 10, and 15) was fabricated through the melt extinguishing system technique. The produced glass system underwent irradiation using a ^{133}Ba and ^{60}Co point source with 1 mCi activity. Gamma spectra with energies of 384 keV, 1173 keV, and 1333 keV were subsequently measured utilizing a NaI(Tl) detector (Kavun et al., 2022). Comparison of the experimental outcomes with those obtained from the XCOM simulation code (Berger and Hubbell, 1987), reveals a strong alignment between the values. Finally, the radiation shielding properties of the newly developed glass system are juxtaposed with those of previously investigated standard glasses, illustrating the superiority of the implemented systems.

2. Material and method

2.1. Glasses preparation

The well-established melt-quench process was employed to fabricate V_2O_5 -doped glasses with varying compositions: x V_2O_5 - (15-x) Li_2O – 42.5 B_2O_3 – 42.5 P_2O_5, where x took values of 0, 2.5, 5, 10, and 15 mol % denoted as Y0, Y1, Y2, Y3, and Y4, respectively. The components, along with their respective quantities as listed in Table 1, were meticulously blended. This amalgam was then transferred into alumina crucibles, which were subsequently placed in the furnace, set at 1150 °C. Throughout the melting process, continuous agitation was maintained to prevent the formation of bubbles. The resulting melts were poured into steel molds and transferred to a 400 °C furnace for annealing, a process that lasted for 4 h before allowing natural cooling. In Fig. 1, visual representations of the manufactured glass samples are presented.

2.2. Characterization

Structural characterization of the synthesized glass samples was carried out by XRD device. The amorphous structure of the glasses was obtained by the X-ray diffractometer (Philips X'Pert PRO, Netherland) using Cu-kα radiation source (λ = 1.54 Å). The microhardness of the glass samples was investigated with a Shimadzu microhardness tester. The Vickers microhardness of the glasses samples was measured using a Vickers tester (Shimadzu HMV-2 Machine, Japan) for 15 s under a load of 2.942N, and the average hardness was obtained from 10 indents. The thermal properties were established by differential thermal analysis (DTA-Perkin-Elmer Sapphire, USA) in a nitrogen atmosphere. A heating rate of 15 °C/min was implemented in the temperature range of 200°C–900 °C. The chemical functionalities of the synthesized glasses were investigated by FTIR analysis. The Perkin Elmer Spectrum 400 device (USA) was used to obtain FT-IR spectra in the 4000 cm^{-1} - 400 cm^{-1} range.

2.3. γ-ray spectra

Radiation measurements were carried out in the experimental setup given in Fig. 2. Accordingly, the Linear Attenuation Coefficient (μ) (LAC) is calculated with Lambert-Beer's law (Kavun et al., 2021) given in Eq. (1). where I_0 is the gamma measured without glass in the experimental setup, and I is the gamma number measured after the glasses are placed in the experimental setup. Although x is expressed as the thickness of the glass here, the glass thicknesses are produced the same. instead, the amount of V_2O_5 in the glass changes.

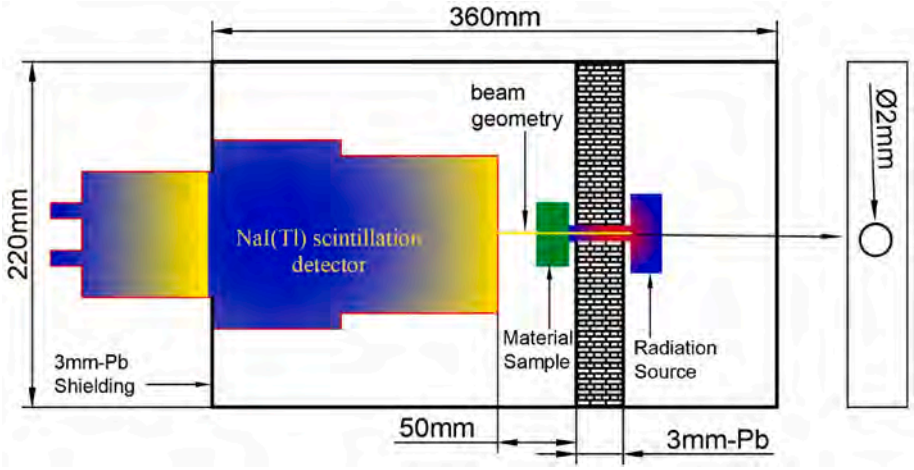

Fig. 2. Experimental schema of radiation shielding measurements.

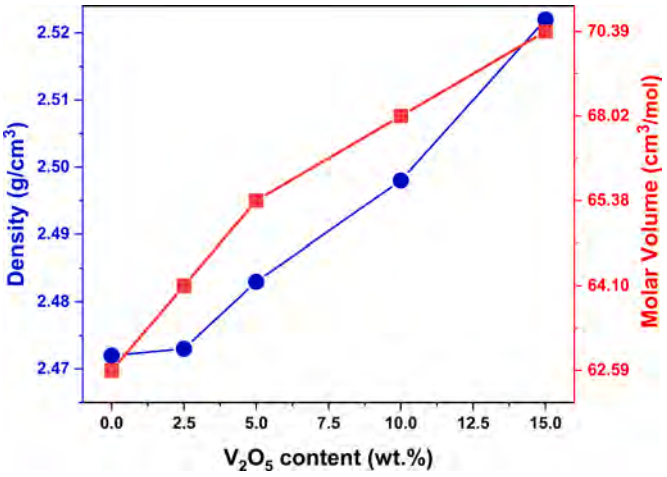

Fig. 3. Density and molar volume for the glass samples.

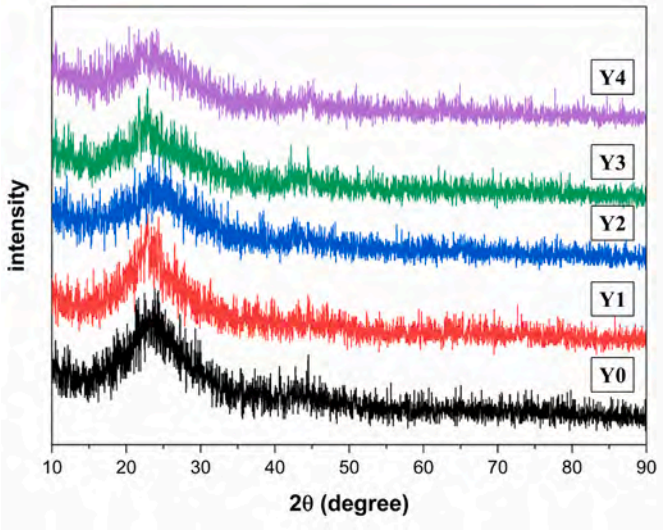

Fig. 5. X-Ray diffraction pattern of Y-series glasses.

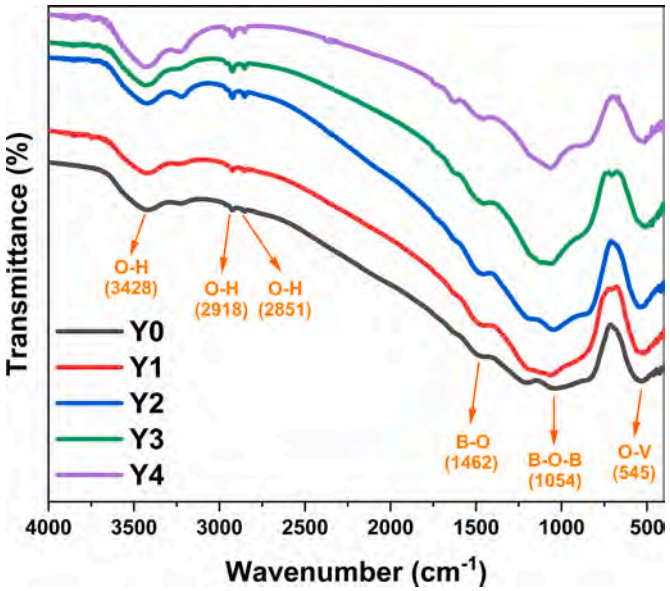

Fig. 4. FTIR spectra of glass samples.

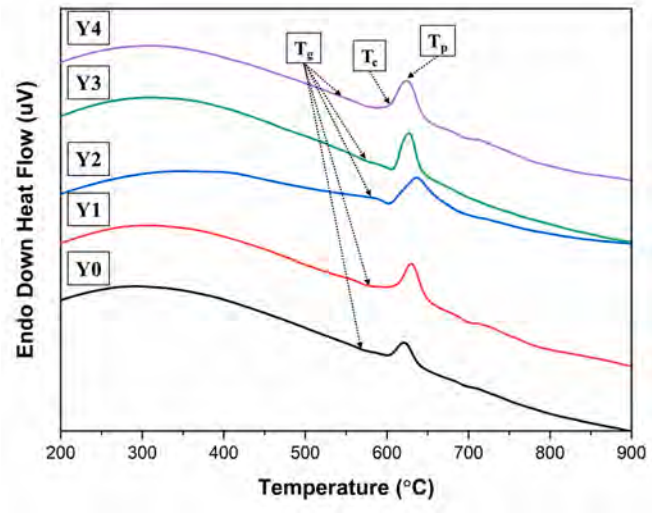

Fig. 6. DTA graphs of Y series glasses.

Table 2
DTA of the prepared glasses.

Sample Code	T_g(°C)	T_c(°C)	T_p(°C)	ΔT(°C)
Y0	572	604	622	32
Y1	575	608	628	33
Y2	583	614	636	31
Y3	581	611	625	30
Y4	549	578	624	29

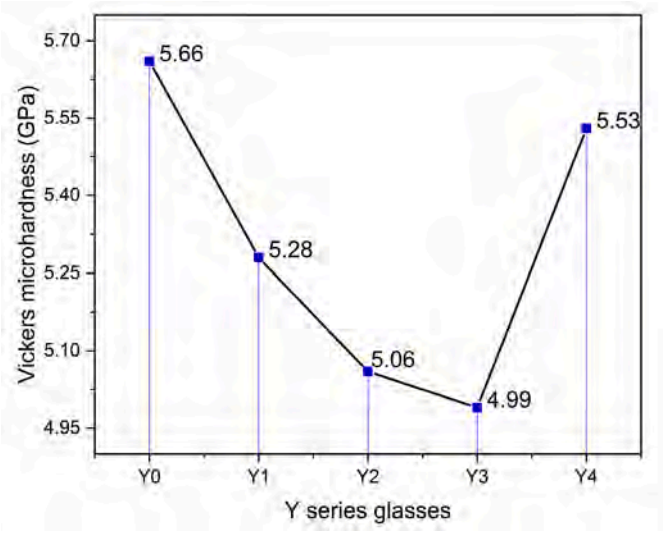

Fig. 7. Variation of micro-hardness for the $42.5P_2O_5$–$42.5B_2O_3$–(15−x) Li_2O–xV_2O_5 glasses.

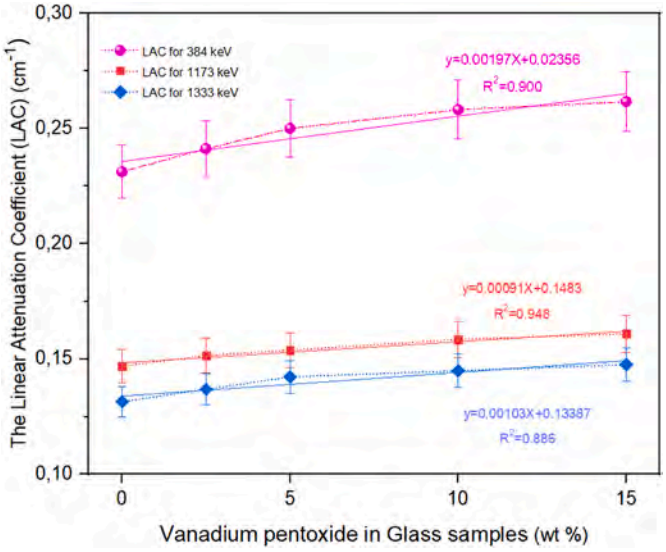

Fig. 8. μ Values of V_2O_5 doped glasses.

$$\mu = \ln\left(\frac{I_0}{I}\right) \Big/ (-x)\,(\mathrm{cm}^{-1}) \tag{1}$$

By using obtained μ, the standart deviation (Yaykaşlı et al., 2022) of these experiments have been calculated via Eq. (2):

$$\sigma = \sqrt{\frac{\sum_{i=1}^{N}(\mu_i - \overline{\mu})^2}{N-1}} \tag{2}$$

Each measurement is represented by μ_i and the average of the

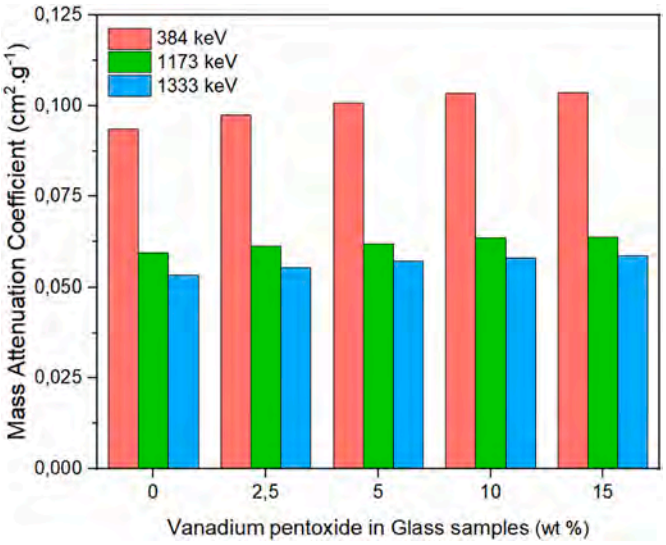

Fig. 9. The Mass attenuation coefficient values of V_2O_5 doped glasses.

measurements are represented by $\overline{\mu}$. N is the number of measurements of every glass sample. The amount of radiation absorbed by a unit mass is found by the mass attenuation coefficient and this is given in Eq. (3) (Kavun et al., 2021):

$$\mu_m = \frac{\mu}{\rho}\ (\mathrm{cm}^2/\mathrm{g}) \tag{3}$$

here, the linear attenuation coefficient is μ and density is ρ.

The material thickness that halves the incoming gamma number is calculated with Half Value Layer (HVL), and the material thickness that reduces it to one-tenth is calculated with Tenth Value Layer (TVL). These are given in Eqs. (4) and (5), respectively (Eskalen et al., 2020). The path taken by the gamma in the material is calculated with the Mean Free Path (MFP) given in Eq. (6) (Eskalen et al., 2020).

$$\textit{Half Value Layer}\ (HVL) = \frac{\ln 2}{\mu}\ (\mathrm{cm}) \tag{4}$$

$$\textit{Tenth Value Layer}\ (TVL) = \frac{\ln 10}{\mu}(\mathrm{cm}) \tag{5}$$

$$\textit{Mean Free Path}\ (MFP) = \frac{1}{\mu}(\mathrm{cm}) \tag{6}$$

^{133}Ba and ^{60}Co point source with 1 mCi activity have been used for irradiation and 384 keV, 1173 keV, and 1333 keV energized gamma have been measured by using NaI(Tl) detector system (ORTEC® 905-4) (Yaykaşlı et al., 2022). This experimental setup has been given in Fig. 2.

2.4. Density and molar volume

A 4-digit precise microbalance (Axiss ACN 220) was used to calculate the density of the glass samples using Archimedes' principle. The density of the obtained glass was calculated by using the equation;

$$\rho = \frac{w_A}{w_A - w_B}\, x\rho_{liquid}\ (\mathrm{g}/\mathrm{cm}^3) \tag{7}$$

here, ρ, w_A, w_B and ρ_{liquid} is density of glass sample, weight of obtained glass in air, weight of obtained glass in liquid and density of liquid respectively. The molar volume (V_M) of glass samples is an essential physical parameter that may be estimated using the sample's molecular weight (M) and observed density value (Mandal et al., 2023). The molar volume (V_g) of the synthesized glass might be obtained from the following equation;

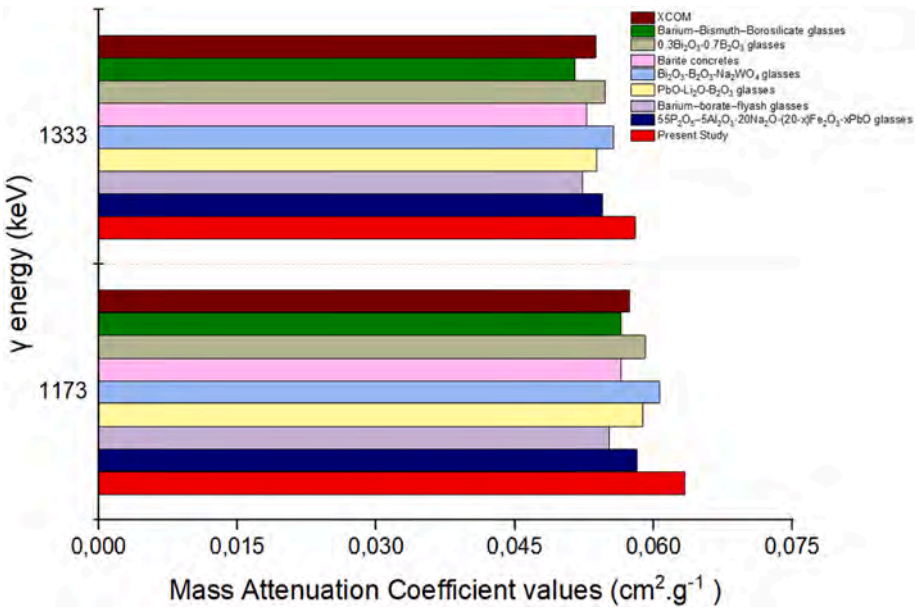

Fig. 10. The Mass attenuation coefficient comparison of some shielding materials with present 10% V_2O_5 doped glasses.

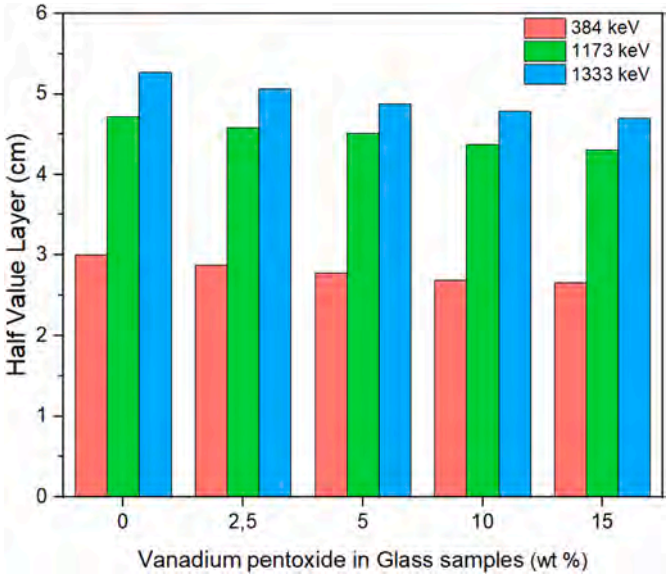

Fig. 11. Half Value Layer (HVL) values of V_2O_5 doped glasses.

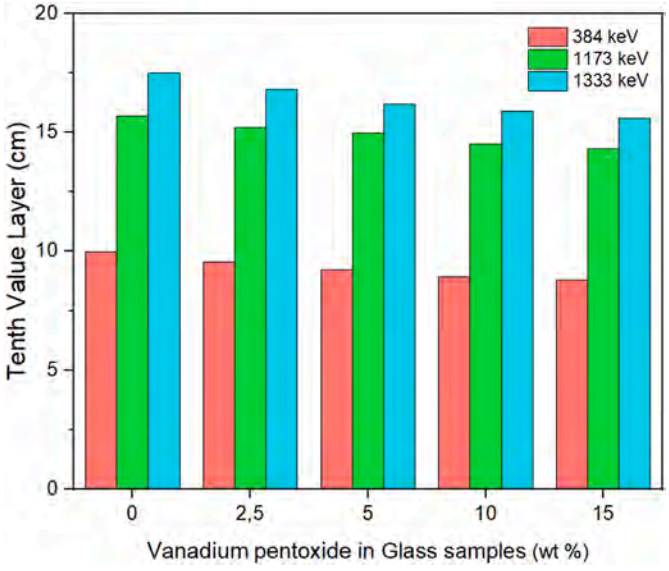

Fig. 12. Tenth Value Layer (TVL) values of V_2O_5 doped glasses.

$$V_g = \frac{M}{\rho}\ \left(\mathrm{cm}^3/\mathrm{mol}\right) \tag{8}$$

where, M is defined as molar mass.

3. Results and discussion

Fig. 3 presents the computed densities (ρ) and molar volumes (V_m) of the fabricated V_2O_5-doped glasses. With an increase in the concentration of V_2O_5 in the glass samples, the density values also showed an increment from 2.472 g/cm^3 to 2.522 g/cm^3. Comparatively, the density of Li_2O is 2.01 g/cm^3, while that of V_2O_5 is 3.36 g/cm^3. This observed rise in density in the synthesized samples as V_2O_5 content increases aligns with the theoretical expectations, confirming the experimental results. Additionally, as the mol% of V_2O_5 increased, the molar volume values of the glasses expanded from 62.59 cm^3/mol to 70.39 cm^3/mol. This suggests a proportional relationship between vanadium concentration and molar volume. This phenomenon may be attributed to the influence of polarizing power strength, which is a measure of the ratio of cation valence to its diameter (Al-Assiri, 2008).

Fig. 4 presents the 400–4000 cm^{-1} range of glass sample FTIR spectra. Visually, there was no noticeable difference between the FTIR spectra of the glass samples. Doping the glass matrix with up to 15 mol% V_2O_5 appears to have no effect on the IR peaks. It is obvious that adding up to 15 mol% V_2O_5 has no significant influence on the main characteristic groups, but it has a very tiny effect on the intensities of other IR bands (Kerkouri et al., 2011). The existence of hydroxyl groups is shown by the wide band present in all glasses about 3428 cm^{-1}, which corresponds to the essential stretching vibrations of O–H ions. The detected peaks, which are centered at 2851 cm^{-1} and 2918 cm^{-1}, are attributed to typical of hydrogen bonding in glass systems (Karunakaran et al., 2009). The peak around 1462 cm^{-1} may be caused by the B–O asymmetric stretching vibration of the BO_3 units (Kumar et al., 2019) (Singh et al., 2011). The band at 1054 cm^{-1} is due to BO_4 unit B–O–B bond stretching

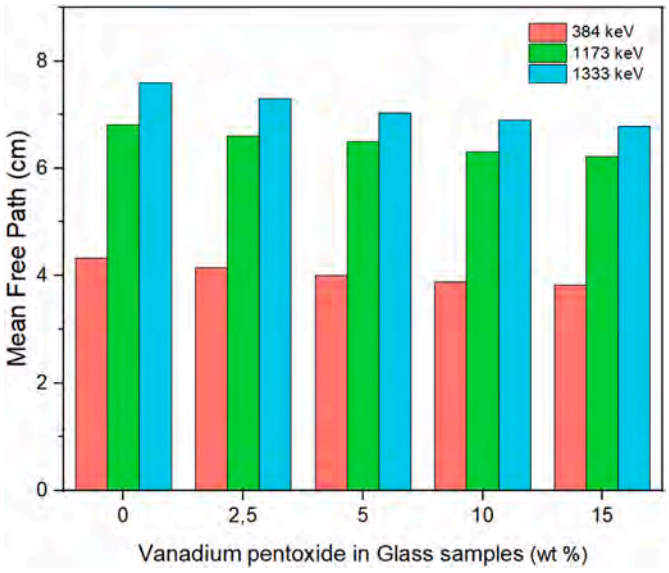

Fig. 13. Mean Free Path (MAC) values of V_2O_5 doped glasses.

vibrations (KILIÇ, 2020). Previous research has reported that the O–V angular vibration correspond to 545 cm^{-1} (KILIÇ, 2020) (Laila et al., 2013).

X-ray diffraction studies were performed between $10° \leq 2\theta \leq 90°$. Fig. 5 offers the X-ray diffraction graph of all Y-series glass systems. X-ray diffraction analysis indicated a knoll broad of about $2\theta \sim 20°–30°$, proving an amorphous structure for all Y-series glasses. The XRD graphs illustrate a fully amorphous glass structure with no sign of crystallization Y-series glasses produced. R. Divina et al. (Divina et al., 2020) reported similar XRD graph results for amorphous glass systems. In all Y series glass samples, the XRD curves are amorphous in nature of glass but different in density, indicating possible structural changes in XRD peak intensity (Nandi et al., 2022). For this reason, amorphous peaks may have partial intensity differences. The densities of the glasses produced in this study vary, and Y0 glass has the lowest density.

Fig. 6 present the DTA curves for different glasses samples. The DTA graphs for all curves indicate just one peak of exothermic. Table 2 summarizes produced of glass-transition temperature (T_g), crystallization temperature (T_c), and the peak of crystallization temperature (T_p) with the thermal parameters that can be determined by DTA analysis. Also, thermal stability has been calculated as formula $\Delta T = T_c - T_g$. The glass transition temperature of obtained glasses increases up to 10% V_2O_5. It may be explicable by the melting point of V_2O_5 (1750 °C) being higher than those of Li_2O (1438 °C), B_2O_3 (450 °C) and P_2O_5 (340 °C). All values of ΔT of Y series glasses were determined as 30 °C on average (Zhang et al., 2022). As a result, these glasses can be difficult to manufacture using traditional techniques. However, it is worth noting that the thermal stability results of these glasses are precision (El-Rehim et al., 2021) (Somaily et al., 2021). It is seen that Tg and Tc values increase by increasing the V_2O_5 concentration in Y series glasses. This may be because the inclusion of V_2O_5 into the matrix of P_2O_5 and B_2O_3 in glass samples causes structural distortion (Madhu et al., 2023b). In addition, V_2O_5 can increase T_g values by causing changes in the BO_3 and BO_4 groups (Dahiya et al., 2016). In addition, it is thought that the main reason for the difference in DTA results of Y series glasses is the binding of vanadium metal ions to the glass network and the strengthening of the system, which may cause the thermal resistance of the glasses to increase.

The Vickers microhardness of obtained $42.5P_2O_5–42.5B_2O_3–(15-x)Li_2O–xV_2O_5$ glasses are presented in Fig. 7. The hardness decreased as the V_2O_5content increased from 0% to 10%. It is seen that Y0 (5.66 GPa) and Y4 (4.99 GPa) glasses have the highest and lowest hardness values. However, no striking change was observed in the hardness values of Y series glasses with the addition of V_2O_3. As a result, it has been determined that the Y series glasses are reproducibility, and their hardness values are stable. Taha et al. It has been stated that as the CuO content increases in $P_2O_5–Li_2O–CuO$ glasses, the significant increase in hardness values is closely related to the density values of the glasses (Taha et al., 2021). It did not observe a change in the hardness results of the Y series glasses because the density values of the glasses are stable.

μ of V_2O_5 doped glasses are shown in Fig. 8. Accordingly, the μ value obtained with 384 keV energy gammas started around 0.2311±0.0116 cm^{-1} and gradually increased. This value has reached 0.2615±0.0131 cm^{-1} in 15% V_2O_5 doped glass. The R^2 value of these values was obtained as 0.900. These values decreased at 1173 keV gamma energy, but the values continued to increase according to the amount of V_2O_5. The R^2 value of these values was found to be 0.948. Finally, the μ values obtained with 1333 keV energy gammas were seen to be close to the previous μ values. The increasing trend in these μ values increased similarly to the increase in the amount of V_2O_5 at 1173 keV. The R^2 value here is determined as 0.886.

The Mass Attenuation Coefficient (MAC) results of V_2O_5 doped glasses are shown in Fig. 9. As can be seen from the MAC results in Fig. 9, the MAC values at 384 keV gamma energy were obtained as the highest at all V_2O_5 concentration values. The values, which were around 0.0934 $cm^2\ g^{-1}$ at this energy, decreased slightly at 1173 keV gamma energy and decreased to around 0.0593 $cm^2\ g^{-1}$. Finally, it was measured at around 0.0532 $cm^2\ g^{-1}$ at an energy of 1333 keV. Accordingly, as the gamma

Table 3
The shielding parameters of V_2O_5 doped Glass samples.

Concentration	μ (384 keV)	ρ	HVL	TVL	MFP	MAC $_{Exp.}$	MAC $_{XCOM}$	$\Delta_{XCOM-Exp.}$
0% V_2O_5	0.2311±0.0116	2.4720	2.9992	9.9631	4.3269	0.0934±0.0031	0.0944	0.98%
2.5% V_2O_5	0.2411±0.0121	2.4732	2.8742	9.5479	4.1466	0.0975±0.0011	0.0945	3.23%
5% V_2O_5	0.2499±0.0125	2.4828	2.7731	9.2120	4.0007	0.1006±0.0005	0.0945	6.52%
10% V_2O_5	0.2581±0.0129	2.4975	2.6852	8.9199	3.8739	0.1033±0.0018	0.0946	9.27%
15% V_2O_5	0.2615±0.0131	2.5215	2.6499	8.8029	3.8231	0.1037±0.0020	0.0947	9.56%
	μ (1173 keV)							
0% V_2O_5	0.1468±0.0073	2.4720	4.7212	15.6836	6.8113	0.0593±0.0013	0.0573	3.61%
2.5% V_2O_5	0.1514±0.0076	2.4732	4.5759	15.2009	6.6017	0.0612±0.0004	0.0573	6.83%
5% V_2O_5	0.1538±0.0077	2.4828	4.5063	14.9697	6.5013	0.0619±0.000008	0.0574	8.03%
10% V_2O_5	0.1585±0.0079	2.4975	4.3729	14.5264	6.3087	0.0634±0.0007	0.0574	10.61%
15% V_2O_5	0.1608±0.0080	2.5215	4.3088	14.3136	6.2163	0.0637±0.0009	0.0574	11.14%
	μ (1333 keV)							
0% V_2O_5	0.1315±0.0066	2.4720	5.2695	17.5048	7.6022	0.0532±0.0016	0.0537	0.91%
2.5% V_2O_5	0.1368±0.0068	2.4732	5.0647	16.8245	7.3068	0.0553±0.0006	0.0537	3.03%
5% V_2O_5	0.1422±0.0071	2.4828	4.8742	16.1918	7.0320	0.0572±0.0004	0.0537	6.60%
10% V_2O_5	0.1448±0.0072	2.4975	4.7839	15.8918	6.9017	0.0580±0.0008	0.0538	7.91%
15% V_2O_5	0.1475±0.0074	2.5215	4.6967	15.6020	6.7758	0.0585±0.0010	0.0538	8.81%

energy value increased, the MAC value decreased. As can be seen from here, the energy value and MAC value are inversely proportional.

The Mass Attenuation Coefficient (MAC) values comparison measured at 1173 keV and 1333 keV energies can be seen in Fig. 10. Accordingly, the obtained MAC values of 10%V_2O_5 doped glasses were higher than the other materials at 1173 keV and 1333 keV energies. For example, for 55P_2O_5–5Al_2O_3-20 Na_2O-(20-x)Fe_2O_3-xPbO glasses, the MAC value have been obtained as 0.0582 cm^2 g^{-1} at 1173 keV gamma energy and also it was found as 0.0545 cm^2 g^{-1} at 1333 keV (El-Taher et al., 2019). The MAC values have been found as 0.0565 cm^2 g^{-1} and 0.0528 cm^2 g^{-1} for barite concretes (Dogra et al., 2017) at same energies. For Barium–borate–fly ash glasses (Singh et al., 2008), the MAC values were obtained as 0.0552 cm^2 g^{-1} and 0.0523 cm^2 g^{-1}. To PbO–Li_2O–B_2O_3 glasses (Kumar, 2017), 0.0589 cm^2 g^{-1} and 0.0539 cm^2 g^{-1} MAC values have been obtained for 1173 keV and 1333 keV. The MAC values were found for Bi_2O_3–B_2O_3–Na_2WO_4 glasses (Dogra et al., 2017) as 0.0589 cm^2 g^{-1} and 0.0539 cm^2 g^{-1} MAC for same energies. The Barium–Bismuth–Borosilicate glasses (Bootjomchai et al., 2012) have 0.0565 cm^2 g^{-1} and 0.0515 g cm^{-2} MAC values for 1173 keV and 1333 keV energies, respectively. The MAC values of 10% V_2O_5 doped glasses were calculated theoretically by XCOM (Berger and Hubbell, 1987) by means of gammas with 1173 and 1333 keV energies. Accordingly, the MAC value found to be 0.05738 cm^2 g^{-1} at 1173 keV energy was calculated as 0.05376 cm^2 g^{-1} at 1333 keV. Finally, 0.3Bi_2O_3-0.7B_2O_3 glasses (Dogra et al., 2017) 0.0591 cm^2 g^{-1} and 0.0548 cm^2 g^{-1} for same energies. But the present study for 10% V_2O_5 doped glasses have 0.0634 ±0.0007 cm^2. g^{-1} value at 1173 keV and 0.0580±0.0008 cm^2. g^{-1} value at 1333 keV.

In Fig. 11, the Half Value Layer (HVL) values of V_2O_5 doped glasses are shown. This value, which indicates the amount of glass thickness that can transmit half of the gamma radiation that interacts with glass, was measured to be highest at 1333 keV energy. However, as the amount of V_2O_5 in the glass increased, this value decreased slightly. At 1173 keV energy, this HVL values decreased slightly, and at 384 keV energy, the required glass thickness and amount of glass was determined to be the lowest compared to the others and can be seen in Fig. 11.

TVL values, which express the material thickness required to reduce the amount of radiation interacting with the material to one-tenth, are given in Fig. 12. As in the previous figure where HVL values are shown, in Fig. 12 where TVL values are shown, the glass thickness that will reduce the gamma amount to one-tenth was obtained as the highest at 1333 keV. As the amount of V_2O_5 in the glass increases, these values decrease again. As the energy value decreases, the required glass thickness decreases. From here, the effect of the energy value on the thickness can be clearly seen. From here, the effect of the energy value on the thickness can be clearly seen.

MFP values expressing the path that gamma can take in the material are shown in Fig. 13. Here, similar to the previous HVL and TVL figures, MFP, which is the expression of the path that gammas can take in glass, is highest at 1333 keV energy. These values decrease as the amount of energy decreases. As can be understood from here, the energy of gamma directly affects the MFP. The experimentally measured and theoretically calculated shielding parameters have been given in Table 3.

4. Conclusion

In this study, some physical properties of 42.5P_2O_5–42.5B_2O_3–(15−x)Li_2O–xV_2O_5 (x = 0, 2.5, 5, 10 and 15) glasses and V_2O_5 dope to these glasses, potential radiation shielding properties were tried to be revealed. For this purpose, some analyzes revealing XRD, FTIR, DTA, micro-hardness and radiation shielding properties were performed.

Here, Linear Attenuation Coefficient (LAC) values were determined experimentally by means of gamma with energies of 384 keV, 1173 keV and 1333 keV via NaI(Tl) detector system (ORTEC® 905-4).

By experimentally determining the μ value, the Mass Attenuation Coefficients (MAC) of these glasses were also calculated and it was determined that the MAC values in each energy group increased as the amount of V_2O_5 in the glass increased. In addition, MAC values theoretically calculated with XCOM also showed a similar increase. However, the experimental MAC values we obtained gave better results than both the theoretical XCOM and many shielding material examples in the literature at 1173 and 1333 keV energy, as seen in Fig. 10.

Another shielding parameter, HVL, TVL and MFP, similarly decreased with the increase in the amount of V_2O_5 in the glass and revealed that these glasses can be used in radiation shielding.

CRediT authorship contribution statement

Yusuf Kavun: Writing – original draft, Supervision, Methodology, Investigation, Formal analysis, Data curation, Conceptualization. **Hasan Eskalen:** Validation, Methodology, Conceptualization, Visualization, Writing – review & editing. **Mustafa Kavgacı:** Visualization, Resources, Data curation, Investigation, Writing – review & editing. **Hakan Yaykaşlı:** Visualization, Resources, Data curation, Investigation, Writing – original draft. **Medeni Bahşi:** Investigation.

Declaration of competing interest

The authors declare that they have no known competing financial interests or personal relationships that could have appeared to influence the work reported in this paper.

Data availability

Data will be made available on request.

Acknowledgment

This study was supported by the Scientific Research Projects Coordination Unit of Kahramanmaraş Sütçü İmam University. Project numbers 2020/7–18 M, 2020/7–19 M, 2020/7–21 M and 2021/3-2 YLS.

References

Al-Assiri, M.S., 2008. Characterization and electrical properties of V2O5–CuO–P2O5 glasses. Phys. B Condens. Matter 403, 2684–2689. https://doi.org/10.1016/J.PHYSB.2008.01.049.

Alrowaili, Z.A., Ali, A.M., Al-Baradi, A.M., Al-Buriahi, M.S., Wahab, E.A.A., Shaaban, K.S., 2022. A significant role of MoO3 on the optical, thermal, and radiation shielding characteristics of B2O3–P2O5–Li2O glasses. Opt. Quant. Electron. 54, 1–19. https://doi.org/10.1007/S11082-021-03447-0/FIGURES/17.

Berger, M.J., Hubbell, J.H., 1987. XCOM: Photon Cross Sections on a Personal Computer. https://doi.org/10.2172/6016002.

Bootjomchai, C., Laopaiboon, J., Yenchai, C., Laopaiboon, R., 2012. Gamma-ray shielding and structural properties of barium–bismuth–borosilicate glasses. Radiat. Phys. Chem. 81, 785–790. https://doi.org/10.1016/J.RADPHYSCHEM.2012.01.049.

Dahiya, M.S., Khasa, S., Agarwal, A., 2016. Structural, optical and thermal properties of transition metal ions doped bismuth borate glasses. Eur. J. Glasses Sci. Technol. B Phys. Chem. Glasses 57, 45–52. https://doi.org/10.13036/17533562.57.2.023.

Divina, R., Sathiyapriya, G., Marimuthu, K., Askin, A., Sayyed, M.I., 2020. Structural, elastic, optical and γ-ray shielding behavior of Dy3+ ions doped heavy metal incorporated borate glasses. J. Non-Cryst. Solids 545, 120269. https://doi.org/10.1016/J.JNONCRYSOL.2020.120269.

Dogra, M., Singh, K.J., Kaur, K., Anand, V., Kaur, P., 2017. Gamma ray shielding and structural properties of Bi2O3-B2O3-Na2WO4 glass system. Univ. J. Phys. Appl. 11, 190–195. https://doi.org/10.13189/UJPA.2017.110508.

El-Rehim, A.F.A., Ali, A.M., Zahran, H.Y., Yahia, I.S., Shaaban, K.S., 2021. Spectroscopic, structural, thermal, and mechanical properties of B2O3-CeO2-PbO2 glasses. J. Inorg. Organomet. Polym. Mater. 31, 1774–1786. https://doi.org/10.1007/s10904-020-01799-w.

El-Taher, A., Ali, A.M., Saddeek, Y.B., Elsaman, R., Algarni, H., Shaaban, K.S., Amer, T.Z., 2019. Gamma ray shielding and structural properties of iron alkali alumino-phosphate glasses modified by PbO. Radiat. Phys. Chem. 165, 108403 https://doi.org/10.1016/J.RADPHYSCHEM.2019.108403.

Eskalen, H., Kavun, Y., Kerli, S., Eken, S., 2020. An investigation of radiation shielding properties of boron doped ZnO thin films. Opt. Mater. 105, 109871 https://doi.org/10.1016/j.optmat.2020.109871.

Fritsch, E., Babonneau, F., Sanchez, C., Calas, G., 1987. Vanadium incorporation in silica glasses. J. Non-Cryst. Solids 92, 282–294. https://doi.org/10.1016/S0022-3093(87)80046-7.

Gaddam, A., Allu, A.R., Fernandes, H.R., Stan, G.E., Negrila, C.C., Jamale, A.P., Méar, F. O., Montagne, L., Ferreira, J.M.F., 2021. Role of vanadium oxide on the lithium silicate glass structure and properties. J. Am. Ceram. Soc. 104, 2495–2505. https://doi.org/10.1111/JACE.17671.

Gomaa, H.M., Zahran, H.Y., Yahia, I.S., 2021. Influence of the structural matrix on the attenuation parameters of some iron-borophosphate glasses. J. Mater. Sci. Mater. Electron. 32, 21135–21154. https://doi.org/10.1007/S10854-021-06613-Y/FIGURES/11.

Hannachi, E., Sayyed, M.I., Slimani, Y., Elsafi, M., 2023. Structural, optical and radiation shielding peculiarities of strontium titanate ceramics mixed with tungsten nanowires: an experimental study. Opt. Mater. 135, 113317 https://doi.org/10.1016/J.OPTMAT.2022.113317.

Hlavae, J., 1983. Technology of Glass and Ceramics. Elsevier Science Pub., New York, NY, Golden, CO https://doi.org/10.2172/850486.

Holand, Wolfram, Beall, G.H., 2019. Glass-Ceramic Technology. John Wiley & Sons, Incorporated.

Jeager, R.G., 1975. Engineering Compendium on Radiation Shielding Vol. 2. Shielding Materials. Springer-Verlag New York Inc.

Karunakaran, R.T., Marimuthu, K., Surendra Babu, S., Arumugam, S., 2009. Structural, optical and thermal investigations on Dy3+ doped NaF–Li2O–B2O3 glasses. Phys. B Condens. Matter 404, 3995–4000. https://doi.org/10.1016/J.PHYSB.2009.07.160.

Kavun, Y., Eskalen, H., Kerli, S., Kavgaci, M., 2021. Fabrication and characterization of GdxFe2O3(100-x)/PVA (x=0, 5, 10, 20) composite films for radiation shielding. Appl. Radiat. Isot. 177, 109918 https://doi.org/10.1016/J.APRADISO.2021.109918.

Kavun, Y., Kerli, S., Eskalen, H., Kavgaci, M., 2022. Characterization and nuclear shielding performance of Sm doped In_2O_3 thin films. Radiat. Phys. Chem. 194, 110014 https://doi.org/10.1016/j.radphyschem.2022.110014.

Kerkouri, N., Haddad, M., Et-Tabirou, M., Chahine, A., Laânab, L., 2011. FTIR, Raman, EPR and optical absorption spectral studies on V2O5-doped cadmium phosphate glasses. Phys. B Condens. Matter 406, 3142–3148. https://doi.org/10.1016/J.PHYSB.2011.04.057.

Kiliç, G., 2020. Synthesis and optical, thermal, structural investigation of zinc-borate glasses containing V2O5. Adıyaman Üniversitesi Fen Bilimleri Dergisi 10, 307–325. https://doi.org/10.37094/ADYUJSCI.678938.

Knoll, G.F., Kraner, H.W., 1981. Radiation detection and measurement. Proc. IEEE. https://doi.org/10.1109/PROC.1981.12016.

Krane, K.S., 1991. Introductory Nuclear Physics. John Wiley & Sons.

Kumar, A., 2017. Gamma ray shielding properties of PbO-Li2O-B2O3 glasses. Radiat. Phys. Chem. 136, 50–53. https://doi.org/10.1016/J.RADPHYSCHEM.2017.03.023.

Kumar, A., Ali, A.M., Sayyed, M.I., Aşkın, A., Rashad, M., Algarni, H., 2019. Structural, optical, and gamma-ray-sensing characterization of (35 −x) PbO–10 MgO–10Na2O–5 Fe2O3–10 BaO–(30 −x) B2O3 glasses. Appl. Phys. Mater. Sci. Process 125, 1–9. https://doi.org/10.1007/S00339-019-2810-7/FIGURES/10.

Laila, S., Supardan, S.N., Yahya, A.K., 2013. Effect of ZnO addition and concurrent reduction of V2O5 on network formation and elastic properties of lead vanadate (55 −x) V2O5–45PbO–(x)ZnO glass system. J. Non-Cryst. Solids 367, 14–22. https://doi.org/10.1016/J.JNONCRYSOL.2013.02.007.

Madhu, A., El-Gawaad, N.S.A., Abdallah, S.A.O., Dadami, S.T., Hegde, B.G., Uthayakumar, T., Kumar, M.B.K., N, S., 2023a. Unravelling the conductivity behaviour of thermally stable Li2O– Bi2O3–B2O3–P2O5 glasses embedded with V2O5. Ceram. Int. 49, 28781–28793. https://doi.org/10.1016/J.CERAMINT.2023.06.138.

Madhu, A., El-Gawaad, N.S.A., Abdallah, S.A.O., Dadami, S.T., Hegde, B.G., Uthayakumar, T., Kumar, M.B.K., N, S., 2023b. Unravelling the conductivity behaviour of thermally stable Li2O– Bi2O3–B2O3–P2O5 glasses embedded with V2O5. Ceram. Int. 49, 28781–28793. https://doi.org/10.1016/J.CERAMINT.2023.06.138.

Mandal, A., Modak, N., Rakshit, A., Mondal, R., Das, A.S., Kabi, S., Mondal, S., Biswas, D., 2023. Structural modifications, optical response, and electrical conductivity mechanism of Bi2O3 doped in P2O5–V2O5–MoO3 nanocomposite glass systems. Mater. Chem. Phys. 298, 127466 https://doi.org/10.1016/J.MATCHEMPHYS.2023.127466.

Martin, James E., Tanır, G., 2013. Radyasyon Ve Radyasyondan Korunma Fiziği : Sağlık Fiziği Uygulamalı, 2020th ed. Palme Yayıncılık.

Masayuki Yamane, Y.A., 2004. Glasses for Photonics. Cambridge University Press.

Nandi, P., Dutta, D., Sanyal, B., Mishra, R., Goswami, M., Arya, A.K., 2022. Structure-property correlation study of gamma irradiated BaO-PbO-K2O-B2O3-SiO2 glasses. J. Non-Cryst. Solids 595, 121833. https://doi.org/10.1016/J.JNONCRYSOL.2022.121833.

Niksarlıoğlu, S., Akman, F., Pekdemir, M.E., Yalçın Kuzu, S., Kaçal, M.R., Yılmaz, M., 2023. An extensive investigation on gamma shielding properties of PLA/Gd2O3 nanocomposites. Radiat. Phys. Chem. 208, 110936 https://doi.org/10.1016/J.RADPHYSCHEM.2023.110936.

Rammah, Y.S., El-Agawany, F.I., Mahmoud, K.A., El-Mallawany, R., Ilik, E., Kilic, G., 2020a. FTIR, UV–Vis–NIR spectroscopy, and gamma rays shielding competence of novel ZnO-doped vanadium borophosphate glasses. J. Mater. Sci. Mater. Electron. 31, 9099–9113. https://doi.org/10.1007/S10854-020-03440-5/FIGURES/15.

Rammah, Y.S., Mahmoud, K.A., Sayyed, M.I., El-Agawany, F.I., El-Mallawany, R., 2020b. Novel vanadyl lead-phosphate glasses: P2O5–PbO–ZnONa2O–V2O5: synthesis, optical, physical and gamma photon attenuation properties. J. Non-Cryst. Solids 534, 119944. https://doi.org/10.1016/J.JNONCRYSOL.2020.119944.

Ravisankar, V., Ramesh, V., Gunasekaran, B. - al, Hussien, I.I., Mohsen, M., Hosny, H.M., Abd El Keriem, M.S., 2019. Study of the optical properties of V2O5-Li2O-P2O5 glass system. J. Phys. Conf. Ser. 1253, 012018 https://doi.org/10.1088/1742-6596/1253/1/012018.

Shen, N., Chen, S., Huang, R., Huang, J., Li, J., Shi, R., Niu, S., Amini, A., Cheng, C., 2021. Vanadium dioxide for thermochromic smart windows in ambient conditions. Mater. Today Energy 21, 100827. https://doi.org/10.1016/J.MTENER.2021.100827.

Singh, S., Kumar, A., Singh, D., Thind, K.S., Mudahar, G.S., 2008. Barium–borate–flyash glasses: as radiation shielding materials. Nucl. Instrum. Methods Phys. Res. B 266, 140–146. https://doi.org/10.1016/j.nimb.2007.10.018.

Singh, G.P., Kaur, P., Kaur, S., Singh, D.P., 2011. Role of V 2 O 5 In Structural Properties Of V 2 O 5-MnO 2-PbO-B 2 O 3 Glasses.

Somaily, H.H., Shaaban, K.S., Makhlouf, S.A., Algarni, H., Hegazy, H.H., Wahab, E.A.A., Shaaban, E.R., 2021. Comparative studies on polarizability, optical basicity and optical properties of lead borosilicate modified with titania. J. Inorg. Organomet. Polym. Mater. 31, 138–150. https://doi.org/10.1007/s10904-020-01650-2.

Susoy, G., 2020. Effect of TeO2 additions on nuclear radiation shielding behavior of Li2O–B2O3–P2O5–TeO2 glass-system. Ceram. Int. 46, 3844–3854. https://doi.org/10.1016/J.CERAMINT.2019.10.108.

Taha, M.A., Youness, R.A., El-Bassyouni, G.T., Azooz, M.A., 2021. FTIR spectral characterization, mechanical and electrical properties of P2O5-Li2O-CuO glass-ceramics. Silicon 13, 3075–3084. https://doi.org/10.1007/S12633-020-00661-5/METRICS.

Uosif, M.A.M., Mostafa, A.M.A., Issa, S.A.M., Tekin, H.O., Alrowaili, Z.A., Kilicoglu, O., 2020. Structural, mechanical and radiation shielding properties of newly developed tungsten lithium borate glasses: an experimental study. J. Non-Cryst. Solids 532, 119882. https://doi.org/10.1016/J.JNONCRYSOL.2019.119882.

Weyl, W.A., Pincus, A.G., Badger, A.E., 1939. Vanadium as a glass colorant. J. Am. Ceram. Soc. 22, 374–377. https://doi.org/10.1111/J.1151-2916.1939.TB19483.X.

Yaykaşlı, H., Eskalen, H., Kavun, Y., Gögebakan, M., 2022. Microstructural, thermal, and radiation shielding properties of Al50B25Mg25 alloy prepared by mechanical alloying. J. Mater. Sci. Mater. Electron. 33, 2350–2359. https://doi.org/10.1007/s10854-021-07434-9.

Zhang, X., Zhang, J., Zhou, C., Li, L., Qi, X., 2022. Optical properties and irradiation resistance of novel high-entropy oxide glasses La2O3-TiO2-Nb2O5-WO3-M2O3 (M=B/Ga/In). J. Rare Earths 3. https://doi.org/10.1016/j.jre.2022.04.003.

International Journal of Innovative Engineering Applications

Journal homepage: https://dergipark.org.tr/ijiea

SYNTHESIS OF FLUORESCENT CARBON QUANTUM DOTS WITH HYDROTHERMAL AND SOLVOTHERMAL METHOD APPLICATION FOR ANTICOUNTERFEITING AND ENCRYPTION

***Mustafa Kavgacı*[*1,2], *Hacı Veli Kalmış*[2], *Hasan Eskalen*[2,3]**

[1]*Kahramanmaraş Istiklal University, Elbistan Vocational School of Health Services, Department of Opticianry, Kahramanmaraş, Turkey*
[2]*Kahramanmaraş Sutcu Imam University, Material Science and Engineering Department, Kahramanmaraş, Turkey*
[3]*Kahramanmaraş Sutcu Imam University, Vocational School of Health Services, Department of Opticianry, Kahramanmaraş, Turkey*

Abstract

Original scientific paper

The objective of this work was to compare the optical performance of hydrothermally and solvothermal synthesized unique fluorescent carbon quantum dots (FCQDs) from organic material and use it as a fluorescent ink for one of the significant information encryption applications. The goji berry and sucrose were used as carbon sources for the experiment. FCQDs are obtained by simple hydrothermal and solvothermal methods using water, isopropanol and acetone as a solvent. The crystal structure and optical properties of the obtained carbon dots are investigated. All obtained FCQDs are amorphous phases. The maximum emission of the obtained FCQDs was found at 465 nm when excited at 386 nm. Among the carbon dot samples synthesized using three different solvents, the sample with the highest PL peak value was found in the sample synthesized with acetone solvent. The morphology of the carbon dot sample produced with acetone solution was examined by TEM and the average diameter of the carbon dots was calculated as 7.2 nm. The fluorescent ink potential of the synthesized FCQDs was compared and the best result found at the carbon dot that was synthesized from solvothermal methods with an acetone solution.

Keywords: *Carbon dots; fluorescence ink; goji berry; information encryption; XRD.*

SAHTECİLİKLE **MÜCADELE VE ŞİFRELEME UYGULAMASI İÇİN HİDROTERMAL VE SOLVOTERMAL YÖNTEM İLE FLUORESAN KARBON KUANTUM NOKTALARININ SENTEZİ**

Özet

Orijinal bilimsel makale

Bu çalışmanın amacı, organik bir malzemeden hidrotermal ve solvotermal yöntemle sentezlenen floresan karbon kuantum noktalarının (FCQDs) optik performanslarını karşılaştırmak ve bunları önemli bilgi şifreleme uygulamalarından biri için bir floresan mürekkep olarak kullanmaktır. Goji berry ve sakkaroz, çalışmada karbon kaynağı olarak kullanılmıştır. FCQD'ler, çözücü olarak su, izopropanol ve aseton kullanılarak hidrotermal ve solvotermal yöntemlerle elde edildi. Elde edilen karbon noktalarının kristal yapıları ve optiksel özellikleri araştırılmıştır. Elde edilen bütün FCQD'ler amorf fazdadır. FQCD'ler 386 nm'de uyarıldığında maksimum emisyonu 465 nm'de elde edilmiştir. Üç farklı çözücü kullanılarak sentezlenen karbon nokta örnekleri arasında en yüksek PL pik değeri aseton çözücü ile sentezlenen örnekte bulunmuştur. Aseton solüsyonu ile üretilen karbon nokta örneğinin morfolojisi TEM ile incelenmiş ve karbon noktaların ortalama çapı 7,2 nm olarak hesaplanmıştır. Sentezlenmiş FCQD'lerin floresan mürekkep olarak kullanılabilme potansiyeli karşılaştırılmış ve en iyi sonuç aseton çözücüsünde solvotermal yöntemle sentezlenen karbon noktaları için bulunmuştur.

Anahtar Kelimeler: *Karbon noktası; bilgi şifreleme; Floresans mürekkep; goji beri; XRD.*

1 Introduction

Today, with the growth in scientific studies, there has been a significant increase in the development of new materials with superior properties. Among them, nanostructured materials are known as one of the most researched and studied groups. Although there are various types of nanostructured materials, carbon based nanostructured materials have attracted specific interest. The newest members of carbon nanostructures are called CDs (carbon dots) or CQDs (carbon quantum dots). Carbon dots were found by chance in 2004 during the purification of carbon nanotubes and were subsequently obtained using laser ablation of graphite [1,2]. After this

* Corresponding author.
E-mail address: mkavgaci@gmail.com (M. Kavgacı)
Received: 20 September 2022; Received in revised form 19 January 2023; Accepted 02 March 2023
Cite this article: Kavgacı, M., Kalmış, H. V., Eskalen, H. (2023). Synthesis of Fluorescent Carbon Quantum Dots with Hydrothermal and Solvothermal Method Application for Anticounterfeiting and Encryption. International Journal of Innovative Engineering Applications, 7(1), 1-8. https://doi.org/10.46460/ijiea.1187470

discovery, the attractive, impressive, superior and unique properties of carbon dots were revealed and a new era began in terms of engineering science [3].

The size of the carbon dots is 10 nm or less. They have superior fluorescence properties in terms of their characteristics [4]. Carbon dots have superior fluorescence and optical properties as well as biocompatibility. Moreover, they have easy synthesis routes and pollution free precursors. Carbon dots, which have been studied by many scientists in recent years, have been found to have a number of exciting properties [5]. Carbon dots find a place in the theoretical and application areas in many fields such as science, engineering and health, thanks to their strength, optical, mechanical and electrical properties [6–8]. The most important feature of carbon dots is surface functionality that exhibits strong PL (photoluminescence), according to their size and excitation wavelength [6]. In addition to these properties, it is very valuable for its excellent biocompatibility, water solubility, low cost, low toxicity, easy synthesis, photostability and chemical stability. Considering these advantages, it has applications in many fields, such as bioimaging, sensor, solar cells, photocatalysis and drug delivery [9]. Carbon dots can be obtained from many natural sources such as food, waste and nutrients with the advantage of low cost [10].

Different organic sources have been used as carbon precursors for CD synthesis. For example, tangerine juice/onion Shell [11] turnip juice [12], rosemary leaves [13], pigeon manure [14], cowberry [15], blueberry [16], blackberry and raspberry [17]. The most known name of the goji berry is “wolfberry”. This name is based on the root "gou" meaning wolf [18]. The name goji is derived from several local words and was first coined by TBRI (Tanaduk Botanical Research Institute) researchers in 1973 [19]. Goji Berry, Latin name Lycium barbarum, is a shrub of the Solanaceae family from Southeast Asia and grows in China, Tibet and other parts of Asia. Its fruits are 1-2 cm long. It is bright red in color and elliptical in shape [20,21]. Goji Berry fruit is highly nutritious. It has become more popular in the last few years due to its recognition as a "superfood" among people.

Due to its nutritional value, it has become more preferred by people today. The fruit contains sugar [19]. Goji berry has several important biological functions, such as boosting immunity, anti-aging, anti-tumor and antioxidant [18]. Digital security is crucial in the information era because counterfeiting not only results in significant economic losses but also has negative effects on people's physical and mental health. Luminescent inks have drawn a lot of interest among the many anti-counterfeiting substances due to their numerous uses in information coding, information storage, and information security. A significant barrier still exists in the production of high anti-counterfeiting strategies and aqueous luminous anti-counterfeiting nanomaterials [22–25].

Sucrose was also added to the goji berry to strengthen the PL peaks of the synthesized carbon spots, based on a related work in the literature [26,27]. Precursors, synthesis procedures, particle size, fundamental PL characteristics, applications, and findings from this work are summarized in Table 1. In this study, goji berry (Lycium barbarum) was used as a natural carbon source. CDs were synthesized by hydrothermal and solvothermal methods. While synthesizing carbon dots, acetone, ultrapure water and isopropyl alcohol were used as solvents, and carbon dot samples synthesized using this solvent were compared. The structural properties of carbon dots were researched by XRD analysis. In addition, the optical properties of the synthesized materials were investigated in UV-Vis spectroscopy. The photoluminescence properties of the obtained nanoparticles with carbon dots were researched by photoluminescence spectrometry. FTIR spectrometer was used to analyze its chemical structure.

Table 1. Carbon source, size, PL properties and application examples used in preparing carbon dots.

Carbon precursors	Synthesis methods	Size (nm)	PL features	Application	Reference
Tea residue/ Choline chloride/ Urea	Hydrothermal	< 10	Ex: 330 nm Em: 410 nm	Sensing	[28]
Chia seed	Hydrothermal	5.4	Ex: 310 nm Em: 415 nm	Cell imaging	[29]
Aconitic acid/ PEI	Thermal carbonization	11.12	Ex: 440 nm Em: 485 nm	Sensing	[30]
Citric Acid/ m-PD	Hydrothermal	3.03 to 3.73	Ex: 320 nm Em: 466 nm	Information encryption, Anti-Counterfeiting	[31]
Laurus nobilis leaves	Hydrothermal	< 10	Ex: 344 nm Em: 425 nm	Fluorescent ink	[32]
Waste corn husk	Hydrothermal	5.39	Ex: 342 nm Em: 428 nm	Composite material	[33]
Rosemary leaves	Hydrothermal	16.13	Ex: 332 nm Em: 422 nm	Food storage, fingerprint detection, antibacterial activity	[13]
Citric Acid/ PEI	Microwave-assisted	12	Ex: 354 nm Em: 442 nm	TNT determination	[34]
Citric Acid	Microwave-assisted	3		Fish gelatin films	[35]
Cowberry	Hydrothermal		Ex: 350 nm Em ~ 440 nm	Composite material	[15]
Blueberry	Facile liquid N_2 treatment method		Ex: 340 nm Em: 450 nm	Sensing	[16]
Goji berry	Hydrothermal Solvothermal	7.2	Ex: 386 nm Em: 465 nm	Information encryption, Anti-Counterfeiting	This work

2 Materials and Methods

2.1 Material

Goji berry was obtained in the personal garden of the author Hacı Veli Kalmış. Solvents purchased from standard manufacturers were used in the experiments. The ultrapure water used in the experiments was supplied from the KSÜ ÜSKİM unit. All materials were used in their current form without purification.

2.2 Preparation of CD Nanoparticles

Goji berry was chosen as a natural carbon source. Goji beryy was cleaned by washing with tap water. It was then washed with pure water. Then, the goji berry was kept in an oven at 60°C for 96 hours to be dried. The dried goji berry was sieved after grinding. 1.25 g of goji berry powder and 1.25 g of sucrose were mixed in 150 ml of solvent in an ultrasonic treatment. Ultrapure water, acetone and isopropyl alcohol were used as solvents. The carbon dots were synthesized using three different solvents. The homogenized mixture was transferred to a teflon box. The Teflon box was then placed in an autoclave made of stainless steel. After being placed in the autoclave oven, it was subjected to hydrothermal and solvothermal treatment at 175°C for 8 hours. At the end of the process, the autoclave was taken from the oven to cool itself to room temperature. The resulting solution was filtered. It was centrifuged and dried. It was stored at 4 °C for experiments. The final concentration of the carbon dots in solution for measurements was 0.25 mg mL^{-1}. The schematic representation of the experimental setup is given in Figure 1. While synthesizing carbon dots, acetone, ultrapure water and isopropyl alcohol were used as solvents, and carbon dot samples synthesized using this solvent were named as GCDa, GCDw and GCDi, respectively.

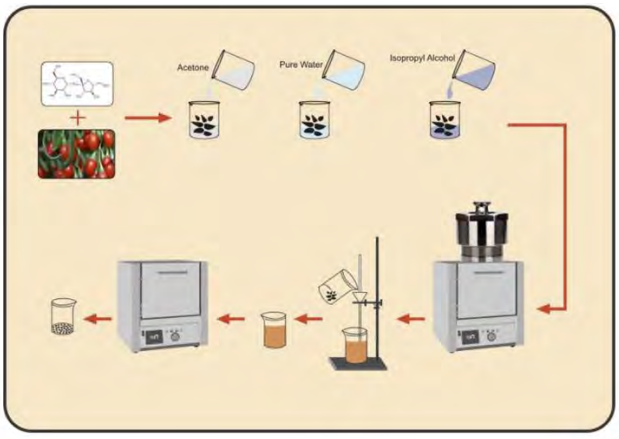

Figure 1. Symbolic representation of obtaining carbon dots from Goji berry.

2.3 Characterization

Structural characterization of the synthesized Carbon dots samples was examined by XRD (X-ray diffraction). Philips X'Pert PRO XRD device with Cu Kα radiation (λ = 0,154056 nm, tuned at 40 kV and 30 mA) was used to detect the XRD pattern. The optical properties of the synthesized carbon dot samples were obtained by UV-Visible Spectrophotometer (Shimadzu UV 1800) at room temperature. FTIR Spectroscopy: Measured with a Perkin Elmer Spectrum 400 instrument in the 4000–450 cm^{-1} range. The PL spectra of the CD samples were scanned with the Varian Cary Eclipse spectrometer.

3 Results and Discussion

The XRD pattern showing the crystal structures of the carbon dots synthesized from Goji berry is presented in Figure 2. CDs synthesized in the XRD plot appear to have flat amorphous peaks similar to the structure of 2θ=23° graphene. Pure graphite has a significant peak at 2θ=26.42° that corresponds to the (002) plane in the X-ray pattern, while GO has two distinctive peaks at 2θ=11° and 2θ=42° that correlate to the (001) and (100) planes [36]. For multi-walled carbon nanotubes, two diffraction peaks with centers at 26° and 45° are often seen. These peaks are designated as (002) and (001) planes [37]. Generally, amorphous carbons with graphitic domains are indicative of carbonaceous materials (sp2 domains). The two broad Bragg peaks at 22.0 and 43.7 were indexed to the graphite hexagonal structure's (002) and (100) planes, respectively [38]. This broad and amorphous peak has also been detected in XRD plots of CDs in many studies [32,39,40].

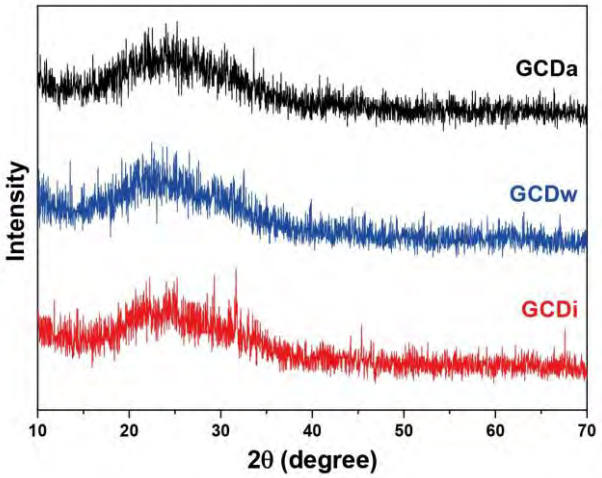

Figure 2 XRD pattern of CDs

UV-Visible spectroscopy can be used to observe what changes nanoparticles undergo as time passes. Carbon nanoparticles can be characterized by UV-Visible spectroscopy [41]. Carbon dots synthesized from Goji berry were examined by UV-Visible spectroscopy. The UV-Visible absorption graph is given in Figure 3. A sharp absorption peak similar to a π-π* transition was seen in the UV–Visible spectrum at 282 nm [42]. Figure 4a illustrates PL spectra of the obtained carbon dots in different solvents and when the samples are excited at 386 nm wavelength, they exhibit maximum emission at 465 nm (Figure 4b). The maximum PL intensity was found in the carbon dots sample which is dissolved in acetone. Photoluminescence spectra of carbon dot sample (GCDa) dissolved in water were investigated using PL spectrometry by varying the wavelength between 400-600 nm (Figure 5). It was observed that the synthesized CD samples gave excitation-induced emission. When the

excitation wavelength was changed from 386 nm to 456 nm with 5 nm intervals, the emission peak was redshifted from 465 nm to 508 nm. The observed redshift in the emission spectrum indicates the possibility of tunability of the PL emission color. Depending on the increase in the excitation wavelength, the intensity of the fluorescence peak decreases and exhibits attenuation [33]. This result is due to electron and hole recombination produced on the surface of CDs. The redshift observed with the difference in excitation wavelengths can be attributed to the difference in the surface sizes of the CDs [42].

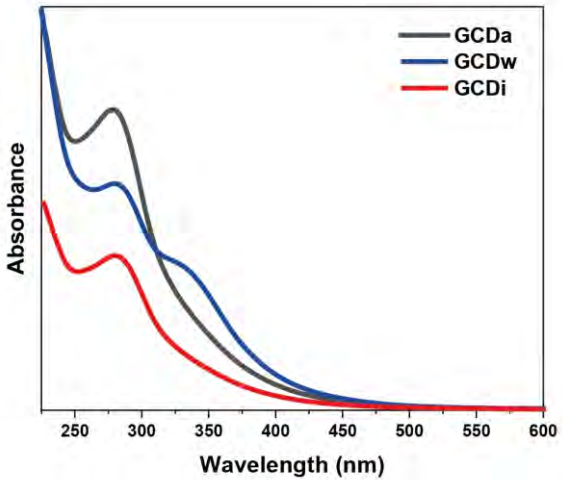

Figure 3. UV-Vis spectrum of synthesized carbon dots from Goji berry.

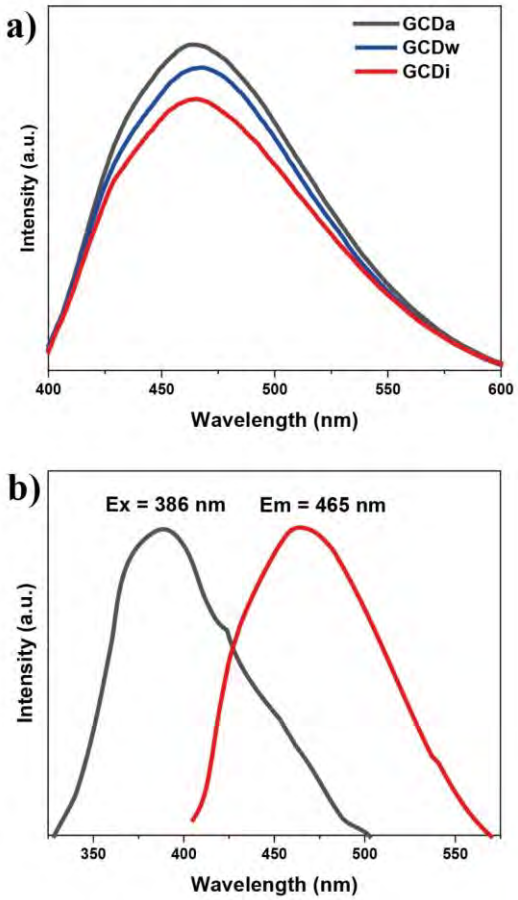

Figure 4. a) PL spectra of CDs synthesized in different solvents b) Excitation and emission spectrum of product GCDa.

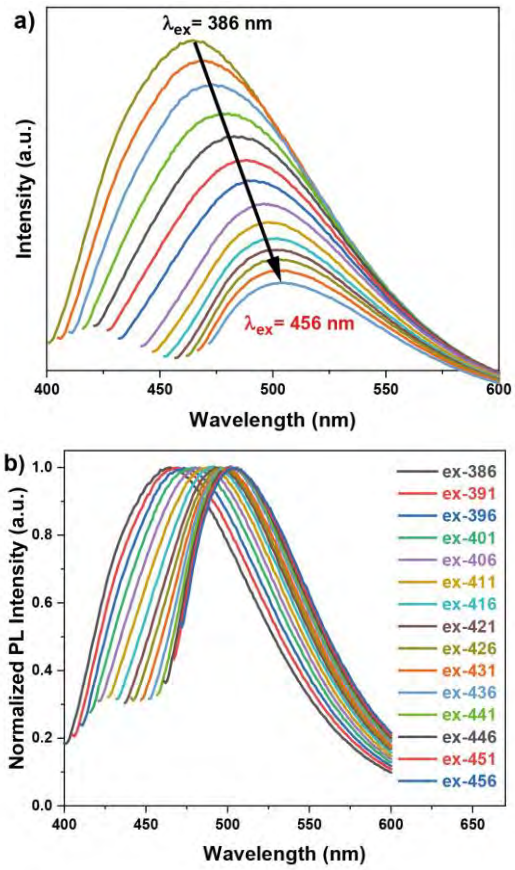

Figure 5. a) Excitation dependent PL spectra of GCDa, b) after normalization.

FTIR measurements were taken in the 450-4000 cm^{-1} range to examine the chemical structure of the synthesized samples. FTIR results are presented in Figure 6. The broad peak seen at 3324 cm^{-1} is attributable to O–H or N–H stretching vibrations [43]. The absorbance peak of the samples at 2924 cm^{-1} and 2846 cm^{-1} coincides with the C–H bonds [44–46]. The 1706–1605 cm^{-1} double peak can be attributed to the stretching vibrations of the C–N and C–O bonds, respectively [44]. The C-N bonds observed in the FTIR analysis may be due to the amino groups in the proteins found in the structure of the goji berry [47]. The peaks of stretching vibration of the C–C, C–N, and C–O groups can be seen at 1372 cm^{-1}, 1200 cm^{-1} and 1100 cm^{-1}, respectively [48].

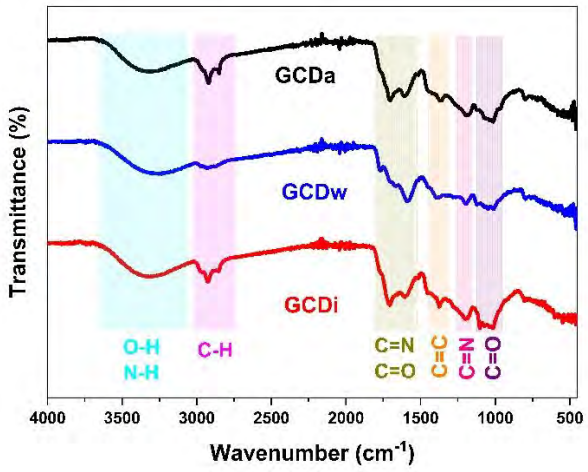

Figure 6. FT-IR spectrum of the CDs.

The morphological properties of synthesized CDs were studied, and Figure 7 depicts the form and size distribution of the carbon dots sample produced in acetone solution. GCDa sampe have homogeneous size and distribution, as observed in the TEM picture. The average diameter of the studied carbon dots was calculated to be 7.2 nm.

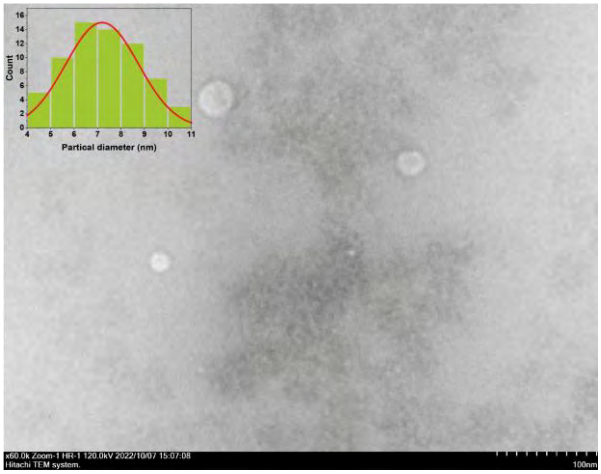

Figure 7. TEM image of GCDa sample.

Carbon dot samples were dissolved in distilled water. Then the carbon dots were centrifuged to separate large particles. The fluorescent abilities of the CDs obtained in Figure 8 are observed at a distance of 10-15 cm under UV light (365 nm). Under UV light, GCDa and GCDw carbon dot samples glowed turquoise. When the synthesized samples were compared, it was observed that the fluorescence irradiation was ordered as PGDa > PGDw > PGDi [14].

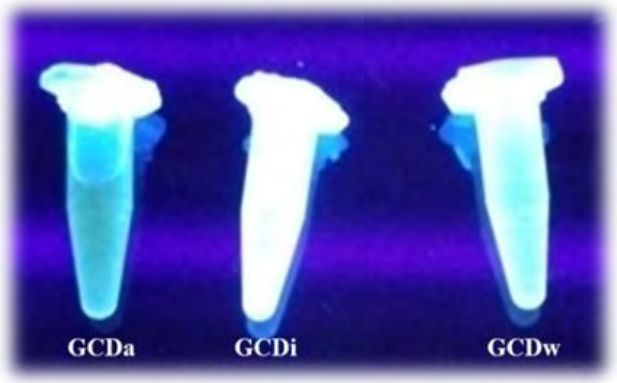

Figure 8. Image of GCDa, GCDi and GCDw samples under UV light, respectively.

CQDs are materials with serious potential as fluorescent inks that can be used in various applications due to their non-toxicity, fluorescent stability and similar properties. Fluorescent inks obtained using CQDs are environmentally friendly and permanent. Additionally, such fluorescent inks can be used in anti-fraud and encryption applications [14]. Interestingly, some luminescent materials with exceptional invisible transparency capabilities may be used spontaneously as luminescent inks (Figure 8). A brush and commercial papers without any background luminescence were used. The similar pattern may be readily obtained, as shown in Figure 9, by utilizing obtained GCDa, GCDw, and GCDi labeled carbon dots as luminous inks. This pattern was invisible in the daylight but was immediately visible under UV light. The best outcome for the GCDa carbon dot sample was produced, and it may be utilized as direct anti-counterfeiting luminescent inks. Utilizing carbon dots with a higher PL peak intensity can help luminescent inks' anti-counterfeiting capabilities.

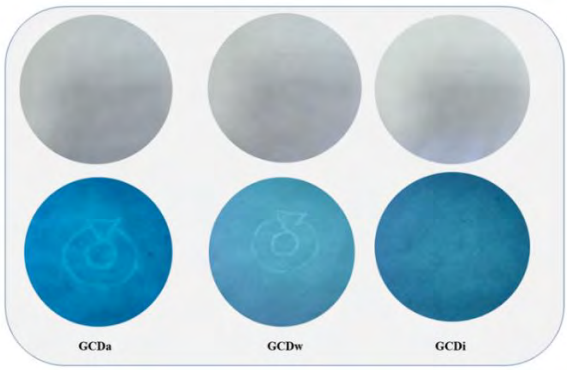

Figure 9. Images drawn with fluorescent ink created from CQDs in daylight and under UV light (365 nm).

4 Conclusion

Fluorescent carbon dots were synthesized from Goji berry simply, non-toxic, environmentally friendly and cost-effective. CDs were obtained by the hydrothermal and solvothermal methods using Goji berry and sucrose as a precursors and water, isopropanol and acetone as a solvent. The crystal structures of carbon quantum dots synthesized using different solvents were investigated by XRD and the crystal structure of obtained carbon dots consists of amorphous phases. The obtained peaks in the UV spectrum of carbon dots are attributed to π–π* electronic transitions. As a result of the excitation of the samples at a wavelength of 386 nm, it was observed that they exhibited maximum emission at a wavelength of 465 nm. By increasing the excitation wavelength, a redshift of the emission peak was detected. The sample with the highest PL peak value among the carbon dot samples generated using three different solvents was discovered in the sample synthesized using acetone solvent. TEM was used to study the morphology of the carbon dot sample synthesized with acetone solution, and the average diameter of the carbon dots was determined to be 7.2 nm. Obtained GCDa, GCDw, and GCDi carbon dots was utilized as luminous inks. This pattern was invisible in the daylight but was immediately visible under UV light. The best outcome for the GCDa carbon dot sample was produced, and it may be utilized as direct anti-counterfeiting luminescent inks.

Acknowledgements

This study was supported by the Scientific Research Projects Coordination Unit of Kahramanmaraş Sütçü İmam University. Project number 2021/1-7 YLS.

Declaration

Ethics committee approval is not required.

References

[1] Xu, X., Ray, R., Gu, Y., Ploehn, H.J., Gearheart, L., Raker, K., & Scrivens, W.A. (2004). Electrophoretic analysis and purification of fluorescent single-walled carbon nanotube fragments. *Journal of the American Chemical Society*, 126(40), 12736–12737.

[2] Sun, Y.P., Zhou, B., Lin, Y., Wang, W., Fernando, K.A.S., Pathak, P., et al. (2006). Quantum-sized carbon dots for bright and colorful photoluminescence. *Journal of the American Chemical Society*, 128(24), 7756–7757.

[3] Bhartiya, P., Singh, A., Kumar, H., Jain, T., Singh, B.K., & Dutta, P.K. (2016). Carbon dots: Chemistry, properties and applications. *Journal of the Indian Chemical Society*, 93(7), 759–766.

[4] Zhang, J. & Yu, S.H. (2016). Carbon dots: large-scale synthesis, sensing and bioimaging. *Materials Today*, 19 (7), 382–393.

[5] Wang, T., Wang, A., Wang, R., Liu, Z., Sun, Y., Shan, G., Chen, Y., & Liu.Y. (2019). Carbon dots with molecular fluorescence and their application as a "turn-off" fluorescent probe for ferricyanide detection. *Scientific Reports*, 9(1), 1–9.

[6] Wang, Y. & Hu, A. (2014). Carbon quantum dots: Synthesis, properties and applications. *Journal of Materials Chemistry C*, 2(34), 6921–6939.

[7] Xu, Y., Liu, J., Gao, C., & Wang, E. (2014). Applications of carbon quantum dots in electrochemiluminescence: A mini review. *Electrochemistry Communications*, 48, 151–154.

[8] Ibrayev, N., Dzhanabekova, R., Seliverstova, E., & Amanzholova, G. (2022). Optical properties of N- and S-doped carbon dots based on citric acid and L-cysteine. *Fullerenes, Nanotubes and Carbon Nanostructures,* 30(1), 22–26.

[9] Dinc, S. & Kara, M. (2018). Synthesis and Applications of Carbon Dots from Food and Natural Products. *Journal of Apitherapy and Nature/Apiterapi ve Doğa Dergisi,* 1(1), 33–37.

[10] Bag, P., Maurya, R. K., Dadwal, A., Sarkar, M., Chawla, P. A., Narang, R. K., & Kumar, B. (2021). Recent Development in Synthesis of Carbon Dots from Natural Resources and Their Applications in Biomedicine and Multi-Sensing Platform. *ChemistrySelect*, 6(11), 2774–2789.

[11] Başkaya, S.K. & Çeşme, M. (2021). Synthesis of N-Doped Carbon Quantum Dots by Hydrothermal Synthesis Method and Investigation of Optical Properties. *Türk Doğa ve Fen Dergisi*, 10(2), 206–211.

[12] Eskalen, H. & Çeşme, M. (2021). Carbon Dots from Turnip Juice: Synthesis, Characterization and Investigation of pH-Dependent Optical Properties. *Bilecik Seyh Edebali University Journal of Science,* 8(2), 924–930.

[13] Eskalen, H., Çeşme, M., Kerli, S., & Özğan, Ş. (2021). Green synthesis of water-soluble fluorescent carbon dots from rosemary leaves: Applications in food storage capacity, fingerprint detection, and antibacterial activity. *Journal of Chemical Research,* 45(5-6), 428–435.

[14] Başkaya, K., Tahta, B., Uruş, S., Eskalen, H., Çeşme, M., & Özğan, Ş. (2022). Multifunctional B, N, P, and S-doped fluorescent carbon quantum dot synthesis from pigeon manure: highly effective Hg (II) sensor and fluorescent ink properties. *Biomass Conversion and Biorefinery,* 1, 1–15.

[15] Kapitonov, A. N., Egorova, M. N., Tomskaya, A. E., Smagulova, S. A., & Alekseev, A. A. (2018). Hydrothermal synthesis of carbon dots and their luminescence. *AIP Conference Proceedings*, 2041(1), 030003.

[16] Aslandaş, A. M., Balci, N., Arik, M., Şakiroglu, H., Onganer, Y., & Meral, K. (2015). Liquid nitrogen-assisted synthesis of fluorescent carbon dots from Blueberry and their performance in Fe^{3+} detection. *Applied Surface Science*, 356, 747–752.

[17] Yang, Z., Xu, M., Wang, T., Wei, H., & Zhang, Y. (2015). Method for hydro-thermal synthesis of carbon quantum dots based on fruits, CN105366659A.

[18] Potterat, O. (2010). Goji (Lycium barbarum and L. chinense): Phytochemistry, pharmacology and safety in the perspective of traditional uses and recent popularity. *Planta Medica,* 76(1), 7–19.

[19] Amagase, H. & Farnsworth, N. R. (2011). A review of botanical characteristics, phytochemistry, clinical relevance in efficacy and safety of Lycium barbarum fruit (Goji). *Food Research International*, 44(7), 1702–1717.

[20] Donno, D., Beccaro, G. L., Mellano, M. G., Cerutti, A. K., & Bounous, G. (2015). Goji berry fruit (Lycium spp.): Antioxidant compound fingerprint and bioactivity evaluation. *Journal of Functional Foods*, 18, 1070–1085.

[21] Montesano, D., Cossignani, L., Giua, L., Urbani, E., Simonetti, M. S., & Blasi, F. (2016). A Simple HPLC-ELSD Method for Sugar Analysis in Goji Berry. *Journal of Chemistry*, 1-5.

[22] Wang, T., Yang, J., Li, H., & Wang, Y. (2019). Aminoclay decorated with lanthanide complexes and carbon dots: Tunable emission and information encryption. *Journal of Rare Earths*, 37(9), 995–1001.

[23] Li, J., Xia, D., Gao, M., Jiang, L., Zhao, S., & Li, G. (2021). Invisible luminescent inks and luminescent films based on lanthanides for anti-counterfeiting. *Inorganica Chimica Acta,* 526, 120541.

[24] Siddique, A.B., Singh, V. P., Chatterjee, S., Pramanik, A. K., & Ray, M. (2018). Facile synthesis and versatile applications of amorphous carbon dot. *Materials Today: Proceedings,* 5(3), 10077–10083.

[25] Kumar, P., Dwivedi, J., & Gupta, B. K. (2014), Highly luminescent dual mode rare-earth nanorod assisted multi-stage excitable security ink for anti-counterfeiting applications. *Journal of Materials Chemistry C*, 2(48), 10468–10475.

[26] Li, Q., Du, H., Li, J., Deng, J., Wang, R., & Chen, Y. (2022). Sulfur-rich carbon quantum dots based on Alternanthera philoxeroides and thiourea for the detection of tartrazine. *Journal of Materials Science: Materials in Electronics,* 33(16), 12808–12818.

[27] Krishnaiah, P., Atchudan, R., Perumal, S., Salama, E. S., Lee, Y. R., & Jeon, B. H. (2022). Utilization of waste biomass of Poa pratensis for green synthesis of n-doped carbon dots and its application in detection of Mn^{2+} and Fe^{3+}. *Chemosphere*, 286, 131764.

[28] Huang, Z. Y., Wu, W. Z., Li, Z. X., Wu, Y., Wu, C.-B., Gao, J., Guo, J., Chen, Y., Hu, Y., & Huang, C. (2022). Solvothermal production of tea residue derived carbon dots by the pretreatment of choline chloride/urea and its application for cadmium detection. *Industrial Crops and Products*, 184, 115085.

[29] Marouzi, S., Darroudi, M., Hekmat, A., Sadri, K., & Oskuee, R. K. (2021). One-pot hydrothermal synthesis of carbon quantum dots from Salvia hispanica L. seeds and investigation of their biodistribution, and cytotoxicity effects. *Journal of Environmental Chemical Engineering*, 9(4), 105461.

[30] Ge, L., Hu, G., Zhao, F., Wang, X., Ma, Z., & Liu, R. (2021). Carbon dots prepared by thermal reactions and selective detections of copper and mercury ions in visible spectrum. *Applied Physics A: Materials Science and Processing,* 127(5), 388.

[31] Wang, H. Y., Zhou, L., Yu, H. M., Tang, X. D., Xing, C., Nie, G., Akafzade, H., Wang, S. Y., & Chen, W. (2022). Exploration of Room-Temperature Phosphorescence and New Mechanism on Carbon Dots in a Polyacrylamide Platform and their Applications for Anti-Counterfeiting and Information Encryption. *Advanced Optical Materials,* 2200678, 1–11.

[32] Eskalen, H., Kavgacı, M., Kayış, A., & Özğan, Ş. (2021). One-Pot Synthesis of Carbon Quantum Dots and Their Application As a Fluorescent Inks. *Eskişehir Technical University Journal of Science and Technology A - Applied Sciences and Engineering*, 22(4), 366–377.

[33] Eskalen, H., Yaykaşlı, H., Kavgacı, M., & Kayış, A. (2022). Investigating the PVA/TiO_2/CDs polymer nanocomposites: effect of carbon dots for photocatalytic degradation of Rhodamine B. *Journal of Materials Science: Materials in Electronics,* 33(7), 4643–4658.

[34] Şen, F. B., Beğiç, N., Bener, M., & Apak, R. (2022). Fluorescence turn-off sensing of TNT by polyethylenimine capped carbon quantum dots. *Spectrochimica Acta Part A: Molecular and Biomolecular Spectroscopy*, 271, 120884.

[35] Kilic, B., Dogan, V., Kilic, V., & Kahyaoglu, L. N. (2022). Colorimetric food spoilage monitoring with carbon dot and UV light reinforced fish gelatin films using a smartphone application. *International Journal of Biological Macromolecules,* 209, 1562–1572.

[36] Uruş, S., Çaylar, M., Eskalen, H., & Özgan, Ş. (2022). Synthesis of GO@Fe_3O_4@TiO_2 type organic–inorganic nanohybrid material: Investigation of the effect of nanohybrid doped liquid crystal E7 and the photocatalytic degradation of ciprofloxacin. *Journal of Materials Science: Materials in Electronics,* 33(7), 4314–4329.

[37] Eskalen, H., Uruş, S., & Özgan, Ş. (2021). Microwave-Assisted Synthesis of Mushrooms Like MWCNT/SiO_2@ZnO Nanocomposite: Influence on Nematic Liquid Crystal E7 and Highly Effective Photocatalytic Activity in Degradation of Methyl Blue. *Journal of Inorganic and Organometallic Polymers and Materials,* 31(2), 763–775.

[38] Marino, C., Cabanero, J., Povia, M., & Villevieille, C. (2018). Biowaste Lignin-Based Carbonaceous Materials as Anodes for Na-Ion Batteries. *Journal of The Electrochemical Society,* 165(7), 1400–1408.

[39] Rai, S., Singh, B. K., Bhartiya, P., Singh, A., Kumar, H., Dutta, P. K., & Mehrotra, G. K. (2017). Lignin derived reduced fluorescence carbon dots with theranostic approaches: Nano-drug-carrier and bioimaging. *Journal of Luminescence*, 190, 492–503.

[40] Das, P., Bhattacharyya, S. K., Banerji, P., & Das, N. C. (2021). Acoustic cavitation assisted synthesis and characterization of photoluminescent carbon quantum dots for biological applications and their future prospective. *Nano-Structures and Nano-Objects*, 25, 100641.

[41] Swapna, M. S. & Sankararaman, S. (2017). Carbon Nanonecklaces with Carbon Nanotubes and Carbon Dots. *International Journal of Materials Science*, 12(4), 541–548.

[42] Sivanandhan, M., Parasuraman, A., Surya, C., Lakshminarayanan, K., Krishnakumar, B., Mani, D., & Ahn, Y. H. (2022). Facile approach for green synthesis of fluorescent carbon dots from Manihot esculenta and their potential applications as sensor and bio-imaging agents. *Inorganic Chemistry Communications*, 137, 109219.

[43] Xu, D., Lei, F., Chen, H., Yin, L., Shi, Y., & Xie, J. (2019). One-step hydrothermal synthesis and optical properties of self-quenching-resistant carbon dots towards fluorescent ink and as nanosensors for Fe^{3+} detection. *RSC Advances,* 9(15), 8290–8299.

[44] Taspika, M., Permatasari, F. A., Nuryadin, B. W., Mayangsari, T. R., Aimon, A. H., & Iskandar, F. (2019). Simultaneous ultraviolet and first near-infrared window absorption of luminescent carbon dots/PVA composite film. *RSC Advances,* 9(13), 7375–7381.

[45] Kayış, A., Kavgacı, M., Yaykaşlı, H., Kerli, S., & Eskalen, H. (2021). Investigation of Structural, Morphological, Mechanical, Thermal and Optical Properties of PVA-ZnO Nanocomposites. *Glass Physics and Chemistry*, 47(5), 451–461.

[46] Pandiyan, S., Arumugam, L., Srirengan, S. P., Pitchan, R., Sevugan, P., Kannan, K., Pitchan, G., Hegde, T. A., & Gandhirajan, V. (2020), Biocompatible Carbon Quantum Dots Derived from Sugarcane Industrial Wastes for Effective Nonlinear Optical Behavior and Antimicrobial Activity Applications. *ACS Omega,* 5(47), 30363–30372.

[47] Gezici, S. (2022). Molecular Mechanisms, Biological and Pharmacological Properties of Goji Berries as a Potential Natural Antioxidant Medicine. *Mersin Üniversitesi Tıp Fakültesi Lokman Hekim Tıp Tarihi ve Folklorik Tıp Dergisi,* 12(1), 67–76.

[48] Beker, S. A., Truskewycz, A., Cole, I., & Ball, A. S. (2020). Green synthesis of: Opuntia-derived carbon nanodots for the catalytic decolourization of cationic dyes. *New Journal of Chemistry,* 44(46), 20001–20012.

J Mater Sci: Mater Electron (2023) 34:1229

Morphology, structure and optical properties of PVA nanocomposites reinforced with bismuth oxide nanoparticles and carbon quantum dots

Mustafa Kavgacı[1,3] and Hasan Eskalen[2,3,*]

[1] Department of Opticianry, Elbistan Vocational School of Health Services, Kahramanmaraş Istiklal University, Kahramanmaraş, Turkey
[2] Department of Opticianry, Vocational School of Health Services, Kahramanmaraş Sütçü İmam University, Kahramanmaraş, Turkey
[3] Department of Material Science and Engineering, Graduate School of Natural and Applied Sciences, Kahramanmaraş Sütçü İmam University, Kahramanmaraş, Turkey

Received: 3 February 2023
Accepted: 12 May 2023
Published online: 27 May 2023

ABSTRACT

In this study, bismuth oxide (Bi_2O_3) and carbon quantum dots (CQDs) were synthesized, structural, morphological and optical properties of the obtained samples were investigated. Novel polymer nanocomposite films were obtained by using the casting method with introducing the produced Bi_2O_3 and CQDs nanoparticles to polyvinyl alcohol (PVA) at different rates. The structural features of the resulting polymer nanocomposite films were investigated by X-ray diffraction technique. The optical parameters of composite films were investigated using the absorption and transmittance spectra. The increase in the amount of Bi_2O_3 additives in the composite PVA films decreased the optical transmittance and energy band gap. Again, the increasing Bi_2O_3-doped to the composite films increased the reflectance, absorption coefficient and extinction coefficient values. The refractive index increased from 1.946 to 1.980 for Bi_2O_3 doped samples and the refractive index reached 2.468 with introducing CQDs to polymer composite film. The yellowness of polymer nanocomposite films was remarkably enhanced with CQDs addition. This novel material has potential use in fields in different fields, including optoelectronics and sensors.

1 Introduction

Blending two substances with dissimilar physical or chemical properties results in a composite material with qualities distinct from those of the original constituent parts. Polymers have been widely employed in a variety of applications. Multifunctional polymer-composites can be obtained by incorporation of the material in a polymeric matrix [1]. Polyvinyl alcohol (PVA) is an important polymer

Address correspondence to E-mail: heskalen@gmail.com; eskalen@ksu.edu.tr

https://doi.org/10.1007/s10854-023-10617-1

used in many different application areas, from the textile to the wood industry. Being able to be used in coatings, being soluble in water, being non-toxic, having high transparency, thermal stability and being flexible are some of the crucial features of PVA [2–4]. The biodegradability of PVA under certain microbial conditions has also paved the way for its use as an environmentally friendly polymer [5]. Another outstanding feature of PVA is that it is a self-healing material. After damage and breakage, it can repair itself without any external influence [6]. The presence of an organic interface layer between the metal and the semiconductor helps to improve the electrical and dielectric properties of the formed metal polymer semiconductors structures [7].

In literature, different materials, such as carbon-based nanomaterials, metal and metal oxide, were proven to increase optical and catalytic activity [1]. Bismuth is one of the least toxic and low-cost elements among heavy metals. It attracts the attention of researchers due to its wide band gap, superior radiation shielding and extraordinary optical properties [1, 8]. Moreover, its have unique photoluminescence, dielectric properties and ionic conductivity [9]. Because of above mentioned outstanding properties bismuth oxide can be used in medicine, catalysis, energy materials, superconductor materials, optical materials, and functional ceramics [10]. The main structures of the bismuth oxide are generally known as α-, β-, γ- and δ-Bi_2O_3 [11]. Radiation shielding properties of n-Bi_2O_3/epoxy-PVA matrix polymer was investigated and n- $Bi_2O_3 \geq 12$ wt % with 2 mm thickness can be used as shielding materials for lower X-ray photon energies was found [12]. The optical properties of bismuth-filled PVA composite were investigated and the obtained result reveals that the band gap energies are enhanced with the addition of bismuth [5]. The usability of Bi_2O_3/PVA (0.5%, 1.0% and 1.5%) in microwave device for reflecting purpose have been studied [13]. Dopamine-melamine nanoparticles incorporated in PVA films were fabricated and can be used as a unique UV absorber with transparent materials [14].

Carbon quantum dots (CQDs) have been considered significant nanoparticles because of their outstanding properties like nontoxicity, water solubility, extraordinary optical properties, and high chemical and physical stability. Moreover, it can be synthesized from a variety of organic materials and especially wastes and biomass, which reduces precursor cost and enable cost-effective CQDs synthesis [2, 15–17]. Various synthesis methods have been utilized to obtained this novel nanoparticle such as laser ablation, microwave irradiation, arc discharge and hydrothermal method. The microwave method is easy low cost and enables to adjust irradiation power and time so that it stands out one step further than other synthesis methods [18–20]. This unique nanoparticle has the potential to use in different application areas and some of the example areas are bioimaging, optical sensing, drug delivery, photocatalytic, light-emitting diodes, and anti-counterfeiting [21–23].

Most of the previous studies has been done to produce polymer-matrix composites using only one type of filler to matrix polymers. Therefore, unlike previous researches, the aim of this study is to produce polymer composites by using two different types of filler simultaneously which are Bi_2O_3 and carbon dots. In this study, to best of our knowledge CQDs obtained from green outer hull of the Prunus dulcis is chosen without the use of any hazardous chemicals or difficult technologies with utilizing simple green techniques. Bismuth oxide (Bi_2O_3), nanorods producted with sonochemical process. Bi_2O_3 nanorods and CQDs nanoparticles is used to form polymer nanocomposite. The Bi_2O_3/PVA, CQDs/PVA, and Bi_2O_3/CQDs/PVA codoped nanocomposites were prepared and their structural, morphological and detailed optical features of the obtained nanocomposite films were investigated for the first time.

2 Materials and method

2.1 Materials

The chemicals used to synthesize the sample were used in analytical purity without any purification. Bismuth (III) nitrate pentahydrate (BiN_3O_9 $5H_2O$) was purchased from Thermo scientific and NaOH Sigma Aldrich. Polyvinyl alcohol (PVA) was obtained from Acros Organics, Thiourea from Merck. All experiments were carried out using distilled water.

2.2 Preparation of CQDs nanoparticles

Prunus dulcis were obtained from the local market. The green outer hull of the Prunus dulcis was

washed with distilled water. The washed hull was dried in an oven at 75 °C for 48 h. Dried Prunus dulcis hull was ground with a blender. 2 g of ground Prunus dulcis hull and 2 g of thiourea were taken and mixed with 20 ml of distilled water. Ultrasonic treatment was applied for 20 min to form a homogeneous mixture. Carbonization was achieved by keeping the mixture in a microwave oven at 360 watts for 15 min. The obtained sample was thrown into 50 ml of distilled water and kept in an ultrasonic bath for 30 min. It was then filtered twice with filter paper.

2.3 Preparation of Bi_2O_3 nanoparticles

An easy and economical sonochemical method was used to fabricate α-Bi_2O_3 nanorods. For the synthesis of α-Bi_2O_3, 5.0 g of bismuth nitrate pentahydrate was added to 100 ml of distilled water and dissolved with continuous stirring. The solution was kept on a magnetic stirrer for about 30 min until a white sol was obtained. 5 M NaOH solution was added dropwise until the pH of the obtained sol was increased from 2 to 10. Then, a homogeneous mixture was obtained by applying ultrasonic treatment for 60 min. After this process, the colour of the white sol turned yellow. The mixture was stirred for 12 h to precipitate.

Since the reaction is pH-dependent, the following reactions take place [24]:

$$Bi(NO_3)_3 \cdot 5H_2O \rightarrow^{pH)9} Bi(OH)_3$$

$$Bi(OH_3) \rightarrow Bi_2O_3 + H_2O$$

The resulting precipitate was filtered. The yellow solution was washed several times with ethanol and distilled water. The resulting sample was dried in an oven at 80 °C for 24 h.

2.4 Preparation of PVA/CQDs/Bi_2O_3 composite films

All nanocomposite films were prepared using the solution casting method. Pure PVA film was prepared by dissolving 0.75 g of Polyvinyl alcohol in 50 mL of distilled water at 90 °C and pouring it into a 9 cm diameter petri dish. The prepared films were dried in a muffle furnace at 50 °C for 48 h. The synthesis detail of the composite films is given in Table 1. The produced composite films were named and it is shown in Table 1. Symbolic representation of the preparation of PVA nanocomposite films is illustrated at Fig. 1.

2.5 Characterization

The structural properties of the produced composite films were investigated using XRD (X-ray diffraction) device. In order to obtain the XRD patterns a Philips X'Pert PRO brand XRD device with Cu Ka radiation (λ = 0,154,056 nm, tuned at 40 kV and 30 mA) was utilized. UV–Visible Spectrophotometer (Shimadzu UV 1800) device was used to investigate the optical properties of the produced composite films. FTIR Spectroscopy using Perkin Elmer Spectrum 400 instrument. It was measured between 4000 cm^{-1} and 450 cm^{-1}. PL spectra of CQD samples were scanned using the Varian Cary Eclipse spectrometer. Hitachi HT7700 EXALENS, 120 kV, the electron microscope was used to obtain TEM (transmission electron microscopy) images of CQDs and Bi_2O_3 nanoparticles.

2.6 Calculations of optical parameters

Energy band gap values were estimated using the Tauc formula:

$$\alpha h\upsilon = B(h\upsilon - E_g)^2 \quad (1)$$

where h is Planck's constant, υ is the frequency of incident light, and B, a constant, measures the disorder of the material.

The α (Absorption coefficient) and k (Extinction coefficient) values of the produced composite films were estimated as follows [25]:

$$\alpha(\lambda) = \left(\frac{2.303}{d}\right)A \quad (2)$$

$$k = \frac{\lambda\alpha}{4\pi} \quad (3)$$

2.7 Determination of film colour

Placing the samples on a white plate allowed us to identify the colours of the films. We utilized the L* a* b* colour space because it reliably correlates colour values with visual perception (also known as the CIELAB colour space). A colour spectrophotometer (Veykolor Pro) with a 4 mm diameter area of illumination was used to measure the colours of the

Table 1 The details of the preparation of polymer nanocomposite films

Name	PVA (g)	Bi_2O_3 (g)	CQDs solution (mL)	Distilled water (mL)
PVA	0.75	0	0	50
PB1	0.75	0.005	0	50
PB2	0.75	0.01	0	50
PB3	0.75	0.02	0	50
PVACDs	0.75	0	0.5	50
PBC1	0.75	0.005	0.5	50
PBC2	0.75	0.01	0.5	50
PBC3	0.75	0.02	0.5	50

Fig. 1 Symbolic representation of the preparation of PVA nanocomposite films

films. The instrument was configured to measure in the CIE L*a*b* format and calibrated using the white and black standards included in the instrument's cap, where the values of spectrophotometric and photographic analysis are, respectively, 'L' (brightness), 'a' (red-green axis), and 'b' (yellow-blue axis). The parameters of a conventional absolute whiteness surface are L_0, a_0, and b_0. The following formulas were used to determine the yellowness index and whiteness index [26].

$$\text{Yellowness index} = 142.86(b^*/L^*) \quad (4)$$

$$\text{Whiteness index} = 100 - \sqrt{(100-L)^2 + a^{*2} + b^{*2}} \quad (5)$$

$$\Delta E = \sqrt{(L^* - L_0^*)^2 + (a^* + a_0^*)^2 + (b^* - b_0^*)^2} \quad (6)$$

2.8 Film opacity and transparency

The synthesized polymer nanocomposite films' transparency and opacity were determined from the following equations:

$$\text{Transparency} = \frac{\log(\%T_{600})}{x} \quad (7)$$

$$\text{Opacity} = \frac{Abs_{500}}{x} \quad (8)$$

here $\%T_{600}$ is the percentage of transmittance at 600 nm wavelength, Abs_{500} is the absorbance value at 500 nm and x is the thickness of the obtained films in millimeters [27].

3 Results and discussion

Figure 2 presents the XRD pattern of the prepared Bi_2O_3 material. The XRD result of the prepared Bi_2O_3 is similar to the current study in the literature [28–30]. The distinctive diffraction peaks of Bi_2O_3 correspond to the JCPDS file (01–071-0465). The prepared sample can be assigned to monoclinic P21/c phase α- Bi_2O_3 [28]. The result of the XRD model indicates the presence of the Bi_2O_3 structure, indicating the successful production of Bi_2O_3. Table 2 shows the angle of diffraction, the XRD parameters (h k l) and the d value that was derived from them.

The morphological feature and microstructure of the synthesized Bi_2O_3 were analyzed via TEM. Figure 3a shows the obtained Bi_2O_3 is rod-like morphology with a relatively smooth surface. The lengths of the particles were vaired between 9.72 to 2.48 μm diameter. Also, small rods like Bi_2O_3 nanoparticles on the image are clearly seen in Fig. 3b with diameter of 448 nm.

The prepared Bi_2O_3 nanoparticles were examined using UV–Vis spectroscopy (Fig. 4). It is seen from the absorption spectrum of Bi_2O_3 that it exhibits maximum absorption of around 291 nm. The tauc plot was obtained to determine the forbidden energy

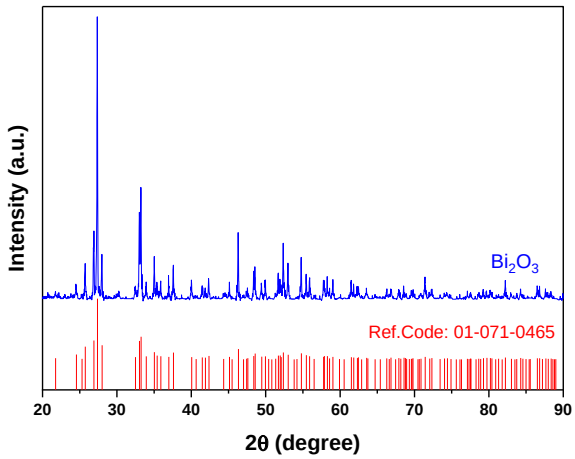

Fig. 2 XRD pattern of the Bi_2O_3

band gap (Eg) of Bi_2O_3. Extrapolation of the line segment intersecting the x-axis gave a value of 2.82 eV for the direct band gap [31].

X-ray (XRD) diffraction technique was used for the structural characterization of the prepared CQDs. The XRD model of the produced CQDs is given in Fig. 5. The diffraction pattern shows that a large 002 peak centered at 27° with low intensity is attributed to the characteristic carbonaceous material. This peak is attributed to the amorphous nature of the produced particles and the lack of order [32, 33].

TEM analysis shows that the Prunus dulcis-derived carbon dots are well dispersed in water, the shape of carbon quantum dots is semi-spherical and

Table 2 The d-value, angle diffraction, and XRD parameters (h k l)

S.No	h	k	l	2Theta [°]	d-spacing [Å]	S.No	h	K	l	2Theta [°]	d-spacing [Å]
1	0	2	0	21.751	4.08273	33	− 2	4	1	54.798	1.67389
2	− 1	0	2	24.555	3.62237	34	− 2	2	4	55.461	1.65545
3	0	0	2	25.748	3.45727	35	− 3	2	3	55.905	1.64333
4	− 1	1	2	26.904	3.31124	36	− 3	0	4	57.78	1.59439
5	− 1	2	1	27.392	3.25338	37	0	2	4	57.885	1.59176
6	− 2	1	1	32.490	2.75361	38	− 1	4	3	58.298	1.58147
7	− 1	2	2	33.034	2.70944	39	− 3	3	2	58.575	1.57463
8	− 2	0	2	33.242	2.69297	40	3	1	1	59.039	1.56336
9	0	2	2	33.951	2.63833	41	− 2	4	3	61.512	1.5063
10	− 2	1	2	35.04	2.5588	42	− 3	3	3	61.832	1.49927
11	0	3	1	35.419	2.5323	43	− 1	5	2	62.329	1.48851
12	1	0	2	35.900	2.49947	44	1	0	4	62.461	1.48567
13	− 1	3	1	36.972	2.42942	45	− 1	1	5	63.574	1.46233
14	− 1	1	3	37.609	2.38973	46	0	3	4	63.732	1.45908
15	− 2	2	2	40.059	2.249	47	− 4	1	3	66.281	1.40901
16	− 1	3	2	41.479	2.17525	48	− 2	2	5	66.835	1.39867
17	− 2	1	3	41.894	2.15466	49	− 1	4	4	67.904	1.37924
18	− 1	2	3	42.367	2.13167	50	− 1	5	3	68.593	1.36704
19	0	2	3	45.137	2.00711	51	− 4	2	3	69.581	1.35003
20	2	2	1	46.341	1.9577	52	− 3	4	3	69.666	1.34859
21	− 2	3	2	47.439	1.91491	53	− 4	0	4	69.798	1.34637
22	− 1	4	1	47.604	1.90867	54	− 1	6	1	71.442	1.31938
23	− 3	1	2	48.400	1.87911	55	2	3	3	72.333	1.30529
24	− 1	0	4	48.59	1.87224	56	− 1	6	2	74.423	1.27373
25	− 1	3	3	49.472	1.8409	57	0	3	5	77.34	1.23281
26	− 1	1	4	49.965	1.82389	58	− 2	2	6	80.205	1.19583
27	− 1	4	2	51.336	1.77836	59	3	1	3	80.409	1.1933
28	− 2	1	4	51.706	1.76647	60	− 4	4	3	82.228	1.17146
29	0	3	3	51.946	1.75888	61	− 3	4	5	84.289	1.14798
30	− 3	1	3	52.084	1.75455	62	4	3	1	86.518	1.12404
31	− 3	2	2	52.372	1.74558	63	− 5	2	2	86.821	1.12089
32	− 2	3	3	53.021	1.72572	64	− 3	6	2	87.670	1.11221

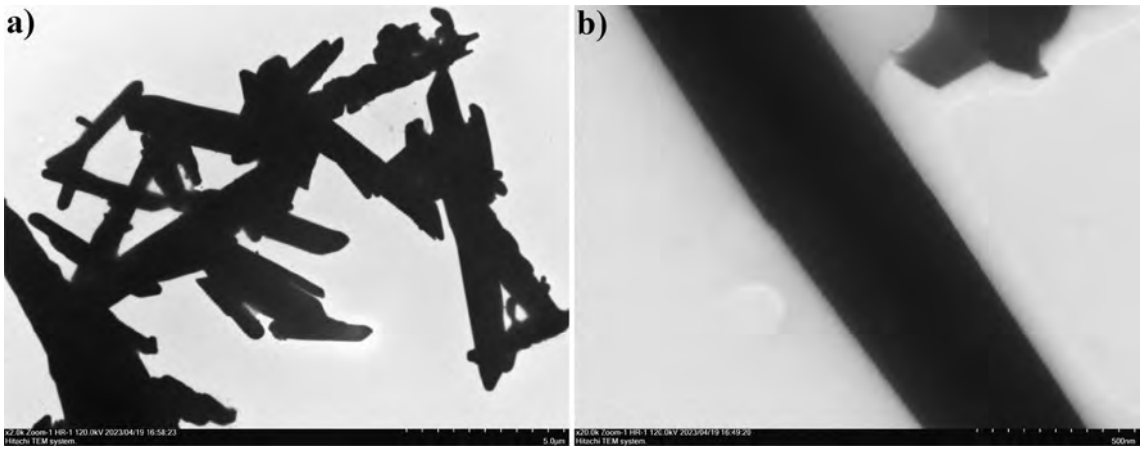

Fig. 3 TEM micrograph of the Bi_2O_3 rods **a** at low magnification and **b** at high magnification

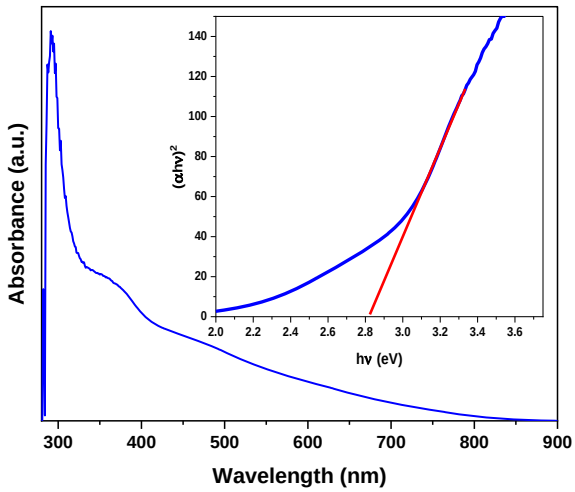

Fig. 4 Band gap pattern of Bi_2O_3

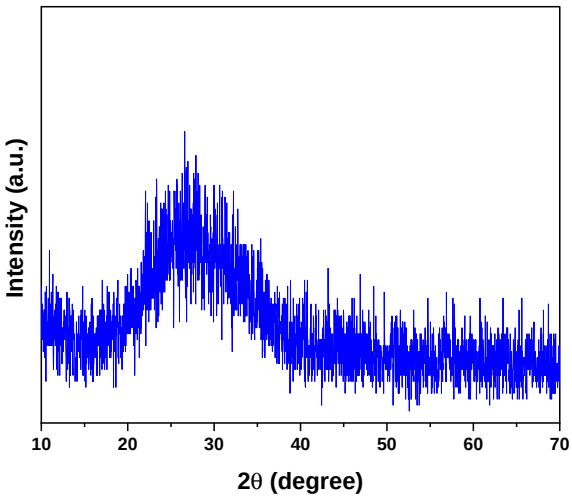

Fig. 5 XRD pattern of CQDs

uniform in size, as illustrated in Fig. 6. The average particle diameter is calculated as 31.07 nm with std 5.27 nm.

The optical properties of the produced CQDs sample were investigated by taking UV–Vis measurements. Pure water-soluble CQDs have a light brown color in daylight and fluorescent blue in the light of a UV lamp (365 nm). The absorption peak at 299 nm, seen in Fig. 7, is attributed to electron transition behaviours. The peak observed at 299 nm can be attributed to the n-π* transitions of the C=O/C=N bonds [34].

The PL emission spectra of the produced CQDs samples are presented in Fig. 8. While the excitation wavelength is 330 nm, the CQDs emission peak exhibits maximum intensity at 405 nm. When the excitation wavelength increases from 300 to 400 nm, the CQDs maximum emission peak shows redshift

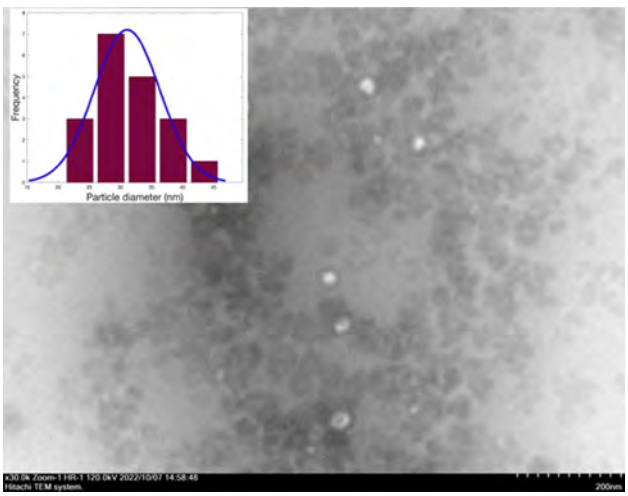

Fig. 6 TEM micrograph of the prepared CQDs, average particle diameter size in the inset

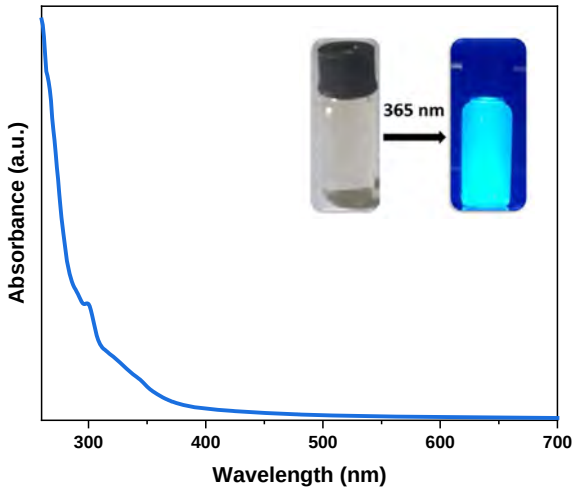

Fig. 7 The absorption spectrum of CQDs

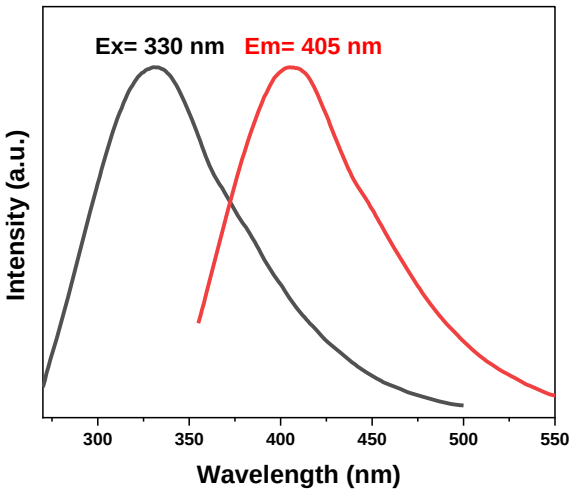

Fig. 8 Excitation and emission spectra of the CQDs

behaviour from 381 to 474 nm (Fig. 9). The quantum confinement effect of CQDs, the uniform and non-uniform particle size of CQDs, and the nature (carbon core and its supporting functional groups) of the surfaces of CQDs can all be employed to describe this redshift [35]. Additionally, it has been suggested that the excitation-dependent emission in the visible region may result from the distribution of various emissive sites/centers on each CQD's surface. This may be because the presence of various functional groups (C=O/C=N) on the surface of CQDs with various energy levels led to the formation of a number of emissive traps that control the emission at various excitation wavelengths [36]. Redshift in emission spectra raises the potential that the color of PL emission may be tunable [2].

The FTIR spectra of the samples are given in Fig. 10. CQDs were examined by FTIR spectroscopy to determine their chemical structures. A broad band centered at 3159 cm^{-1} and 3291 cm^{-1} is attributed to C–OH stretching and –OH bending vibrations [37, 38]. The band observed between 2100–1950 cm^{-1} can be attributed to the stretching vibrations of isothiocyanate (N=C=S) or thiocyanate (S−C≡N). The peaks at 1648.8 cm^{-1} and 1608.6 cm^{-1}, respectively, are attributed to the stretching vibrations of C=O and C= C [37, 39, 40]. The peaks at 1393 cm^{-1} and 1075.9 cm^{-1} can be assigned to the stretching vibrations of C–N and C–O [41, 42]. Also, the peak around 729 cm^{-1} can be attributed to the bending vibration of C–H [43, 44].

The structural properties of the prepared PVA nanocomposite films were investigated using XRD. XRD patterns of pure PVA, CQDs doped PVA, Bi_2O_3 doped PVA and CQDs/Bi_2O_3 doped PVA nanocomposite films are given in Fig. 11. The broad characteristic peak around 20° in the pure PVA XRD results indicates the amorphous structure. The XRD pattern of PVA with the CQDs added is not different from the XRD pattern of pure PVA. This is due to the amorphous nature of CQDs. With the addition of Bi_2O_3 to PVA, the sharp peaks of the bismuth oxide structure are clearly visible in the XRD graph. This result is compatible with the reference diffraction pattern of bismuth oxide with a monoclinic structure (Pdf code: 01–072-0398) [45]. In addition to the PVA peak, the planes of the three peaks (hkl) at 2θ = 27.47°, 33.34° and 55.69°, 57.16° belonging to the Bi_2O_3 structure are (120), (200) and (− 222).

UV–Visible absorption spectrums of PVA composite films measured in the range of 200 nm to 1100 nm are examined (Fig. 12). The peak peak at 275 nm can be attributed to the π–π* transitions of PVA caused by the C=O and C=C bonds, as seen in Fig. 12a; the absorbances of nanocomposite films are higher compared to pure PVA. As the proportion of Bi_2O_3 increases, the absorbance increases. This results from the presence of Bi_2O_3 nanoparticles dispersed in the polymer that absorbs the incoming radiation [46, 47]. As similar to Bi_2O_3/PVA samples, the absorbance value of Bi_2O_3/CQDs/PVA samples increases with parallel to the Bi_2O_3 concentration of samples (Fig. 12 b). The hydroxyl and isothiocyanate or thiocyanate functional groups are present on the synthesized CQDs surface. This can increase the n-π*

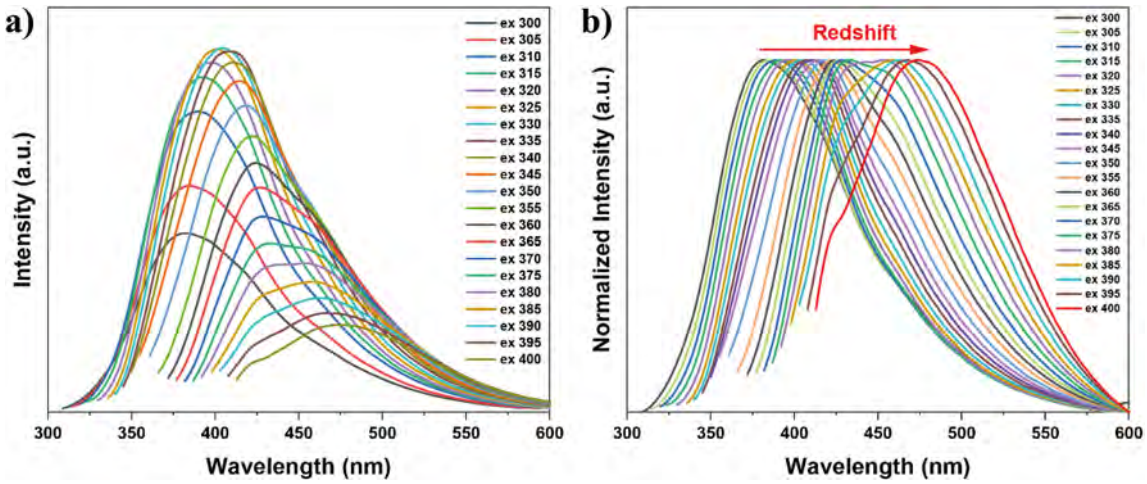

Fig. 9 **a** Emission spectra of CQDs solution under different excitation wavelengths, **b** Normalized PL spectra of the CQDs excited by different wavelength

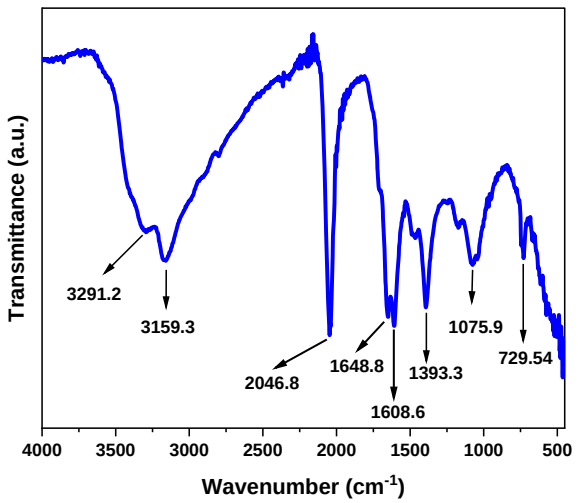

Fig. 10 FTIR spectra of CQDs

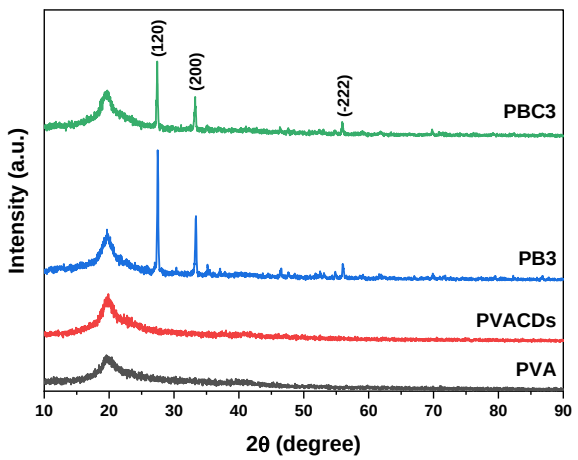

Fig. 11 XRD pattern of polymer nanocomposite films

transitions and increase the measured absorbance values [48].

The transmittance spectra of pure PVA and nanocomposite films are given in Fig. 13. As seen in all patterns, nanocomposite films with Bi_2O_3 and CQDs added show lower transparency in the visible region than pure PVA film. The decrease in permeability can be attributed to the aggregation and the increase in the number of charge carriers, which occurs due to increasing concentrations of Bi_2O_3 nanoparticles in the composite films[46, 47].

In Fig. 14, reflectance spectra of pure PVA and nanocomposite films are presented. When these spectra are examined, it will be seen that the reflection rate increases as the amount of Bi_2O_3 additive increases. This is an expected result of agglomerations that may occur due to increased Bi_2O_3 concentration [49].

The absorption coefficient is a distinguishing feature of absorbent materials. The absorption coefficient expresses the ability of a substance to absorb light of a certain wavelength per unit length. The absorption coefficients of CQDs and Bi_2O_3 doped PVA composite films are shown in Fig. 15. It is seen from the graph that the absorption coefficient is relatively low at high wavelengths, that is, at low energies. This indicates low absorption and means that the probability of electron transition is low. As the wavelength decreases, that is, as the energy increases, a significant increase in the absorption coefficient is observed. At higher energies, the absorption is significantly increased, indicating the

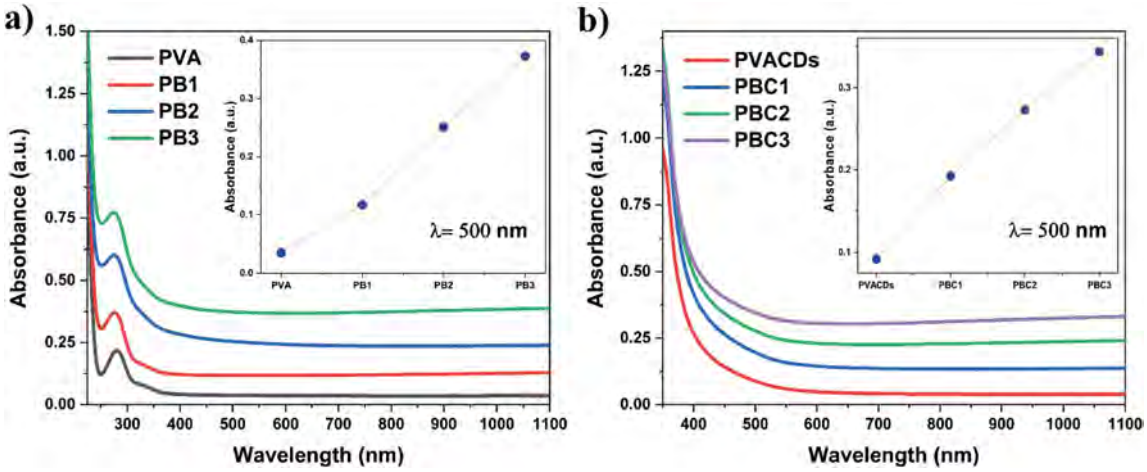

Fig. 12 Absorbance pattern of **a** Bi_2O_3/PVA and **b** Bi_2O_3/CQDs/PVA nanocomposites

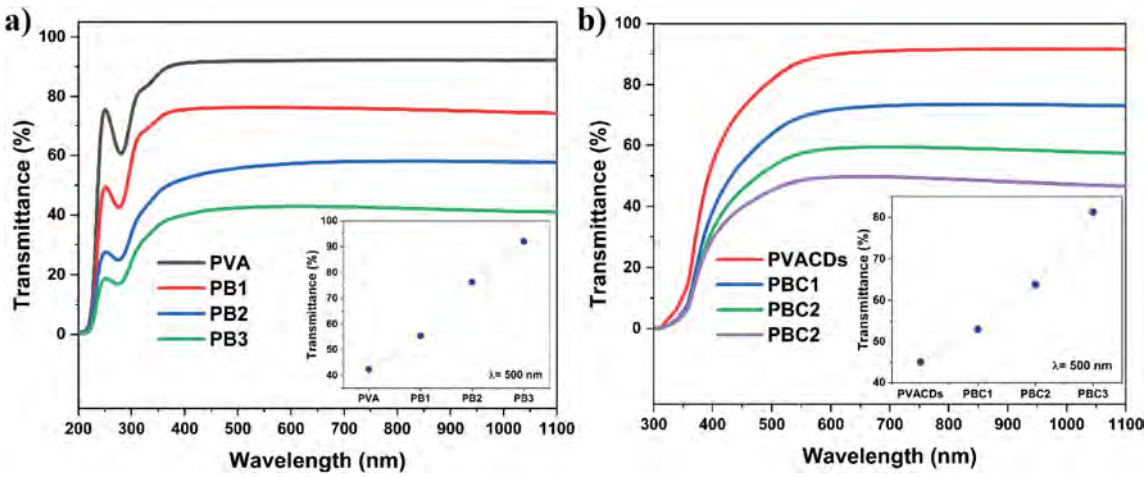

Fig. 13 Transmittance pattern of **a** Bi_2O_3/PVA and **b** Bi_2O_3/CQDs/PVA nanocomposites

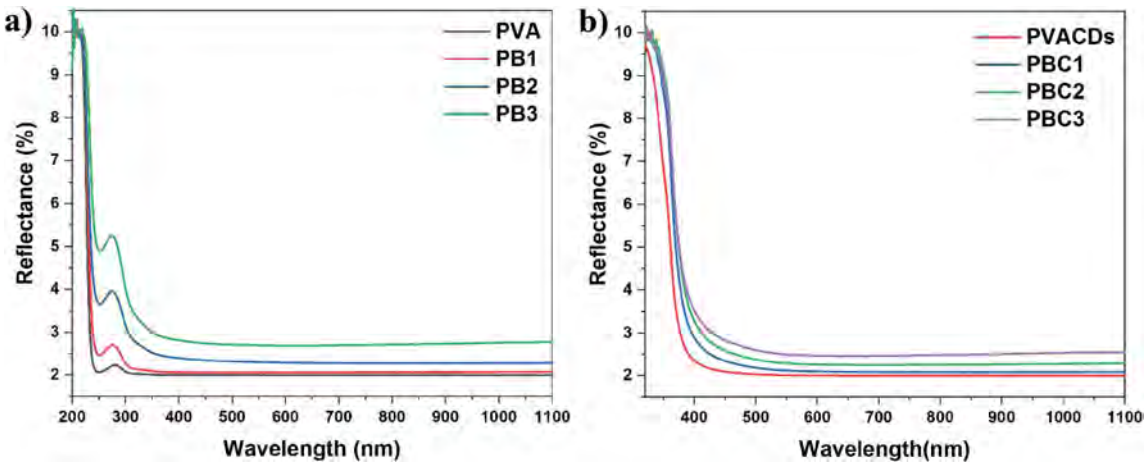

Fig. 14 Reflectance pattern of **a** Bi_2O_3/PVA and **b** Bi_2O_3/CQDs/PVA nanocomposites

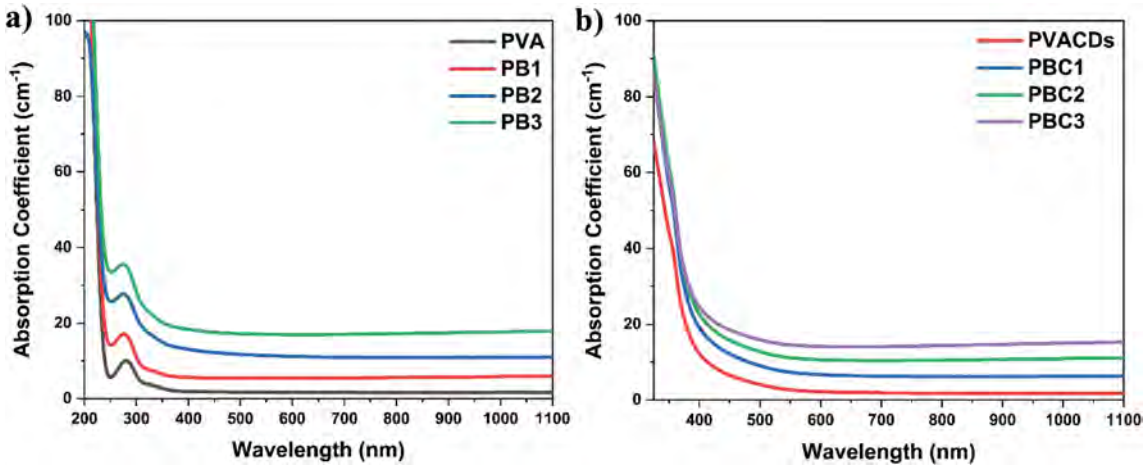

Fig. 15 Absorption Coefficient pattern of **a** Bi_2O_3/PVA and **b** Bi_2O_3/CQDs/PVA nanocomposites

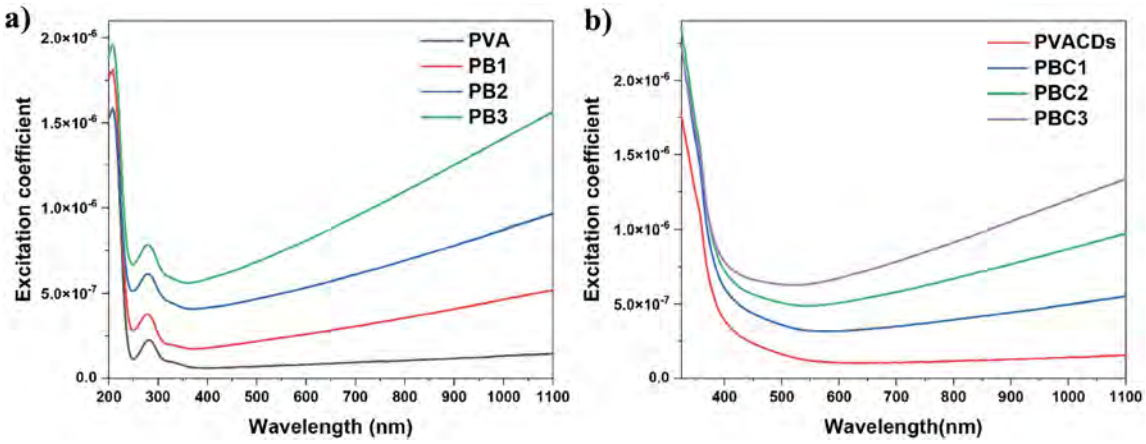

Fig. 16 Excitation coefficient pattern of **a** Bi_2O_3/PVA and **b** Bi_2O_3/CQDs/PVA nanocomposites

high potential of electron conduction. The absorption coefficient in nanocomposite films increases with increasing Bi_2O_3 contribution. The increase in the absorption coefficient creates the expectation of direct electron transfer at higher energies [47, 50].

The extinction coefficient (k) expresses the differences in the loss of electromagnetic energy caused by photon scattering and absorption per unit thickness. It is a distinctive feature. Figure 16 shows the change in extinction coefficient values of all composite films as a wavelength function. It is clearly seen from Fig. 16 that the damping coefficient increases with the increase of Bi_2O_3 additive concentration. This can be attributed to the high absorption coefficient. In addition, k increased with increasing wavelength [25, 47, 49].

The energy band gaps of the composite PVA films were determined using the UV–Vis spectroscopy technique. The graphs in Fig. 17 show the energy band gaps of all films against photon energy. The optical band gap was determined by the Tauc method. The energy band gaps of the composite films were found between 5.37 eV and 2.75 eV. It was found as 5.37 eV, 5.3 eV, 5.22 eV, 5.13 eV, 3.16 eV, 3 eV, 2.85 eV and 2.75 eV for PVA, PB1, PB2, PB3, PVACDs, PBC1, PBC2 and PBC3, respectively. As can be seen from the graph, the optical band gap decreased as the amount of Bi_2O_3 additive increased in PVA composite films. Optical band gap energy of CQDs doped Bi_2O_3-PVA composite films are shown in Fig. 17.

The concentrations of bismuth oxide and carbon dot nanoparticles in the prepared polymer composite films affect the values of their optical bandgaps. When compared to pure PVA, the optical energy bandgap of polymer composite films decreased with

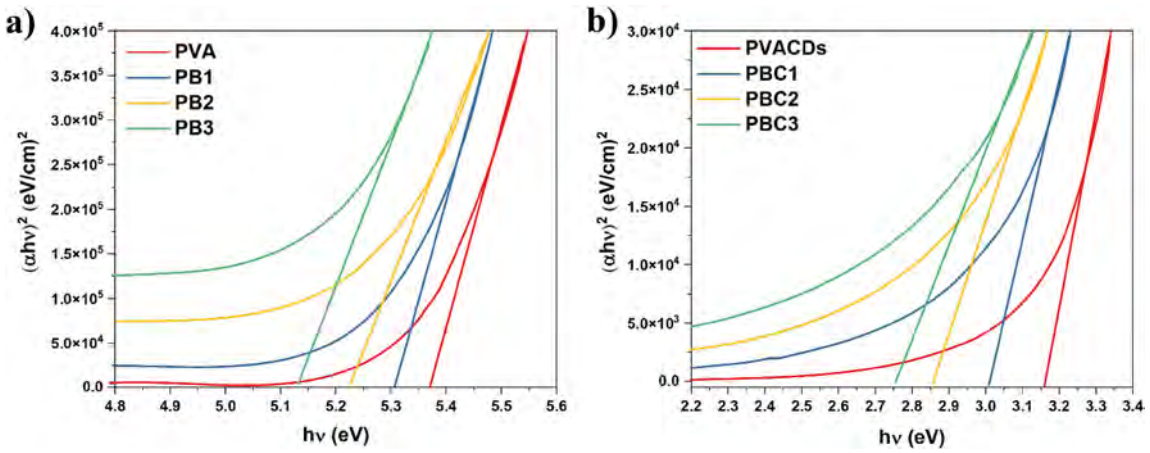

Fig. 17 Band gap energy of prepared **a** Bi_2O_3/PVA and **b** Bi_2O_3/CQDs/PVA nanocomposites

an increase in nanofiller weight. The band gap gets decreasing as doping levels increase, according to numerous studies reported [51–54]. This pattern was noticed because nano-filler particles may organize themselves in the polymer matrix, creating conductive paths where electron hopping can take place. A change in the valence and conduction bands as well as an improvement in carrier-carrier interaction result from this situation. The bandgap is lowered as a result of the high carrier concentration in the valence and conduction bands [55]. In some studies, this behaviour is explained by the fact that the used nanofiller can cause defects in the PVA polymer matrix [56] and producing more defects and charge carriers within the PVA polymer band [57]. The charge transport complexes that exist in the energy bands between HOMO and LUMO may have caused to the decrease in Eg values. From to XRD data, the result is consistent with the increased PVA disordering degree for the obtained composite structure [58]. This result's sophisticated combination between fillers and PVA chains illustrates the host matrix's researched engineering optical band gap. Adjusting the band gap makes the PVA/Bi2O3/CQDs polymer composite suitable for optoelectronic applications. The schematic illustration of bandgap energy of the polymer composite film is shown in Fig. 18.

Refractive index is generally written as $n^* = n + ik$, here, the refractive index is a complex function with a real portion (linear refractive index) and an imaginary part (extinction coefficient). Using the ratio $(n^2-1)/(n^2+2) = 1-(E_g/20)^{1/2}$ $(n^2$ -1)/$(n^2 + 2)$ = 1-$(E_g/20)^{1/2}$, the n values for the polymer nanocomposites around the wavelength of an

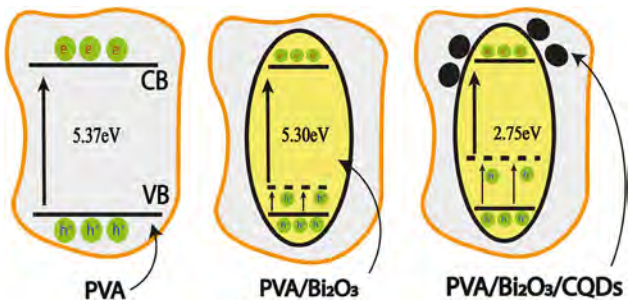

Fig. 18 The schematic illustration of bandgap energy of polymer composite film

absorption edge can be determined from their E_g values [59]. An important consideration when employing materials to utilise optical instruments, optoelectronic devices, filters, optical switches, modulation, light-emitting diodes, and waveguides is the index of refraction (n) [60]. The n values for the obtained Bi_2O_3/PVA and Bi_2O_3/CQDs/PVA films were established using the relation $E_g = E_{gd}$, (E_{gd}, direct band gap of sample) and the obtained results are shown at Fig. 19. As filler dopant concentrations increased, the polymeric film's refractive index increased as well, which was perfectly consistent with the findings of the current study. The obtained results of the refractive index showed the considerable influence of the Bi_2O_3 and CQDs dopants on the PVA composite films, which suggested the proposed films to be possibly a promising, adaptable candidate in optoelectronic devices [61]. The increase in packing density of the produced nanocomposite film, which is reported in the literature [46, 62, 63], might be the cause of the refractive index increase with concentration. This situation results from an increase in

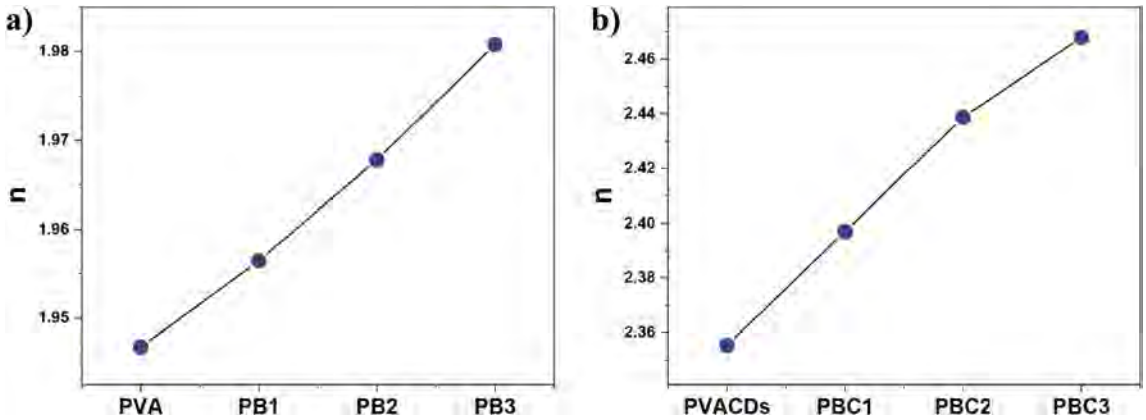

Fig. 19 Refractive index of **a** Bi_2O_3/PVA and **b** Bi_2O_3/CQDs/PVA nanocomposites

Table 3 Color parameters, whiteness index and yellowness index of the nanocomposite films

	L	a	b	ΔE	Yellowness	Whiteness
PVA	87.750	− 1.080	0.890	3.661	1.449	87.670
PB1	85.130	− 1.400	2.970	6.614	4.984	84.772
PB2	83.540	− 1.940	5.060	8.931	8.653	82.671
PB3	85.760	− 3.920	9.450	10.605	15.742	82.466
PVACDs	81.730	− 1.930	28.080	28.853	49.082	66.444
PBC1	69.120	− 1.450	24.140	32.196	49.894	60.777
PBC2	76.490	− 1.760	28.820	31.653	53.827	62.765
PBC3	74.440	0.380	35.540	38.595	68.206	56.222

reflection brought on by an improvement in the refractive index brought on by a rise in the incoming photon's dispersion [64]. Also it may have linked this increase to the creation of intermolecular interactions between the filler and the OH group in PVA [63].

For optical applications, a change in colour shade or intensity is a crucial practical characteristic. To assess and quantify the color variation of the synthesized polymer nanocomposite films, a colourimetry investigation was conducted. Table 3 provides an overview of the mean deviation of the CIELab coordinates L*, a*, and b* and the DE (total color difference) values for acquired films [65]. With the inclusion of more Bi_2O_3 particles, the yellowness of the films produced increased, and this rise gained significant momentum with the addition of CQDs to the composite structure. This decline can be brought on by the scattering of light caused by the inclusion of filler in the polymer matrix [27]. The inclusion of CQDs resulted in a drop in the determined whiteness ratio. Despite having a high yellowness index, CQDs doped nanocomposite films may be used as food packaging materials since they are equivalent to normal films [66].

Optical opacity is an important parameter used to assess the transparency of a film. A higher opacity value indicates a more transparent film. Figure 20 demonstrates, the transparency and opacity results of the obtained films. CQDs nanoparticles had a more significant influence on the film's transparency and yellowness. It has also been demonstrated that the nanocomposite films prepared here could also be used as beneficial UV barriers [67]. It has been noted that the edible polyvinyl alcohol films' transparency decreased when chitosan was added [68].

4 Conclusion

The engineering of new or unique polymer composite materials has become essential for usage in several optoelectronic and nanodevice applications, including photovoltaics, solar cells, light filters, and UV detectors. In this study, morphology, structure and optical properties of PVA nanocomposites reinforced with bismuth oxide nanoparticles and carbon

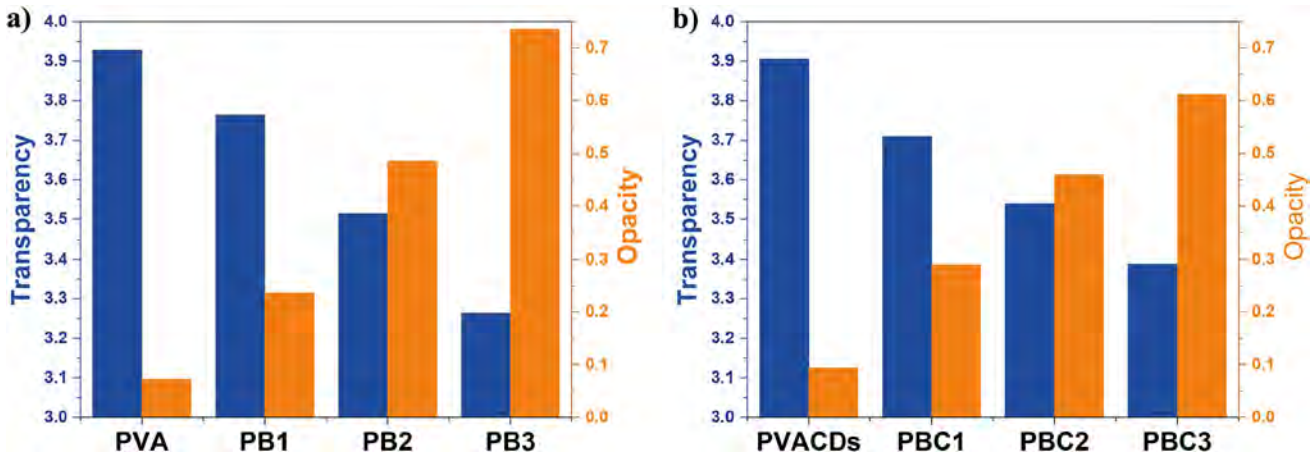

Fig. 20 Transparency and opacity at 600 nm of **a** Bi_2O_3/PVA, **b** Bi_2O_3/CQDs/PVA nanocomposites

quantum dots (CQDS) were investigated. Green outer hull of the Prunus dulcis is chosen without the use of any hazardous chemicals or difficult technologies, green methods and techniques have been employed in a simple and affordable manner to produce CQDs from the natural source for the first time. It has been determined that the synthesized CQDs have an amorphous structure from X-ray pattern. As a result of the TEM analysis, the average particle size was calculated to be 31 nm. The obtained CQDs gave a maximum PL peak at 405 nm when excitaed at 330 nm. More over, excitation dependent emission (tunable emission colour) is observed from this novel nanodots. Bi_2O_3 nanorods were produced using bismuth nitrate precursor using a sonochemical method. In the XRD examination, it was observed that Bi_2O_3 has a monoclinic structure. The morphological properties of the synthesized Bi_2O_3 were examined by TEM analysis, and it was observed that the particles had a diameter of 448 nm. For Bi_2O_3 nanostructures, the direct band gap value was 2.82 eV. Polymer composite films were synthesis with solution casting methods with using PVA. The degree of crystallinity of Bi_2O_3 is reduced with introducing PVA polymer is found. As the amount of Bi_2O_3 additive to the composite films increased, the optical transmittance decreased from 90 to 40%. Similarly, as the bismuth additive ratio increased, the energy gap value decreased from 5.37 eV to 2.75 eV. R, α and k values increased as the bismuth content in the composite films increased. The refractive index of prepared nanocomposite films was enhanced by introducing Bi_2O_3 and further increased with CQDs doped samples. This novel polymer composite material has potential use in optoelectronics and sensors for future applications.

Acknowledgements

This study was supported by the Scientific Research Projects Coordination Unit of Kahramanmaraş Sütçü İmam University. Project number 2021/1-7 YLS.

Author contributions

The manuscript was written with the contributions of all authors. All authors have approved the final version of the manuscript. MK: Experimental measurements, investigation, HE: Experimental measurements, investigation, review & editing, supervision.

Funding

Kahramanmaraş Sütçü Imam Üniversitesi, 2021/1-7 YLS., Hasan Eskalen

Data availability

Not Applicable.

Code availability

Not Applicable.

Declarations

Conflict of interest The authors declared that they have no conflicts of interest to this work. We declare that we do not have any commercial or associative interest that represents a conflict of interest in connection with the work submitted.

Ethical approval Not Applicable.

References

1. H.M. Gayitri, M.Q.A. Al-Gunaid, F. H. AL-Ostoot, N. Al-Zaqri, A. Boshaala, and A. P. Gnanaprakash, Investigation on opto-electrical, structural and electro-chemical performance of PVA/ZnBi2MoO7 hybrid nanocomposites. Polym. Bull. **80**, 773 (2023)
2. H. Eskalen, H. Yaykaşlı, M. Kavgacı, A. Kayış, J. Mater. Sci.: Mater. Electron. **33**, 4643 (2022)
3. Y. Kavun, H. Eskalen, S. Kerli, M. Kavgaci, Appl. Radiat. Isot. **177**, 109918 (2021)
4. H. Eskalen, M. Çeşme, S. Kerli, Ş Özğan, J. Chem. Res. **45**, 428 (2021)
5. M.V. Muthamma, S.G. Bubbly, S.B. Gudennavar, K.C.S. Narendranath, J. Appl. Polym. Sci. **136**(37), 47949 (2019)
6. P. Tiamduangtawan, C. Kamkaew, S. Kuntonwatchara, E. Wimolmala, K. Saenboonruang, Radiat. Phys. Chem. **177**, 109164 (2020)
7. M. Yildirim, M. Gökçen, T. Tunç, I. Uslu, Ş Altindal, Polym. Eng. Sci. **54**, 1811 (2014)
8. M. Irfan, M. Aslam, Z.A. Raza, Polym. Bull. **80**, 791 (2023)
9. Y. Badali, Y. Azizian-Kalandaragh, İ Uslu, Ş. Altindal **31**, 8033 (2020)
10. F. Sedaghatdoust-Bodagh, Y. Azizian-Kalandaragh, J. Opto-electron. Adv. Mater. **19**, 663 (2017)
11. W.E. Mahmoud, A.A. Al-Ghamdi, F. Al-Agel, Polym. Adv. Technol. **22**, 2055 (2011)
12. B.M. Abunahel, S. Iskandar, N.Z. Mustafa, N. Azman, Appl. Phys. **124**, 828 (2018)
13. A Singh, R Prasad, KP, SP and undefined 2018, in Ieeexplore.Ieee.Org (2018 International conference on applied electromagnetics, signal processing and communication (AESPC), nd)
14. Y. Wang, J. Su, T. Li, P. Ma, H. Bai, Y. Xie, M. Chen, W. Dong, ACS Appl. Mater. Interfaces **9**, 36281 (2017)
15. M. Çeşme, H. Eskalen, Bilecik Seyh Edebali University J. Sci. **8**, 924 (2021)
16. M. Aslan, H. Eskalen, Fullerenes. Nanotubes Carbon Nanostructures **29**, 1026 (2021)
17. S.K. Başkaya, B. Tahta, S. Uruş, H. Eskalen, M. Çeşme, Ş Özğan, Biomass. Convers. Biorefin. **1**, 1 (2022)
18. M. Çeşme, H. Eskalen, Cumhuriyet Sci. J. **41**, 808 (2020)
19. H. Eskalen, Appl. Phys.. A Mater. Sci. Process **126**, 1 (2020)
20. H.U. Castañeda-Serna, G. Calderón-Domínguez, A. García-Bórquez, M. de la P. Salgado-Cruz, and R. R. Farrera Rebollo, Structural and luminescent properties of CQDs produced by microwave and conventional hydrothermal methods using pelagic Sargassum as carbon source. Opt. Mater. (Amst) **126**, 112156 (2022)
21. H. Eskalen, M. Kavgaci, A. Kayiş, Ş Özğan, Eskişehir Techl University J. ScI. Technol. Appl. Sci. Eng. **22**, 366 (2021)
22. H. Eskalen, S. Uruş, S. Cömertpay, A.H. Kurt, Ş Özgan, Ind. Crops. Prod. **147**, 112209 (2020)
23 M. Çeşme, H. Eskalen, S.K. Başkaya, Fruits and Vegetable Wastes: Valorization to Bioproducts and Platform Chemicals, in *Fluorescent Carbon Dots from Vegetable and Fruit Wastes and Their Applications*. ed. by R.C. Ray (Springer Nature Singapore, Singapore, 2022)
24. S. Sharma, S.K. Mehta, A.O. Ibhadon, S.K. Kansal, J. Colloid. Interface. Sci. **533**, 227 (2019)
25. Z.K. Heiba, A.M. El-naggar, M.B. Mohamed, Y. Altowairqi, A.M. Kamal, Appl. Phys. A Mater. Sci. Process **127**, 1 (2021)
26. M. Koosha, S. Hamedi, Prog. Org. Coat. **127**, 338 (2019)
27. P. Terzioğlu, F. Güney, F.N. Parın, İ Şen, S. Tuna, Food Packag Shelf Life **30**, 100742 (2021)
28. A.Z. Szeremeta, S. Pawlus, A. Nowok, K. Grzybowska, M. Zubko, A. Molak, J. Am. Ceram. Soc. **103**, 3732 (2020)
29. V.N. Sonkusare, R.G. Chaudhary, G.S. Bhusari, A.R. Rai, H.D. Juneja, Nano-Str. Nano-Objects **13**, 121 (2018)
30. T.A. Gadhi, A. Hernández-Gordillo, M. Bizarro, P. Jagdale, A. Tagliaferro, S.E. Rodil, Ceram Int. **42**, 13065 (2016)
31 J. Krishna Reddy, B. Srinivas, V. Durga Kumari, M. Subrahmanyam, Chem. Cat. Chem. **1**(4), 492 (2009)
32. K. Jlassi, A. Khalaf Ahmed, H. Mutahir, A. M. Abdullah, M. M. Chehimi, and I. Krupa, (n.d.).
33. H. Eskalen, M. Kavgacı, A. Kayış, Ş Özğan, Eskişehir Techl. Univ. J Sci. Technol. Appl.. SciEng. **22**, 366 (2021)
34. Y. Ni, P. Zhou, Q. Jiang, Q. Zhang, X. Huang, Y. Jing, Dyes Pigm. **197**, 109923 (2022)
35. H. Eskalen, S. Uruş, M. Kavgacı, H.V. Kalmış, B. Tahta, Biomass Convers. Biorefin. **1**, 1 (2023)
36 I. Mondal, D. Samanta, M. Shaw, M. Abdus Salam Shaik, M. Kr Mahto, R. Basu, A. Bhattacharya, and A. Pathak, Spectrochim. Acta A Mol. Biomol. Spectrosc. **294**, 122530 (2023)

37. J. Shen, S. Shang, X. Chen, D. Wang, Y. Cai, Mater. Sci. Eng., C **76**, 856 (2017)
38 K. Qu, J. Wang, J. Ren, X. Qu, Chem. A Eur. J. **19**, 7243 (2013)
39. J. Jia, W. Lu, S. Cui, C. Dong, S. Shuang, Microchim. Acta **188**, 1 (2021)
40. G. Liu, Z. Chen, X. Jiang, D.Q. Feng, J. Zhao, D. Fan, W. Wang, Sens Actuators. B Chem. **228**, 302 (2016)
41. K. Huang, Q. He, R. Sun, L. Fang, H. Song, L. Li, Z. Li, Y. Tian, H. Cui, J. Zhang, Chem. Phys. Lett. **731**, 136586 (2019)
42. F. Akhgari, N. Samadi, K. Farhadi, J. Fluoresc. **27**, 921 (2017)
43. A.F. Shaikh, M.S. Tamboli, R.H. Patil, A. Bhan, J.D. Ambekar, B.B. Kale, J. Nanosci. Nanotechnol. **19**, 2339 (2018)
44. A. Kurdekar, L.A.A. Chunduri, E.P. Bulagonda, M.K. Haleyurgirisetty, V. Kamisetti, I.K. Hewlett, Microfluid Nanofluidics **20**, 1 (2016)
45. M. Mohammadi, A. Tavajjohi, A. Ziashahabi, N. Pournoori, S. Muhammadnejad, H. Delavari, R. Poursalehi, Micro. Nano Lett. **14**, 239 (2019)
46. Z.K. Heiba, M.B. Mohamed, J. Mol. Struct. **1181**, 507 (2019)
47. S.S. Najm, Mater. Today Proc. **61**, 632 (2022)
48 S.B. Aziz, A.Q. Hassan, S.J. Mohammed, W.O. Karim, M.F.Z. Kadir, H.A. Tajuddin, N.N.M.Y. Chan, Nanomaterials **9**(2), 216 (2019)
49. N.J. Mohammed, Z.S. Rasheed, A.S. Hassan, Al-Mustansiriyah J. Sici. **29**, 118 (2018)
50. G. Abdul Hadi Abdul Jabbar, A. Abdulmunem Saeed, and M. F. Hadi AL-Kadhemy 2022 Int. J. Nanoelectron. Mater.
51. M.I. Mohammed, I.S. Yahia, S.A. El-Mongy, J. Appl. Polym. Sci. **140**, e53821 (2023)
52. M.F. Zaki, A. Tayel, A.B. El Basaty, Bull. Mater. Sci. **45**, 1 (2022)
53. F.M. Ali, F. Maiz, Physica B Condens. Matter. **530**, 19 (2018)
54 A.M. Al-Fa'ouri, O.A. Lafi, H.H. Abu-Safe, M. Abu-Kharma, Arabian. J. Chem. **16**, 104535 (2023)
55 Z. Faiza, A. Malik, A.A. Khattak, Alahmadi, and S. U. Butt, Materials **15**(15), 5154 (2022)
56 S.H. Zyoud, A. Almoadi, T.H. AlAbdulaal, M.S. Alqahtani, F.A. Harraz, M.S. Al-Assiri, I.S. Yahia, H.Y. Zahran, M.I. Mohammed, Sh. Mohamed, Abdel-wahab, Polymers **15**(15), 1351 (2023)
57. S.A.M. Issa, D.E. Abulyazied, A.W. Alrowaily, H.A. Saudi, E.S. Ali, A.M.A. Henaish, H.M.H. Zakaly, J. Rare Earths (2023). https://doi.org/10.1016/j.jre.2023.02.013
58 A. Atta, A.M. Abdel Reheem, E. Abdeltwab, Ion beam irradiation effects on surface morphology and optical properties of ZnO/PVA composites. Surf Rev Letters (2020). https://doi.org/10.1142/S0218625X19502147
59. P. Dhatarwal, R.J. Sengwa, Physica B Condens. Matter. **613**, 412989 (2021)
60. H.E. Ali, M. Abdel-Aziz, A.M. Ibrahiem, M.A. Sayed, H.S.M. Abd-Rabboh, N.S. Awwad, H. Algarni, M. Shkir, M.Y. Khairy, Microstructure Study and Linear/Nonlinear Optical Performance of Bi-Embedded PVP/PVA Films for Optoelectronic and Optical Cut-Off Applications. Polymers **14**(9), 1741 (2022)
61. T.H. AlAbdulaal, A. Almoadi, I.S. Yahia, H.Y. Zahra, M.S. Alqahtani, E.S. Yousef, K.I. Hussein, M. Jalalah, F.A. Harraz, M.S. Al-Assiri, Optik (Stuttg) **268**, 169741 (2022)
62. T.S. Soliman, S.A. Vshivkov, J. Non. Cryst. Solids **519**, 119452 (2019)
63. M.S. Ismail, A.A. Elamin, F. Abdel-Wahab, Y.H. Elbashar, M.M. Mahasen, Opt. Mater. (Amst) **131**, 112639 (2022)
64. G. A. Hadi Abdul Jabbar, A. A. Saeed, and M. F. Hadi AL-Kadhemy, Kuwait (2023) J. Sci.
65. S. Alashrah, Y. El-Ghoul, F.M. Almutairi, M.A.A. Omer, Development, characterization and valuable use of novel dosimeter film based on PVA polymer doped nitro blue tetrazolium dye and AgNO3 for the accurate detection of low X-ray doses. Polymers **13**, 3140 (2021)
66. I. Dudeja, R. K. Mankoo, A. Singh, and J. Kaur, (n.d.).
67. Y. Amaregouda, K. Kamanna, T. Gasti, V. Kumbar, J. Polym. Environ. **30**, 2559 (2022)
68. S.R. Kanatt, M.S. Rao, S.P. Chawla, A. Sharma, Food Hydrocoll **29**, 290 (2012)